Design and Control of Magnetic Resonance-Compatible, Pneumatic Actuators and

Robotic Platforms for Steerable Needle Interventions

BY

DAVID BENJAMIN COMBER

Dissertation

Submitted to the Faculty of the

Graduate School of Vanderbilt University

in partial fulfillment of the requirements

for the degree of

DOCTOR OF PHILOSOPHY

in

Mechanical Engineering

December 2015

Nashville, Tennessee

Approved:

Eric J. Barth, Ph.D.

Robert J. Webster III, Ph.D.

Michael Goldfarb, Ph.D.

Joseph S. Neimat, M.D.

William Grissom, Ph.D.

Soli Deo honor et gloria

Acknowledgment

There are many people who have helped and encouraged me in my educational journey to the Ph.D. degree. I would like to thank my advisors, Eric Barth and Bob Webster, for their guidance and support throughout my graduate studies. I am very grateful for their mentorship and encouragement, particularly during my academic job search and the NIH grant preparation process. It has truly been a pleasure to work for and learn from them.

I am also grateful for the generous advice and help from additional faculty members. I wish to thank several professors in particular for their support: Michael Goldfarb, Tom Withrow, Pietro Valdastri, and Nabil Simaan. I would also like to thank professors Jeff Mayer and Jack Mitchell at Penn State for encouraging me to go to graduate school.

Due in part to the interdisciplinary nature of my research, I have received help from many professors and students. I wish to thank Joseph Neimat for his generous input and collaboration on the clinical aspects of my project. For their help with MRI scanner experiments, I would like to thank Will Grissom and Chuck Nockowski at the Institute of Imaging Science (VUIIS). For hosting and teaching me first-hand know-how on MRI-guided robotic systems, I would like to thank Greg Fischer and his students from the A.I.M. Lab at Worchester Polytechnic Institute.

The fluid power community has been incredibly supportive of my work. I thank the Center for Compact and Efficient Fluid Power (CCEFP) for funding my project. I would like to thank Kim Stelson as a particular champion for my research and for his encouragement in my academic job search. I am especially grateful for several years of working collaboration with Jonathon Slightam and Vito Gervasi at Milwaukee School of Engineering. I also wish to thank Andrew Plummer and Nigel Johnston for hosting me at the University of Bath during the summer of 2013.

During the rigorous and formative experiences of graduate school, my fellow graduate students have provided heartening camaraderie and inspiration. I am particularly grateful to have shared five years at Vanderbilt with Phil Swaney, David Earl, and Joe Chen. I am deeply indebted to past and present members of the DCES Lab: Andy Willhite, Chao Yong, Mark Hofacker, Alex Pedchenko, John Tucker, Bryn Pitt, Anna Winkelmann, Josh Cummins, Yue Chen, and Tyler Gibson. They were influential in my decision to come to Vanderbilt and later to continue beyond the master's degree. I would also like to thank several past and present members of the MED Lab for their generous help with my research: Hunter Gilbert, Phil Swaney, Diana Cardona, Rich Hendrick, Raul Wirz, Ray Lathrop, and Jessica Burgner-Kahrs.

My family and several friends outside the Vanderbilt community have been a major source of personal encouragement and helped me persevere during my graduate studies. I am forever grateful for my parents, sisters, and grandparents, for their love and prayers. I thank my parents for exemplifying the values of hard work and education and introducing me to a love for science. I

Table of Contents

List of Figures

List of Tables

Abstract

This dissertation presents the design and validation of a robotic platform to control steerable needles under magnetic resonance imaging (MRI) guidance. The use of MRI to guide needle-based interventions provides clinicians with informative data, including excellent visualization of soft tissue, needle placement confirmation, and thermal dose monitoring. Additionally, the patient stands to benefit from the minimally-invasive and radiation-free nature of MRI-guided interventions. However, because the closed, narrow bore of high-field MRI scanners substantially limits clinician access to the patient during imaging, many interventions require the use of a compact robot to help deliver the needle to the target under MRI guidance. Such a robot must satisfy the challenging requirements of safety, precision, compactness, and magnetic resonance (MR)-compatibility. Numerous potential interventions have yet to be realized because the majority of MR-compatible robots reported to date were designed in an anatomy-specific way and are thus difficult to apply to other anatomical targets. Therefore, the goal of the work described herein is to develop a modular robotic platform to actuate concentric tube steerable needles, a class of continuum robot applicable to treatment of a broad range of anatomical structures. The design, fabrication, and control of two, multiple degree-of-freedom prototypes are described. To the author's knowledge, the first prototype is the first fully-pneumatic MR-compatible robot to be reported for neurosurgical applications. The main contributions of the second prototype are hybrid pneumatic control for precise and intrinsically-safe operation, and novel designs of bellows actuators additively manufactured for compactness and hermetic sealing. To enable a novel, foramen ovale approach to epilepsy treatment using the modular MR-compatible robot, prototypes of a non-invasive head holder, a helical needle, and a radiofrequency ablation electrode are presented. Finally, the potential applicability of this non-invasive approach to a wide range of patients is explored. Designed using nonlinear optimization, curvilinear concentric tube needle trajectories are shown to accurately traverse the medial axis of the hippocampus for twenty different cases. The results herein collectively contribute robotic hardware and controls to help transform deep brain therapy from open surgery to a minimally-invasive procedure.

Chapter 1 – Overview

Introduction

Image-guided interventions (IGI) combine needle-based hardware with pre- or intra-operative use of medical images to perform therapy without traditional surgical access. The general aims of IGI are to reduce patient trauma and cost of care while also improving patient outcomes. Visual feedback by direct line-of-sight in open surgery is replaced in IGI by a navigation system for device tracking, image registration, and visualization. Conventional instruments in open surgery are replaced in IGI by miniature end effectors controlled by robotic manipulators. An important subclass of manipulators is steerable catheters or needles.

While the history of IGI dates back to early use of x-ray to extract foreign objects from appendages, the advent of modern IGI began in the 1980s as navigation systems for stereotactic neurosurgery arose from the invention of the personal computer [1]. Computer technology allowed for three-dimensional (3-D) imaging modalities like computed tomography (CT) or magnetic resonance imaging (MRI) to be used for planning stereotactic interventions. The high spatial resolution and 3-D volume basis of these modalities enable stereotaxy by providing adequate visualization of the untreated eloquent tissue in close proximity to the target tissue.

The state-of-the-art in commercial navigation systems for stereotactic neurosurgery is found in products like StealthStation (Medtronic PLC, Dublin), NAV3i (Stryker, Inc., Kalamazoo, MI) and iPlan (Brainlab AG, Munich). These systems overlay pre-operative images with the interventional device, which is typically registered and tracked optically or electromagnetically. A major limitation of the state-of-the-art is inability to use closed-bore, diagnostic MRI scanners intra-operatively. This limitation arises not from the navigation technology, but rather from the magnet's long and narrow geometry, necessary to create a strong, homogeneous magnetic field. As shown in Fig. 1.1, the resulting tightly confined space within the scanner typically prevents adequate clinician access to the patient.

The major motivations for intra-operative MRI (iMRI) with IGI are to correct on-the-fly for brain shift and to improve monitoring and confirmation of the therapy. Brain shift is change in morphology after pre-operative imaging, particularly occurring during the surgery as intra-cranial pressure equilibrates to atmospheric. Deformations can be as much as 20 mm [2], resulting in substantial inaccuracy in the spatial relation between the real-time morphology and the pre-op image. For therapy monitoring and confirmation, there are several reasons why MRI is preferable to CT.
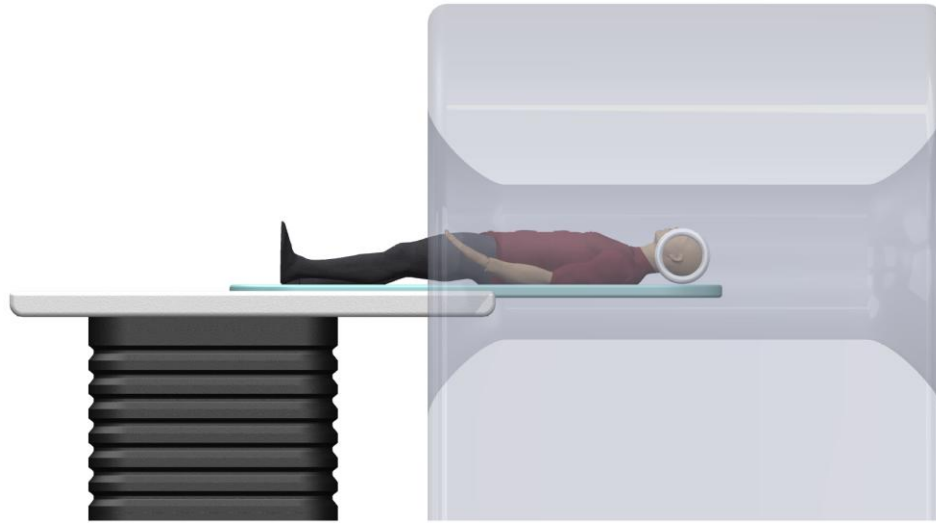
Figure 1.1 – Computer-aided design (CAD) model of an MRI scanner with human-scale manikin.

Radiation exposure to the patient and clinical team using CT would be high [1], as frequent image acquisitions are required to safely place the needle and to monitor the therapy. If the therapy is thermal ablation, a common example of IGI, it is difficult to monitor with CT. However, techniques like MR thermal imaging (MRTI) can directly measure change in tissue temperature. Additionally, MRI provides better soft tissue distinction than CT, and this is generally beneficial for visualizing the eloquent tissues of the brain. Perfusion and neural activity can also be acquired with other MR-based imaging techniques.

Commercially available iMRI scanners improve clinician access to the patient during imaging. Early iMRI scanners typically had an open, "double donut" bore, while newer designs favor a higher strength, closed-bore magnet plus a patient transfer system for intermittent imaging throughout the procedure. One notable design, VISIUS Surgical Theatre (IMRIS, Winnipeg, MB), features a stationary operating table and movable scanner suspended on a ceiling-mounted gantry. This system originated from the NeuroArm project at the University of Calgary, where two 7 degree-of-freedom (DOF) robotic arms were developed for brain tumor microsurgery with iMRI [19-20].

However, the general trend with iMRI has been to move away from specialized scanners towards standard magnets [3]. Surgeries with the specialized systems are expensive and also slow, because imaging with the scanner and operating on the patient cannot take place at the same time. This problem can potentially be solved using compact robots that can interact with the patient inside the scanner. The main technological barriers to doing this are that the robot must fit compactly in the scanner with the patient—there is little space available (see Fig 1.1)—and it must be fully non-magnetic and MRI-compatible. Hospitals could readily use these robots with existing diagnostic scanners, which are substantially more common than iMRI systems.

A robotic system of this kind could additionally provide the clinician increased accuracy and more degrees of freedom within the minimally invasive context. For percutaneous interventions in

the brain, where it is critical to closely monitor needle position and therapy delivery, MRI guidance and MRTI are particularly advantageous. In light of this pronounced potential impact within neurosurgery, this dissertation research has focused on development of a robotic, needle-based treatment for cases of medically-intractable epilepsy.

Background and Significance

Magnetic Resonance Compatible Robots

Precise needle tip placement is required for many IGI procedures, such as biopsy, thermal ablation, brachytherapy and deep brain stimulation. In these procedures, accurate positioning of the needle tip is limited by several factors, including tissue deformation, registration error and dependence on hand-eye coordination. Target accuracy has generally improved in recent years due to the development and use of image-guided surgical robots. Furthermore, real-time imaging during surgery can streamline procedures by reducing or eliminating the need for pre-operative imaging. For neurosurgical applications the need for intraoperative imaging is particularly great, as brain shift error typically occurs when only pre-operative imaging is available, and there is more criticality to monitor needle position and therapy delivered.

Because magnetic resonance imaging (MRI) generally provides the most informative type of medical images, there is substantial interest in developing fully MR-compatible surgical robots. Indeed, many of these devices have been invented in the past two decades, and the extreme conditions of the MRI operating environment have been surmounted by remarkable innovations. Because MRI scanners produce strong magnetic fields, fast-changing magnetic field gradients, and powerful radiofrequency pulses, conventional mechatronic systems are not suitable for MRI-guidance applications. Any electromagnetic actuator found in such systems cannot be used because its ferrous core renders it not MR-safe. MR-compatible systems require alternative forms of actuation that both are non-magnetic (MR-safe) and do not malfunction due to the magnetic fields nor generate image artifacts (MR-compatible). Photographs of several noteworthy MR-compatible robots found in the literature are presented in Fig. 1.2.

Four general types of actuation are used in MR-compatible robots: manual, hydraulic, piezoelectric and pneumatic. Manual actuation has been implemented successfully in devices for prostate brachytherapy. Namely, Krieger et al. achieved better than 2mm accuracy with a 3-DOF manually actuated robot under 1.5T imaging; the authors later modified this system to employ piezoelectric motors [4, 5]. While manual actuation is fully MR-compatible, it is also the slowest type of system to operate and has not reduced procedure times to the same extent as other forms of MR-compatible actuators.
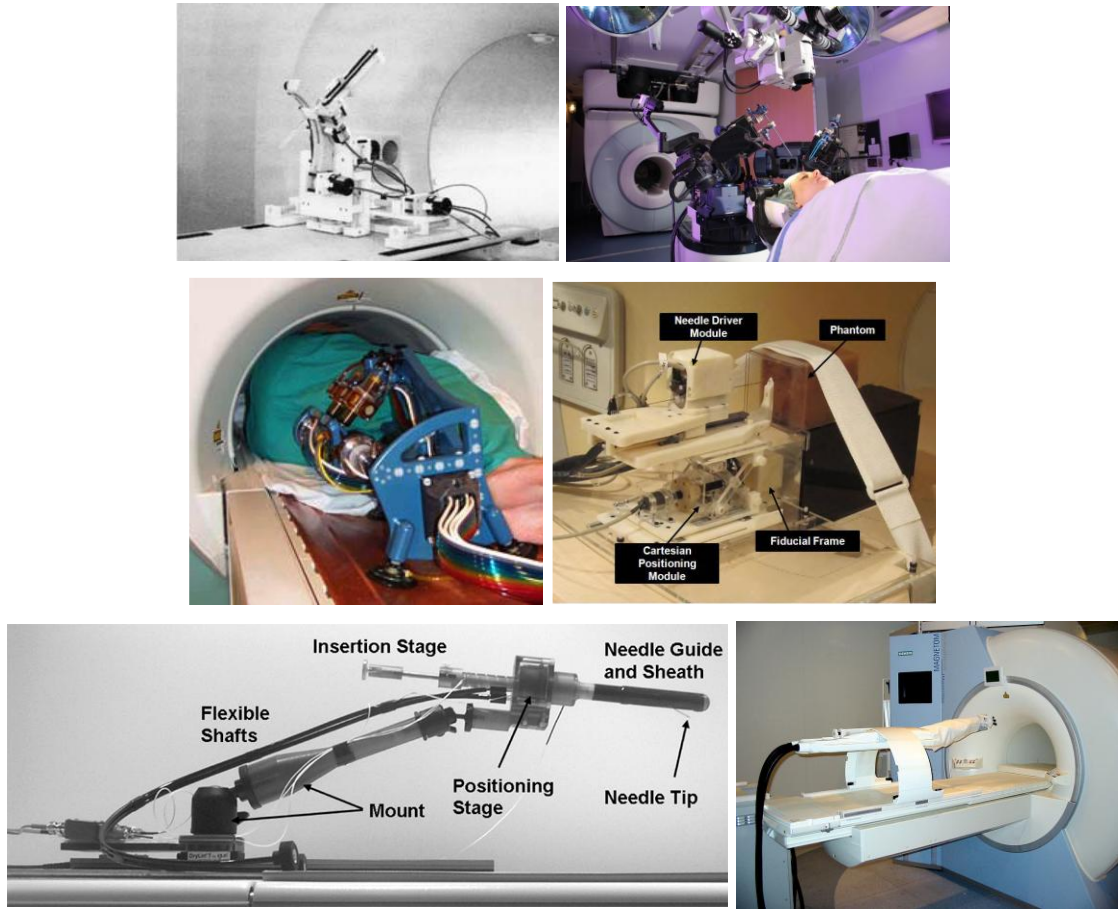
Figure 1.2 – A selection of MR-compatible robots. Clockwise from top left: Masamune et al. [10], Sutherland et al. [16], Su et al. [39], Melzer et al. [22], Krieger et al. [5], Muntener et al. [19]

Kim et al. and Moser et al. have shown hydraulic actuators to be a viable technology in MR-compatible systems [6, 7]. However, Kim et al. encountered problems with air bubbles in the fluid system and with fluid leakage. Similarly, Elhawary et al. note that for hydraulic systems, there is the risk of contamination of the sterile environment in the event of a fluid spill, as well as a safety risk at the typical operating pressure of 15 bar [8].

Reviewing the spectrum of MR-compatible robots, Tsekos et al. conclude that the majority have used piezoelectric motors [9]. Reported in 1995 by Masamune et al., the first MR-compatible robotic platform used piezomotors to position a needle for stereotactic neurosurgery, but the motors substantially degraded the image quality [10]. While piezomotors provide many desirable characteristics, such as high torque, low backlash and a hard brake, commercially available piezomotors must be located far from the magnet isocenter in order to realize acceptable signal-to-noise ratio (SNR). This restriction is inherent to the high frequency power supply for piezomotors. Designs for MR-compatible robots have attempted to avoid this problem by locating the piezomotors farther from the imaging volume or by electromagnetically isolating the motor drives from the scanner room. However, many designs still produced unacceptable levels of signal noise

that precluded manipulator actuation during MR imaging, as described in [9]. For example, Krieger et al. reported 40% to 60% reduction in SNR when piezomotors were enabled [5]. Thus, even at a substantial distance away from magnet isocenter, the motors must power down during imaging.

Elhawary et al. review several MR-compatible systems employing piezomotors, all remotely actuated through mechanisms like drive shafts, belt or chain drives, and linkages [8]. These transmissions can result in undesirably large robots. For example, while Larson et al. achieved sub-millimeter accuracy at 4T with a 5-DOF robot for stereotactic breast interventions, the authors note that larger patients cannot fit inside the scanner because the telescoping robot substantially reduces the clearance [11]. Wang et al. successfully demonstrated a 6-DOF robot that can operate inside a standard high field 3T diagnostic magnet with the piezomotors running and also located next to the head coil. However, preservation of a high SNR required substantial modifications to the piezomotors drivers [12]. Similarly, Su et al. reported a very small, 2% loss in SNR during simultaneous imaging and servoing of piezomotors; non-harmonic motors were selected for reduced noise and the commercial motor driver boards were replaced with custom, low-noise drivers [13].

Clinical use of piezomotor-driven robotic systems has also been demonstrated. Pfleiderer et al. reported clinical testing of a piezomotor robotic system with a manual biopsy gun for breast lesion diagnosis [14]. Pandya et al. reported several tumor resections using NeuroArm, two MRI-guided, piezomotor-actuated arms each of seven degrees of freedom [15, 16].

To a lesser extent than piezomotors, pneumatic actuators have also been used in the development of MR-compatible surgical robots. Pneumatic actuators offer several advantages over piezoelectric and hydraulic systems. As these actuators are completely free of electrical circuitry when implemented with optical sensors, they do not introduce artifacts to the MR images. Easily powered by medical instrument air already available in hospitals, they do not pose a contamination hazard, in contrast to hydraulic systems. The gas dynamics also make pneumatic actuators favorable for fast or force-controlled applications [17].

In light of these desirable characteristics, several MR-compatible devices are reported to employ either double-acting pneumatic piston cylinders or pneumatic stepper motors. Stoianovici et al. invented PneuStep, a precision pneumatic stepper motor that has successfully operated within a 7T scanner [18]. Using a 6-DOF MRI-guided robot with PneuStep technology, Muntener et al. reported an accuracy of 2.02 mm for prostatic needle placement in-vivo in canines [19]. Two other pneumatic, rotational stepper motors are reported by Chen et al. and Sajima et al. [20, 21].

The creators of INNOMOTION, an MR-compatible robotic system commercially available in Europe for spine surgery, used piezoelectric motors in an early version of the robot. However, reduction in image quality and the risk of inductive heating led the team to an improved design with pneumatic piston-cylinders, engineered for safety and controllability through high dynamic and low static friction characteristics [22]. In other research efforts, pneumatic piston-cylinders have been

used in several MRI-guided needle placement robots designed to diagnose and treat cancers of the prostate and breast [21, 23]. A robot employing a fail-safe ratcheting mechanism with piston-cylinders demonstrated successful image-guided interventions in pig abdomens [24]. Similarly, Fischer et al. reported a needle tip accuracy of 0.94 mm RMS for a transperineal prostate robot actuated by piston-cylinders with custom fail-safe rod locks [25]. MRI-guided needle placement for prostate biopsy and brachytherapy has been clinically performed with robots actuated either by a one-axis pneumatic needle drive or fully manually [26, 27].

A frequently cited choice of pneumatic piston cylinder is the MR-compatible Airpel model line manufactured by Airpot Corp (Norwalk, CT). With these actuators Song et al. achieved an average position accuracy of 0.3 mm in a 3T scanner by incorporating external damping into their 4-DOF robot for prostate brachytherapy [28]. Another system for prostatic interventions was developed by Fischer et al. and demonstrated a very low, 5% reduction on SNR [25]. Thus, the literature suggests that pneumatic actuation is an excellent technology to enable MR-compatibility in robotic systems.

Precision Pneumatic Controls

The dynamics for pneumatic piston-cylinder actuators are highly nonlinear but precision control with them has been demonstrated in both surgical and non-surgical applications [24, 27-36]. Selecting glass cylinders with graphite pistons for a low-friction, air-bearing effect, Ben-Dov and Salcudean implemented small-scale force tracking using two flapper-nozzle valves with pressure feedback [29]. Richer and Hurmuzlu reported a thorough mathematical model of the pneumatic servo system for spool-type valves, and they proceeded to demonstrate accurate force tracking using sliding mode control (SMC) [30-31]. An excellent primer on sliding mode control theory can be found in [32]. It is well established that for pneumatic applications, nonlinear control schemes can achieve superior accuracy. Ning and Bone demonstrated that a nonlinear model-based controller outperformed a linearized model-based approach [33]. Similarly, Chillari et al. compared the performance of several pneumatic position control methods, and concluded a nonlinear approach is preferable to proportional-integral-derivative (PID) control [34].

In the context of this dissertation research, position control is of greater interest than force or pressure control. Yang et al. reported 1 mm needle tip accuracy for a 1-DOF MR-compatible device using a fiber-optic 3D force sensor [35]. Zhu and Barth achieved 0.05 mm accuracy in robot joint space using a composite adaptive-SMC force tracker for an industrial robot [36]. While accuracy on the order of micrometers has been shown for industrial actuators, it has yet to be achieved with MR-compatible piston-cylinders until this dissertation research.

Concentric Tube Steerable Needles

While pneumatic technology is well suited for MRI-guided robotic applications, requirements

for inherent safety and precision control dictate a custom solution. Robot hardware for this work was designed to actuate concentric tube steerable needles. A class of continuum robots, the concentric tube steerable needle (also known as the active cannula) is made up of multiple, nested tubes, each of superelastic nitinol. Typically, the tip of each tube is precurved by a heat treatment process [37, 38] to a circular curve or helical curve. Controllable needle motion is realized as the tube bases (proximal ends) are axially translated or rotated relative to one another (see Fig. 1.3). To impart these motions to the needle tubes, various actuation units have been reported in the literature, including one piezoelectric MR-compatible version [39-41]. Beam-mechanics-based models for motion control of concentric tube needles are described in [42-47].
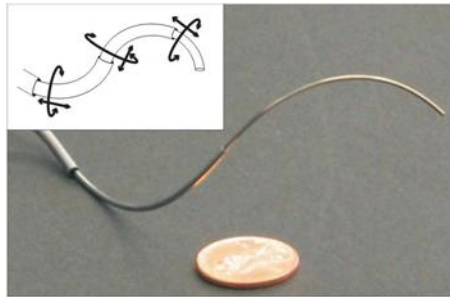
Figure 1.3 – A steerable needle made from telescoping, curved, superelastic tubes.

Image-Guided Interventions for Epilepsy Therapy

Research towards an MRI-guided robotic treatment for epilepsy is motivated by the high prevalence of and severe disability caused by this neurological disease. The debilitating effects of epilepsy are a stark reality for some 50 million epilepsy patients world-wide [48]. With a patient population of 2.3 million adults and 500,000 children in the United States, epilepsy accounts for an estimated $15.5 billion annually in medical costs and lost or reduced income or production [49]. Prevalence is estimated at 0.5 to 1.0%, and epilepsy is said to account for 1% of the global burden of disease [50-51].

In 20 to 40 percent of epilepsy cases, anticonvulsant medications fail to provide seizure control [48, 51-52], putting the patient at substantial risk for sudden unexplained death in epilepsy (SUDEP). Furthermore, studies demonstrate that if initial anticonvulsant monotherapy is ineffective, trials of subsequent medications yield diminishing benefit [48]. Additionally, patients failing to obtain seizure control are estimated to have a 30-fold increase in lifetime disease cost [53]. Even for patients achieving good seizure control by medicinal therapy, common medications have debilitating side effects such as fatigue, blurred vision, and cognitive effects that represent a significant additional patient burden and may limit compliance with or efficacy of these therapies. Furthermore, significant adverse effects are possible including inflammation or failure of the liver or pancreas, and serious reductions in white blood cell or platelet counts.

Surgical resection of the hippocampus, where seizures commonly begin, is a potentially

permanent cure for patients with medically-refractory epilepsy. Studies have shown a seizure-free rate following hippocampectomy of 70 to 80 percent [52, 54-55]. In fact, the results of randomized trials of epilepsy surgery suggest that "in temporal-lobe epilepsy, surgery is superior to prolonged medical therapy" [50]. Additionally, the American Academy of Neurology has concluded that temporal lobectomy is effective in reducing seizures, improving quality of life, and reducing risk of long term mortality [56].

Despite these compelling findings, several studies in nations with standardized and more universally regulated healthcare have demonstrated an underutilization of epilepsy surgery in excess of 50%, and it is estimated to be even higher at 90% in the USA and UK [52, 55-57]. These high rates of undertreatment likely arise from inherent physician bias against brain surgery [58]. While there are significant risks of open-brain surgery, the risks of intractable epilepsy are greater and more frequent. The SUDEP rate is 7 to 17% for the epilepsy population as a whole but as high as 50% in patients with refractory epilepsy [59, 60].

Recent technological advances including laser tissue ablation and MR thermography have reinvigorated an interest in the development of minimally-invasive therapies for the treatment of temporal lobe epilepsy [61]. MR thermography allows for real time visualization of thermal deposition during an ablation procedure. Three different experimental MRI-guided systems have been reported in the literature for epileptogenic foci ablation: Visualase [61-64], ClearPoint by MRI Interventions [65], and NeuroBlate by Monteris Medical [66, 67].

Preliminary results using the Visualase laser applicator demonstrated a 6-month seizure freedom rate of 54% in a small series of patients and suggest relative safety and more limited morbidity compared to open resection [61]. These results approach rates achieved by surgical resection and are a substantial improvement upon stereotactic ablations which were not image guided and which achieved much smaller volumes of ablation [68, 69].

However, these MRI-guided ablation systems are limited by the need to drill an opening in the skull, and pass through a significant volume of untreated brain tissue before reaching the mesial structures. Thus, these approaches carry attendant risks of hemorrhage and damage to eloquent brain structures. In addition, these systems use either a "frameless" mini-frame or a traditional stereotactic frame. Manually rather than robotically adjustable, these devices can require multiple patient transfers into and out of the MRI scanner, similar to iMRI systems. Thus, introducing a compact, MRI-compatible robot could streamline surgical workflow. Furthermore, these stereotactic techniques are limited to linear trajectories, which may limit the total volume of hippocampus ablated, and may represent the principal cause of decreased efficacy relative to current surgical techniques (i.e. 54% vs. 70-80%). This gap in efficacy motivates the development of an MRI-guided robotic steerable needle capable of non-linear trajectory motion as well as reduced invasiveness by novel, foramen ovale access.

In contrast to the traditional "straight shot" needle as aimed using a stereotactic frame, the

concentric tube robot introduces the potential for non-linear trajectories that would, for example, improve the coverage of lesioning a tumor or seizure focus tissue. To achieve the coordinated motion required for these non-linear trajectories, robotic control is needed.

For this dissertation research, a high impact application for this technology was identified, namely, temporal-lobe epilepsy. The general concept for using the concentric tube robot to treat epilepsy is illustrated in Fig. 1.4. This percutaneous treatment would deploy the steerable needle through a straight outer cannula, which is manually inserted beneath the cheek skin and docked to the foramen ovale, a small natural opening in the skull base. Actuated at its proximal end by the precision pneumatic robot prototype, the needle would deploy out of the foramen ovale and maneuver a radiofrequency ablation electrode along the length of the hippocampus from head to tail. Magnetic resonance imaging would guide the needle along the planned path, and MR thermometry would monitor the delivery of thermal ablative therapy.
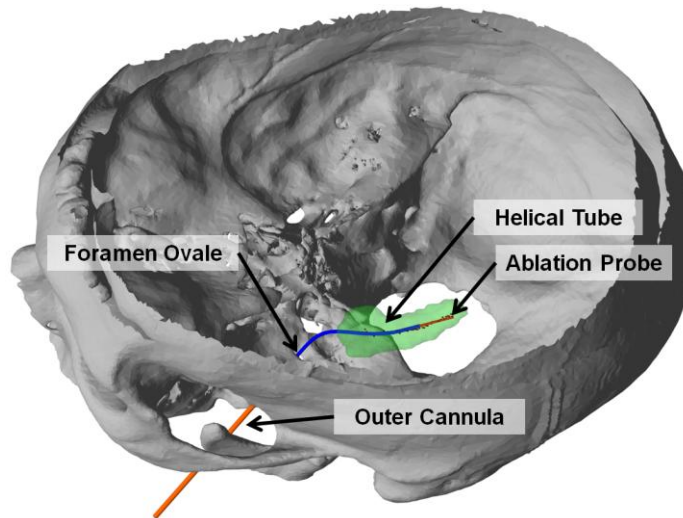
Figure 1.4 – Concentric tube needle and ablation probe design for transforamenal therapy.

<u>Document Organization</u>

This dissertation comprises six chapters. Chapter 2 describes an MR-compatible concentric tube robot that was designed for a back-of-the-skull approach to the hippocampus. Chapter 3 presents robot hardware and controls resulting from a second design iteration to improve device safety, compactness, and sterilizability. Chapter 4 reports hardware design and validation to enable the foramen ovale approach to hippocampotomy. Chapter 5 investigates the feasibility of transforamenal hippocampotomy for multiple patients by optimization of the concentric tube robot design parameters. Chapter 6 summarizes the dissertation, its key contributions, and a roadmap for future work. Summaries of the manuscripts included in this dissertation are as follows:

Manuscript 1 (Chapter 2): *Design and Control of a Magnetic Resonance Compatible Precision Pneumatic Robot*, D. B. Comber, E. J. Barth, and R. J. Webster III

From: *ASME Journal of Medical Devices*, 8(2):011003, 2014.

Abstract: The versatile uses and excellent soft tissue distinction afforded by magnetic resonance imaging (MRI) have led to the development of many MR-compatible devices for MRI-guided interventions. This paper presents a fully pneumatic MR-compatible robotic platform designed for neurosurgical interventions. Actuated by non-magnetic pneumatic piston-cylinders, the robotic platform manipulates a five degree-of-freedom active cannula designed for deep brain interventions. Long lines of tubing connect the cylinders to remotely located pressure sensors and valves, and MRI-compatible optical sensors mounted on the robot provide the robot joint positions. A robust, nonlinear, model-based controller precisely translates and rotates the robot joints, with mean steady-state errors of 0.032 mm and 0.447°, respectively. MRI-compatibility testing in a 3-Tesla closed-bore scanner has shown that the robot has no impact on the signal-to-noise ratio, and that geometric distortion remains within recommended calibration limits for the scanner. These results demonstrate that pneumatic actuation is a promising solution for neurosurgical interventions that either require or can benefit from sub-millimeter precision. Additionally, this paper provides a detailed solution to the controls problems imposed by severe nonlinearities in the pneumatic system, which has not previously been discussed in the context of MR-compatible devices.

Manuscript 2 (Chapter 3): *Design and Control of an MR-Compatible Additively Manufactured Needle Steering Robot*, D. B. Comber, J. E. Slightam, V. R. Gervasi, J. S. Neimat, and E. J. Barth

From: *IEEE Transactions on Robotics,* In Press.

Abstract: Fluid power actuators (hydraulic and pneumatic) are well suited for electromagnetically sensitive environments like magnetic resonance imaging (MRI) machines. Such actuators would enable intraoperative MRI guidance of robotically steerable needles. Yet, a technical barrier to using fluid power in MRI-guided surgical systems is the absence of commercial, off-the-shelf fluid power actuators that are sterilizable and inherently safe. This paper reports the design, modeling, and control of an additively manufactured pneumatic stepper actuator. Designed using corrugated diaphragm theory, one helix-shaped bellows and one toroid-shaped bellows provide pure rotation and pure translation, respectively. The entire actuator module functions as a two degree-of-freedom needle driver; that is, the two bellows directly translate and rotate the base of one tube of a steerable needle. Several of these modules can be cascaded together as a complete actuation unit for steerable needles comprising multiple, concentric tubes. For needle tip translations and rotations, mechanical stops limit the bellows' movements to maximum unplanned step sizes of 0.5 mm and 0.5 degrees, which are acceptably safe in the event of a systems failure. Additively manufactured by selective laser sintering of nylon powder, the prototype device is compact and hermetically sealed for sterilizability. The linear bellows produced peak forces of 33 N and -26.5 N

for needle insertion and retraction, respectively. The rotary bellows produced peak torques of ±68 mN·m. Sub-step control allows translations and rotations less than full step increments; steady-state errors of 0.013 mm and 0.018 degrees were achieved.

Manuscript 3 (Chapter 4): *Design and Validation of a Concentric Tube Robot for MRI-Guided Hippocampotomy*, D. B. Comber, E. B. Pitt, Y. Chen, C. H. Grimes, J. S. Neimat, E. J. Barth, and R. J. Webster III

From: Manuscript in preparation for submission to *IEEE Transactions on Biomedical Engineering*

Abstract: This paper reports the design and validation of an MRI-guided concentric tube needle robot to treat epilepsy. The curved trajectory capabilities of this steerable needle enable access to the deep brain through the foramen ovale. This transforamenal approach would eliminate drilling of the skull and substantially minimize passage through untreated brain tissue. We hypothesized that a steerable needle comprising one superelastic tube of helical pre-curvature concentric with an inner, straight, ablation probe could traverse a follow-the-leader trajectory from the foramen ovale, to and through the hippocampus head-to-tail. To investigate the transforamenal approach, dual CT/MRI scans of a de-identified patient brain were registered and segmented. The resulting skull and hippocampus models were used to design a concentric tube needle. In simulation with this design, mean distance of the needle trajectory from the medial axis of the hippocampus was 0.88 mm. A superelastic nitinol tube was shape set to the helix corresponding to this planned trajectory. A radiofrequency ablation electrode was manufactured and tested. Accuracy of robotic control of the prototype needle was measured with an optical tracker. Needle tip position errors were 0.89, 1.14, and 1.02 mm for three placements. Robotic control was tested under MRI guidance using an MR-compatible actuation unit. For three placements in a phantom, needle tip errors were 3.07, 1.11, and 3.19 mm. Regarding MR-compatibility, no reduction in signal-to-noise ratio was observed with the robot in full motion. These results indicate that the robotic system reported here could feasibly enable a foramen ovale approach to epilepsy treatment.

Manuscript 4 (Chapter 5): *Optimization of Curvilinear Needle Trajectories for Transforamenal Hippocampotomy*, D. B. Comber, E. B. Pitt, H. B. Gilbert, M. W. Powelson, E. Matijevich, J. S. Neimat, R. J. Webster III, and E. J. Barth

From: Manuscript submitted to *Neurosurgery*, In Review.

Abstract:

Background: The recent development of MRI-guided laser-induced thermal therapy (LITT) offers a minimally-invasive alternative to craniotomies performed for tumor resection or for amydalohippocampectomy to control seizure disorders. Current LITT therapies rely on linear stereotactic trajectories that mandate twist-drill entry into the skull and potentially long approaches traversing healthy brain. The use of robotically-driven, telescoping, curved needles has the

potential to reduce procedure invasiveness by tailoring trajectories to the curved shape of the ablated structure and by enabling access through natural orifices.

Objective: This work investigated the feasibility of using a concentric tube robot to access the hippocampus through the foramen ovale to deliver thermal therapy and thereby provide a percutaneous treatment for epilepsy without drilling the skull.

Methods: The skull and both hippocampi were segmented from dual CT/MR image volumes for 10 patients. For each of the 20 hippocampi, a concentric tube robot was designed and optimized to traverse a trajectory from the foramen ovale to and through the hippocampus from head to tail.

Results: Across all 20 cases, the mean distances (error) between hippocampus medial axis and backbone of the needle were 0.55, 1.14, and 1.66 mm for best, mean, and worst case, respectively.

Conclusion: These curvilinear trajectories would provide accurate transforamenal delivery of an ablation probe to typical hippocampus volumes. This strategy has the potential to both decrease the invasiveness of the procedure while increasing the completeness of hippocampal ablation.

<u>References</u>

[1] K. Cleary and T.M. Peters, "Image-Guided Interventions: Technology Review and Clinical Applications," *Annu. Rev. Biomed. Eng.*, 12:119-142, 2010.

[2] T. Hartkens, D.L. Hill, A.D. Castellano-Smith, D.J. Hawkes, C.R. Maurer Jr, A.J. Martin, and C.L. Truwit, "Measurement and analysis of brain deformation during neurosurgery," *IEEE Trans. Medical Imaging,* 22(1):82-92, 2003.

[3] N. Foroglou, A. Zamani, and P. Black, "Intra-operative MRI (iop-MR) for brain tumour surgery," *British Journal of Neurosurgery*, 23(1):14-22, 2009.

[4] A. Krieger, R. Susil, C. Menard, J. Coleman, G. Fichtinger, E. Atalar, and L. Whitcomb. "Design of a Novel MRI Compatible Manipulator for Image Guided Prostate Interventions," *IEEE Trans. Bio-Med. Eng.*, 52(2):306-313, 2005.

[5] A. Krieger, I. Iordachita, S. Song, N. Cho, P. Guion, G. Fichtinger, and L. Whitcomb. "Development and Prelimary Evaluation of an Actuated MRI-Compatible Robotic Device for MRI-Guided Prostate Intervention," *IEEE ICRA*, Anchorage, AK, pp. 1066-1073, 2010.

[6] D. Kim, E. Kobayashi, T. Dohi, and I. Sakuma. "A New, Compact MR-Compatible Surgical Manipulator for Minimally Invasive Liver Surgery," *Medical Image Computing and Computer Assisted Intervention*, 2488, pp. 99-106, 2002.

[7] R. Moser, R. Gassert, E. Burdet, L. Sache, H.R. Woodtli, W. Maeder, and H. Bleuler. "An MR Compatible Robot Technology," *IEEE ICRA*, Taipei, Taiwan, pp. 670-675, 2003.

[8] H. Elhawary, A. Zivanovic, B. Davies, and M. Lampérth. "A Review of Magnetic Resonance Imaging Compatible Manipulators in Surgery," *Proc IMechE, Part H: J. of Engineering in Medicine*, 220(3):413-424, 2006.

[9] N. Tsekos, A. Khanicheh, E. Christoforou, and C. Mavroidis. "Magnetic Resonance-Compatible Robotic and Mechatronic Systems for Image-Guided Interventions and Rehabilitation: A Review Study," *Annu. Rev. Biomed. Eng.*, 9:351-387, 2007.

[10] K. Masamune, E. Kobayashi, Y. Masutani, M. Suzuki, T. Dohi, H. Iseki, and K. Takakura. "Development of an MRI-Compatible Needle Insertion Manipulator for Stereotactic Neurosurgery," *J Image Guid Surg.*, 1(4):242-248, 1995.

[11] B. Larson, A. Erdman, N. Tsekos, E. Yacoub, P. Tsekos, and I. Koutlas. "Design of an MRI-Compatible Robotic Stereotactic Device for Minimally Invasive Interventions in the Breast," *J. Biomech. Eng.*, 126(4):458-465, 2004.

[12] Y. Wang, G. Cole, H. Su, J. Pilitsis, and G. Fischer. "MRI Compatibility Evaluation of a Piezoelectric Actuator System for a Neural Interventional Robot," *IEEE EMBC*, Minneapolis, MN, pp. 6072-6075, 2009.

[13] H. Su, G.A. Cole, and G.S. Fischer. "High-field MRI-Compatible Needle Placement Robots for Prostate Interventions: Pneumatic and Piezoelectric Approaches," *Advances in Robotics and Virtual Reality*, eds. T. Gulrez and A. Hassanien, Springer-Verlag, Chap. 1, 2011.

[14] S.O.R. Pfleiderer, J.R. Reichenbach, T. Azhari, C. Marx, A. Malich, A. Schneider, J. Vagner, H. Fischer, and W.A. Kaiser. "A Manipulator System for 14-Gauge Large Core Breast Biopsies Inside a High-Field Whole Body MR Scanner," *J Magn Reson Imaging*, 17, pp. 493-498, 2003.

[15] S. Pandya, J.W. Motkoski, C. Serrano-Almeida, A.D. Greer, I. Latour, and G.R. Sutherland. "Advancing neurosurgery with image-guided robotics," *J Neurosurg*, 111(6):1141-1149, 2009.

[16] G. Sutherland, I. Latour, A.D. Greer, T. Fielding, G. Feil, and P. Newhook. "An Image-Guided Magnetic Resonance-Compatible Surgical Robot," *Neurosurgery*, 62(2):286-293, 2008.

[17] N. Yu, C. Hollnagel, A. Blickenstorfer, S. Kollias, and R. Riener. "Comparison of MRI-Compatible Mechatronic Systems with Hydrodynamic and Pneumatic Actuation," *IEEE/ASME Trans. Mechatronics*, 13(3):268-277, 2008.

[18] D. Stoianovici, A. Patriciu, D. Petrisor, D. Mazilu, and L. Kavoussi. "A New Type of Motor: Pneumatic Step Motor," *IEEE/ASME Trans. Mechatronics*, 12(1):98-106, 2007.

[19] M. Muntener, A. Patriciu, D. Petrisor, M. Schar, D. Ursu, D. Song, and D. Stoianovici. "Transperineal Prostate Intervention: Robot for Fully Automated MR Imaging—System Description and Proof of Principle in a Canine Model," *J. Radiology*, 247(2):543-549, 2008.

[20] Y. Chen, C. D. Mershon, and Z. T. H. Tse. "A 10-mm MR-Conditional Unidirectional Pneumatic Stepper Motor," *IEEE/ASME Trans Mechatronics*, *20*(2):782-788, 2015.

[21] H. Sajima, H. Kamiuchi, K. Kuwana, T. Dohi, and K. Masamune. "MR-Safe Pneumatic Rotation Stepping Actuator," *J Robotics and Mechatronics*, 24(5):820-827, 2012.

[22] A. Melzer, B. Gutmann, T. Remmele, R. Wolf, A. Lukoscheck, M. Bock, H. Bardenheuer, and H. Fischer. "INNOMOTION for Percutaneous Image-Guided Interventions: Principles and

Evaluation of this MR- and CT-Compatible Robotic System," *IEEE Eng Med Biol Mag*, pp. 66-73, May/June 2008.

[23] B. Yang, U-X. Tan, A. McMillan, R. Gullapalli, and J.P. Desai. "Design and Implementation of a Pneumatically-Actuated Robot for Breast Biopsy under Continuous MRI," *IEEE Int Conf Robot Autom*, Shanghai, pp. 674-679, 2011.

[24] N. Zemiti, I. Bricault, C. Fouard, B. Sanchez, and P. Cinquin. "LPR: A CT and MR-Compatible Puncture Robot to Enhance Accuracy and Safety of Image-Guided Interventions," *IEEE/ASME Trans. Mechatronics*, 13(3):306-315, 2008.

[25] G. Fischer, I. Iordachita, C. Csoma, J. Tokuda, S. DiMaio, C. Tempany, N. Hata, and G. Fichtinger. "MRI-Compatible Pneumatic Robot for Transperineal Prostate Needle Placement," *IEEE/ASME Trans. Mechatronics*, 13(3):295-305, 2008.

[26] M.R. van den Bosch, M.R. Moman, M. van Vulpen, J.J. Battermann, E. Duiveman, L.J. van Schelven, H. de Leeuw, J.J.W. Lagendjik, and M.A. Moerland. "MRI-guided robotic system for transperineal prostate interventions: proof of principle," *Phys Med Biol*, 55:133-140, 2010.

[27] K.J. Macura and D. Stoianovici. "Advancements in Magnetic Resonance-Guided Robotic Interventions in the Prostate," *Top Magn Reson Imaging*, 19(6):297-304, 2008.

[28] S. Song, N. Cho, J. Tokuda, N. Hata, C. Tempany, G. Fichtinger, and I. Iordachita. "Preliminary Evaulation of a MRI-compatible Modular Robotic System for MRI-guided Prostate Interventions," *IEEE RAS & EMBS*, Tokyo, Japan, pp. 796-801, 2010.

[29] D. Ben-Dov and S. Salcudean. "A Force-Controlled Pneumatic Actuator," *IEEE Trans Robotics & Automation*, 11(6):906-911, 1995.

[30] E. Richer and Y. Hurmuzlu. "A High Performance Pneumatic Force Actuator System: Part 1—Nonlinear Mathematical Model," *ASME J Dyn. Syst., Meas. Control*, 122(3):416-425, 2000.

[31] E. Richer and Y. Hurmuzlu. "A High Performance Pneumatic Force Actuator System: Part 2—Nonlinear Controller Design," *ASME J. Dyn. Syst., Meas. Control*, 122(3):426-434, 2000.

[32] J.-J. Slotine and W. Li. *Applied Nonlinear Control*, Prentice Hall, Englewood Cliffs, New Jersey, Chap. 7, pp. 278, 1991.

[33] G.M. Bone and S. Ning. "Experimental Comparison of Position Tracking Control Algorithms for Pneumatic Cylinder Actuators," *IEEE/ASME Trans Mechatronics*, 12(5):557-561, 2007.

[34] S. Chillari, S. Guccione, and G. Muscato. "An Experimental Comparison Between Several Pneumatic Position Control Methods," *Proc 40th IEEE Conf Decision and Control*, Orlando, FL, pp. 1168-1173, 2001.

[35] B. Yang, U-X. Tan, A. McMillan, R. Gullapalli, and J.P. Desai. "Design and Control of a 1-DOF MRI-Compatible Pneumatically Actuated Robot with Long Transmission Lines," *IEEE/ASME Trans Mechatronics*, 16(6):1040-1048, 2011.

[36] Y. Zhu and E. Barth. "Accurate Sub-Millimeter Servo-Pneumatic Tracking using Model Reference Adaptive Control (MRAC)," *International Journal of Fluid Power*, 11(2):43-55, 2010.

[37] M.J. Drexel, G.S. Selvaduray, and A.R. Pelton, "The Effects of Cold Work and Heat Treatment on the Properties of Nitinol Wire," *Proceedings of the International Conference on Shape Memory and Superelastic Technologies*, pages 447–454, 2006.

[38] A.R. Pelton, S.M. Russell, and J. DiCello. "The Physical Metallurgy of Nitinol for Medical Applications," *Journal of Metals*, 55(5):33–37, 2003.

[39] H. Su, D.C. Cardona, W. Shang, A. Camilo, G.A. Cole, D.C. Rucker, R.J. Webster III, and G.S. Fischer. "A MRI-Guided Concentric Tube Continuum Robot with Piezoelectric Actuation: A Feasibility Study," *IEEE International Conference on Robotics and Automation*, pp. 1939-1945, 2012.

[40] J. Burgner, D.C. Rucker, H.B. Gilbert, P.J. Swaney, P.T. Russell, K.D. Weaver, and R.J. Webster III. "A Telerobotic System for Transnasal Surgery," *IEEE/ASME Trans Mechatronics,* 19(3):996-1006, 2014.

[41] J. Burgner, P.J. Swaney, R.A. Lathrop, K.D. Weaver, and R.J. Webster III. "Debulking From Within: A Robotic Steerable Cannula for Intracerebral Hemorrhage Evacuation," *IEEE Transactions on Biomedical Engineering*, 60(9):2567-2575, 2013.

[42] D.C. Rucker, R.J. Webster III, G.S. Chirikjian, and N.J. Cowan. "Equilibrium conformations of concentric tube continuum robots," *International Journal of Robotics Research*, 29(10):1263–1280, 2010.

[43] D.C. Rucker, B.A. Jones, and R.J. Webster III. "A geometrically exact model for externally loaded concentric tube continuum robots," *IEEE Transactions on Robotics*, 26(5):769–780, 2010.

[44] R.J. Webster III and B.A. Jones. "Design and kinematic modeling of constant curvature continuum robots: A review," *International Journal of Robotics Research*, 29(13):1661-1683, 2010.

[45] D.C. Rucker and R.J. Webster III. "Parsimonious evaluation of concentric-tube continuum robot equilibrium conformation," *IEEE Transactions on Biomedical Engineering*, 56(9):2308–2311, 2009.

[46] R.J. Webster III, J.M. Romano, and N.J. Cowan. "Mechanics of precurved-tube continuum robots," *IEEE Transactions on Robotics*, 25(1):67–78, 2009.

[47] P.E. Dupont, J. Lock, B. Itkowitz, and E. Butler. "Design and control of concentric-tube robots," *IEEE Trans Robotics*, 26(2):209–225, 2010.

[48] P. Kwan and M.J. Brodie. "Early identification of refractory epilepsy," *N Engl J Med*, 342(5):314-319, 2000.

[49] "Curing the Epilepsies: The Promise of Research," 2014 Apr 28. Retrieved 2014 Jun 14, from http://www.ninds.nih.gov/disorders/epilepsy/epilepsy_research.htm

[50] S. Wiebe, W.T. Blume, J.P. Girvin, and M. Eliasziw. "A randomized, controlled trial of surgery for temporal-lobe epilepsy," *N Engl J Med*, 345(5):311-318, 2001.

[51] H. Choi, R.L. Sell, L. Lenert, P. Muennig, R.R. Goodman, F.G. Gilliam, and J.B. Wong. "Epilepsy surgery for pharmacoresistant temporal lobe epilepsy: a decision analysis," *JAMA*, 300(21):2497-2505, 2008.

[52] S.D. Lhatoo, J.K. Solomon, A.W. McEvoy, N.D. Kitchen, S.D. Shorvon, and J.W. Sander. "A prospective study of the requirement for and the provision of epilepsy surgery in the United Kingdom," Epilepsia, 44(5):673-676, 2003.

[53] C.E. Begley, J.F. Annegers, D.R. Lairson, T.F. Reynolds, and W.A. Hauser. "Cost of epilepsy in the United States: a model based on incidence and prognosis," *Epilepsia*, 35(6):1230-1243, 1994.

[54] S.F. Berkovic, A.M. McIntosh, R.M. Kalnins, G.D. Jackson, G.C.A. Fabinyi, G.A. Brazenor, P.F. Bladin, and J.L. Hopper. "Preoperative MRI predicts outcome of temporal lobectomy: an actuarial analysis," *Neurology*, 45(7):1358-1363, 1995.

[55] S.G. Uijl, F.S.S. Leijten, K.G.M. Moons, E.P.H.M. Veltman, C.H. Ferrier, and C.A. van Donselaar. "Epilepsy surgery can help more adult patients with intractable seizures," *J Epilepsy Research*, 101(3):210-216, 2012.

[56] J. Engel Jr., S. Wiebe, J. French, M. Sperling, P. Williamson, D. Spencer, R. Gumnit, C. Zahn, E. Westbrook, and B. Enos. "Practice parameter: temporal lobe and localized neocortical resections for epilepsy: report of the Quality Standards Subcommittee of the American Academy of Neurology, in association with the American Epilepsy Society and the American Association of Neurological Surgeons," *Neurology*, 60(4):538-547, 2003.

[57] P. de Flon, E. Kumlien, C. Reuterwall, and P. Mattsson. "Empirical evidence of underutilization of referrals for epilepsy surgery evaluation," *Eur J Neurol*, 17(4):619-625, 2010.

[58] J.I. Sirven, 2010. "The silent gap between epilepsy surgery evaluations and clinical practice guidelines," *Eur J Neurol*, **17**(4):522-523.

[59] D.M. Ficker, E.L. So, W.K. Shen, J.F. Annegers, P.C. O'Brien, G.D. Cascino, and P.G. Belau. "Population-based study of the incidence of sudden unexplained death in epilepsy," *Neurology*, 51(5):1270-1274, 1998.

[60] M.R. Sperling, 2001. "Sudden Unexplained Death in Epilepsy," *Epilepsy Curr,* 1(1):21-23.

[61] J.T. Willie, N.G. Laxpati, D.L. Drane, A. Gowda, C. Appin, C. Hao, D.J. Brat, S.L. Helmers, A. Saindane, S.G. Nour, and R.E. Gross. "Real-Time Magnetic Resonance-Guided Stereotactic Laser Amygdalohippocampotomy for Mesial Temporal Lobe Epilepsy," *Neurosurgery,* 14(6):569-585, 2014.

[62] D.A. Woodrum, L.A. Mynderse, K.R. Gorny, K.K. Amrami, R.J. McNichols, and M.R. Callstrom. "3.0T MR-Guided Laser Ablation of a Prostate Cancer Recurrence in the Postsurgical Prostate Bed". *J Vasc Interv Radiol*, 22, pp. 929-934, 2011.

[63] D.J. Curry, A. Gowdy, R.J. McNichols, and A.A. Wilfong. "MR-Guided Stereotactic Ablation of Epileptogenic Foci in Children". *Epilepsy and Behavior*, 24(4), August, pp. 408-414, 2012.

[64] A. Carpentier, R.J. McNichols, R.J. Stafford, J. Itcovitz, J.P. Guichard, D. Reizine, S. Delalog, E. Vicaut, D. Payen, A. Gowda, and B. George. "Real-Time Magnetic Resonance-Guided Laser Thermal Therapy for Focal Metastatic Brain Tumors," *Neurosurgery*, 63(1):21-29, July 2008.

[65] P.S. Larson, P.A. Starr, G. Bates, L. Tansey, R.M. Richardson, and A.J. Martin. "An Optimized System for Interventional MRI Guided Stereotactic Surgery: Preliminary Evaluation of Targeting Accuracy," Neurosurgery, 70(Operative):95-103, 2012.

[66] A.H. Hawasli, S. Bagade, J.S. Shimony, M. Miller-Thomas, and E.C. Leuthardt. "Magnetic Resonance Imaging-Guided Focused Laser Interstitial Thermal Therapy for Intracranial Lesions: Single-Institution Series," Neurosurgery, 73(6):1000-1017, 2013.

[67] G. Rahmathulla, P.F. Recinos, J.E. Valerio, S. Chao, and G.H. Barnett. "Laser Interstitial Thermal Therapy for Focal Cerebral Radiation Necrosis: A Case Report and Literature Review," Stereotactic and Functional Neurosurgery, 90(3):192-200, 2012.

[68] A.G. Parrent and W.T. Blume. "Stereotactic amygdalohippocampotomy for the treatment of medial temporal lobe epilepsy," *Epilepsia*, 40(10):1408-1416, 1999.

[69] W.D. Yang, Q. Yu, J.N. Zhang, C.H. Shen, F.L. Wang, L.Y. Cui, H. Li, and S.Y. Yang. "Stereotactic combined amygdala and hippocampus lesions for treatment of medial temporal lobe epilepsy," *Chinese J Surgery*, 43(9):616-619, 2005.

Chapter 2 – Design and Control of a Magnetic Resonance Compatible Precision Pneumatic Robot

David B. Comber, Eric J. Barth, and Robert J. Webster III

Vanderbilt University, Nashville, TN

Prologue

This chapter describes the mechanical design and low-level control of a robotic actuation unit for motion control of a concentric tube robot under MRI guidance. The actuation unit employs pneumatic piston-cylinders and was fabricated by a combination of traditional machining and additive manufacturing. After submission of the manuscript, higher level controls were developed. Needle tip accuracy was quantified and is reported in the chapter's addendum.

Abstract

The versatile uses and excellent soft tissue distinction afforded by magnetic resonance imaging (MRI) has led to the development of many MR-compatible devices for MRI-guided interventions. This paper presents a fully pneumatic MR-compatible robotic platform designed for neurosurgical interventions. Actuated by non-magnetic pneumatic piston-cylinders, the robotic platform manipulates a five degree-of-freedom active cannula designed for deep brain interventions. Long lines of tubing connect the cylinders to remotely located pressure sensors and valves, and MRI-compatible optical sensors mounted on the robot provide the robot joint positions. A robust, nonlinear, model-based controller precisely translates and rotates the robot joints, with mean steady-state errors of 0.032 mm and 0.447°, respectively. MRI-compatibility testing in a 3-Tesla closed-bore scanner has shown that the robot has no impact on the signal-to-noise ratio, and that geometric distortion remains within recommended calibration limits for the scanner. These results demonstrate that pneumatic actuation is a promising solution for neurosurgical interventions that either require or can benefit from sub-millimeter precision. Additionally, this paper provides a detailed solution to the controls problems imposed by severe nonlinearities in the pneumatic system, which has not previously been discussed in the context of MR-compatible devices.

I. Introduction

Magnetic resonance imaging (MRI) offers several advantages for image-guided interventions

in comparison to other imaging modalities such as ultrasound, x-ray fluoroscopy, and computed tomography. Providing excellent soft tissue distinction through a wide variety of contrast methods, MRI does not expose the patient or clinicians to radiation. Additionally, because MRI is a three-dimensional modality, the orientation of image slices can easily be modified with no need to reposition the patient or imaging equipment [1, 2].

Harnessing these benefits, MRI-guided interventions have the potential to reduce invasiveness and increase accuracy of a procedure, thereby improving patient outcome. Particularly amenable to MRI guidance are needle-based interventions such as biopsy, brachytherapy, ablation, electrode placement, and deep brain stimulation. Already, some of these treatments have been clinically demonstrated with MRI guidance. For instance, using MR thermometry for thermal dose monitoring, MRI-guided laser ablation has been performed for prostate cancer as well as for epileptogenic foci and metastatic brain tumors [3-5]. However, many interventions cannot yet employ MRI guidance because clinician access to the patient is substantially limited by the confined space of a closed-bore diagnostic scanner.

MR-compatible robotic systems are a promising solution to this problem, and development of such devices began during the 1990s, with the first robotic platform reported in 1995 by Masamune et al. [6]. Using six piezoelectric motors, the robot positioned a needle for stereotactic neurosurgery, but the motors substantially degraded the MRI image quality. In the years that followed, designs for MR-compatible robots attempted to avoid this problem by locating the piezoelectric motors farther from the imaging volume or by electromagnetically isolating the motor drives from the scanner room. However, many of these devices still produced unacceptable levels of signal noise that precluded manipulator actuation during MR imaging, as described in a 2007 review by Tsekos et al. [1].

Several robotic systems employing piezoelectric motors inside high-field scanners have been reported to have little to no negative effect on image quality [2, 7-9]. Quite recently, Su et al. reported a very small loss in signal-to-noise ratio (SNR) of 2% during simultaneous imaging and servoing of piezoelectric motors; non-harmonic motors were selected for reduced noise and the commercial motor driver boards were replaced with custom, low-noise drivers [2]. Clinical use of piezoelectric-driven robotic systems has also been demonstrated. Pfleiderer et al. reported clinical testing of a piezoelectric robotic system with a manual biopsy gun for breast lesion diagnosis [7]. Pandya et al. reported several tumor resections using NeuroArm, two MRI-guided, piezoelectrically-actuated arms each of seven degrees of freedom [10, 9].

Nonetheless, in regards to MR-compatibility, fluid power actuators have the advantage over their piezoelectric counterparts of being able to completely eliminate the need for electric and magnetic components in the scanner room [2]. The creators of INNOMOTION, an MR-compatible robotic system commercially available in Europe, used piezoelectric motors in an early version of the robot. However, reduction in image quality and the risk of inductive heating led the team to an

improved design with pneumatic piston-cylinders, engineered for safety and controllability through high dynamic and low static friction characteristics [11]. In other research efforts, pneumatic piston-cylinders have been used in several MRI-guided needle placement robots designed to diagnose and treat cancers of the prostate and breast [12, 13]. Robots employing intrinsically fail-safe pneumatic stepper mechanisms have demonstrated successful image-guided interventions in pig abdomens and canine prostates [14, 15]. MRI-guided needle placement for prostate biopsy and brachytherapy has been clinically performed with robots actuated either by a one-axis pneumatic needle drive or fully manually [16, 17].

Precision control of pneumatic piston-cylinders is a difficult task due to the nonlinear compressibility of the working fluid. The actuator dynamics are third order in terms of piston position, since the input to the typical 5-port/4-way control valve is a mass flow rate, which leads to rate of change in chamber pressure and volume. Ning and Bone demonstrated that a nonlinear model-based controller outperforms a linearized model-based approach [18]. Similarly, Chillari et al. compared the performance of several pneumatic position control methods, and concluded a nonlinear approach is preferable to PID control [19]. Advancing the development of nonlinear, model-based controllers, Richer and Hurmuzlu introduced a detailed mathematical model for the actuator-valve system dynamics [20]. Using this model, Zhu and Barth achieved 0.05 mm accuracy using a composite adaptive and sliding mode force controller for an industrial robot [21]. In research related to the work presented here, Comber et al. achieved 0.006 mm steady-state error using model-based sliding mode control [22]. This control was for a single translational stage in the absence of cannula interaction forces or kinematic stage coupling implemented through rod-locks. This prior work is now extended to include these considerations.

To the authors' best knowledge, this paper presents the first fully pneumatic robot to be designed for neurosurgical interventions. This is also the first pneumatic robot specifically designed to control a steerable needle; a prior device with similar objectives used piezoelectric actuators [23]. Section 2 describes the mechanical design of the robotic platform to manipulate this active cannula, which is a continuum robot made from concentric precurved elastic tubes (see [24, 25] and references therein as overviews). A model-based, nonlinear controller for the pneumatic actuators is presented in section 3. In section 4 experimental results demonstrate precision positioning of the robot base joints, and conclusions are provided in section 5.

II. Mechanical Design of Robot

The design of an MR-compatible robot presents several challenges. Acceptable materials and actuators for the device are strictly limited to non-ferromagnetic and primarily non-metallic choices, due to the static and changing magnetic fields of the MR scanner. Additionally, the robot must be sufficiently compact to fit inside the scanner with the patient. To satisfy these restrictions while ensuring a high level of accuracy and robustness in the robot mechanisms, pneumatic piston-

cylinders known to be MR-compatible were selected, as depicted in Fig. 2.1. A five degree-of-freedom active cannula was designed for deep brain ablation procedures (the robot provides a tube that can deliver a fiber laser or a variety of other thermal ablation probes), and a robotic platform to manipulate the cannula was designed and built, as shown in Fig. 2.2.

Pneumatic Actuator with Fail-Safe Rod Lock

MR-compatible pneumatic piston-cylinders were selected as actuators. In comparison to hydraulic actuation, advantages of pneumatics in surgery include easy integration into existing instrument air facilities in hospitals and no mess for small leaks in the pneumatic system. In comparison to many piezoelectric motors, pneumatic actuators allow for robot servoing during MR imaging because they are free from electrical presences. The actuators (Airpot anti-stiction Airpel model E9 non-magnetic piston-cylinders) comprise a glass cylinder with 9.30 mm (0.366 inch) bore, graphite piston, graphite rod seal, and plastic components. A brass piston rod and mount are the only metallic parts. Rated to 690 kPa (100 psi) gage, the actuator provides a maximum force of 46.8 N (10.5 lbf).

Building on the rod lock concept of Fischer et al. [12], we designed a new type of fail-safe rod lock that is easy to manufacture by rapid prototyping, and facilitates tuning of the locking force. Figure 2.1 depicts a cross-sectional view of the rod lock fastened to the head of the piston-cylinder. In the fail-safe state, a wave spring (Smalley part no. CS062-M2) presses a 0.125 inch (3.18 mm) aluminum Dremel collet against a washer with a beveled inner surface. Inserted between the cylinder head and the collet teeth, the beveled washer provides a way to adjust the clamping force of the collet on the piston rod; that is, the wave spring pre-load force is adjusted by slightly increasing or decreasing the distance to which the cylinder head is threaded into the rod lock body. Upon pressurization of the chamber formed by two sliding seals and the collet-carrying plunger, the collet disengages from the beveled washer. Unequal cross-sectional areas of contact between the plunger and the sliding seals provide a net force to the plunger, further depressing the wave spring and releasing the collet. The rod lock exhibited optimal performance at 85 psi gage (590
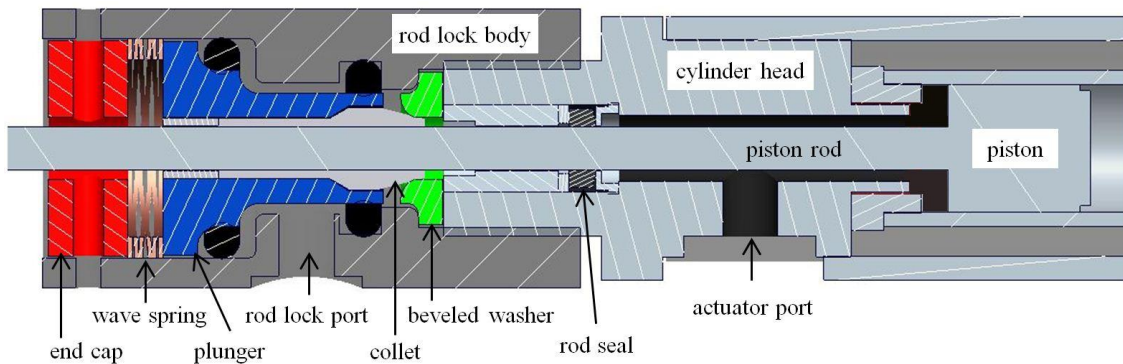
Figure 2.1 – Pneumatic piston-cylinder with fail-safe rod lock.

kPa), with plunger movement of approximately 1 mm from the engaged to disengaged position of the lock. The rod lock body, cap, plunger, and beveled washer were rapid prototyped of air-tight material, Krypton Green by Polyjet. Using the Polyjet technology allowed for smooth, fine surface finish with close tolerances; this was necessary to achieve good performance with the sliding seals. The material was selected for its ruggedness and high strength properties. The sliding seals were lightly lubricated to reduce friction and wear, and sharp edges on the Dremel collet were sanded to prevent sticking and wearing against the beveled washer.

Active Cannula Design

A three-tube active cannula was designed with a specific clinical application in mind, namely, a back-of-the-skull approach for needle-based ablation of temporal-lobe epileptogenic foci. Thermal ablation of the hippocampus was selected as a specific objective, since hippocampal sclerosis is the primary cause of temporal-lobe epilepsy [26, 27]. However, the modular nature of the robotic platform would easily accommodate active cannulas designed for other percutaneous interventions. Common to all active cannulas is the fundamental concept whereby a desired curved trajectory is obtained by telescoping and rotating the bases of the concentric, pre-curved tubes relative to one another.

For the three-tube design, the active cannula comprises an outer relatively stiff tube (potentially made of a metal like titanium, though this tube could also be nitinol) and two inner tubes of super-elastic nitinol. The inset in Fig. 2.2 shows the degrees of freedom of the cannula. The outer titanium tube provides a first degree of freedom for an initial insertion depth up to 7 inches. The middle tube, made of nitinol, is pre-curved at its front end to a curvature specified using the patient's pre-operative MRI. During the procedure this tube would first be rotated within the titanium tube to a desired orientation and then translated beyond the tip of the titanium tube. The innermost, nitinol tube is designed to mimic a straight, flexible ablation probe. To manipulate a device of this kind, a total of 3 translations and 2 rotations are required from the robotic platform.

Translational Mechanism Design

The three translational stages of the robot were designed and built by a novel configuration for piston-cylinder actuators. Conventionally, the cylinder is fixed while the piston and rod translate. However, the space limitations of the scanner gantry aperture led to a compact design in which the piston rod is fixed and the cylinder translates. As shown in Fig. 2.2, the first translational stage, for insertion of the titanium tube, comprises two linear plain bearings (Igus part no. FJUM-01-30) and an acrylic plate (T1) to which the titanium tube is rigidly fixed. To the rear side of this sliding plate the rod lock and cylinder head are rigidly fixed, and the free end of the piston rod is rigidly fixed to the stationary front plate of the robot frame. Manufacture by laser cutter enabled precision alignment of all axes. Two carbon fiber guide shafts of diameter 30 mm, precision machined to -
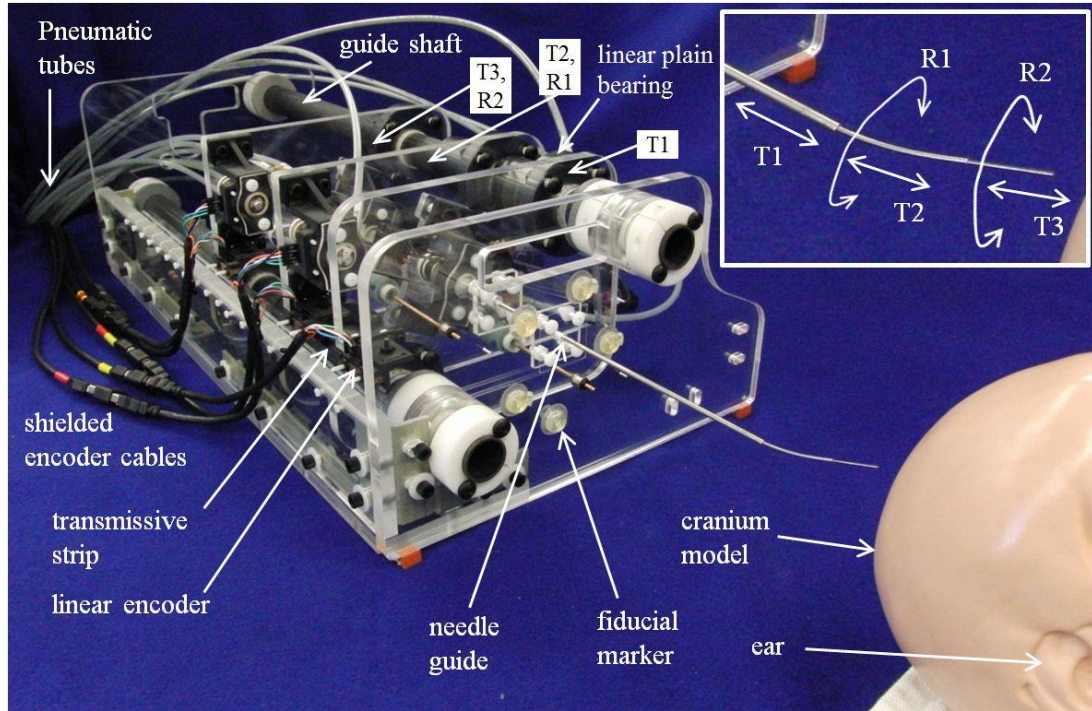
Figure 2.2 – Photograph of the robotic platform with cranium model. Inset shows the 5 DoF's corresponding to the labeled base joints.

0.1 mm tolerance, provide a low friction surface for translation of the linear plain bearings. Additionally the shafts provide structural rigidity to the stationary frame of the robot. The low friction behavior of the translational mechanism aids in precision control. The length of the linear bearings was carefully selected to ensure no binding of the sliding plate would occur due to the cantilever position of the actuating force axis relative to each bearing axis.

The second and third translational stages are designed similar to the first; each comprises an acrylic plate to which two linear bearings are mounted to translate the plate along the pair of guide shafts. The second stage translates the middle, pre-curved nitinol tube and the third stage translates the innermost nitinol tube. To translate the second stage, a piston-cylinder is mounted with the rod lock and cylinder head fixed to the rear side of sliding plate T2, and the free end of the piston rod fixed to sliding plate T1. Similarly, to translate the third stage, a piston-cylinder is mounted with the rock lock and cylinder head fixed to the rear side of sliding plate T3, and the free end of the piston rod fixed to sliding plate T2.

Thus, the three translational stages of the robotic platform are kinematically coupled together. As plate T1 translates forward, it pulls along with it plates T2 and T3. Similarly, additional forward translation of plate T2 (with plate T1 locked stationary) pulls plate T3 forward as well. As the three sliding plates collapse together, the actuators for translations 1 and 2 pass through clearance holes in plates T2 and T3. The stroke lengths of the three actuators for translations 1, 2 and 3 are, respectively, 7 in (178 mm), 3 in (76.2 mm), and 3 in (76.2 mm).

Rotational Mechanism Design

To rotate the base of each of the two nitinol tubes, identical linear-to-rotary transmissions were designed and built for each, as shown in Fig. 2.3. The rotational mechanism (R1) for the middle, pre-curved nitinol tube is mounted to the front side of plate T2. Similarly, the rotational mechanism (R2) for the innermost nitinol tube is mounted to the front side of plate T3. Each transmission comprises a timing belt stretched taught between two grooved pulleys of pitch diameter 19.1 mm. A two-piece belt clamp made of ABS plastic couples the free end of the piston rod to the timing belt, such that the pulleys rotate as the piston rod translates across the taught portion of the belt. The transmission ratio is 6.00 degrees rotation per mm of piston displacement. A maximum torque of 447 mN·m is achievable, and the maximum angular displacement of the pulley is 400 degrees.
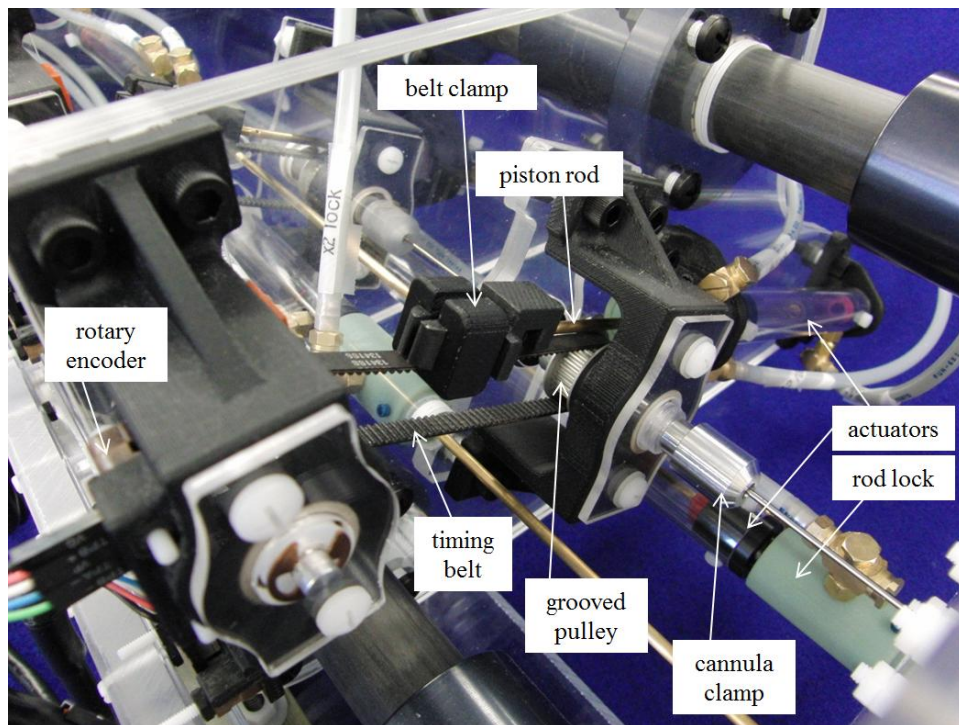
Figure 2.3 – Photograph of the linear-to-rotary transmission R1 mounted to plate T2.

The grooved pulley closest to the piston-cylinder rotates a custom-made aluminum shaft to which the nitinol tube is mounted using an aluminum Dremel collet. This tube clamping design can accommodate various cannula tube diameters by interchanging collets. The aluminum shaft is hollow to permit the ablator and cooling catheter to run along the inside of the active cannula. The shaft is supported by two ball bearings with glass balls and polyetheretherketone (PEEK) raceways (Igus part no. B626A7G). The bearing housings are made of ABS plastic and acrylic parts. The second grooved pulley is mounted to a solid shaft, which also supports a rotary encoder disc for optical position sensing of the piston displacement.

III. Robot Controller

Using sliding mode control (SMC) theory, a robust, nonlinear controller for the MR-compatible piston-cylinder was developed and first tested for a one degree-of-freedom needle insertion, as described by Comber et al. [28]. The controller was later implemented on the five degree-of-freedom platform and preliminary results were reported in [22, 29].

Design of Model-Based Sliding Mode Control

Due to unknown friction forces in the robot mechanisms as well as nonlinear behavior in the pneumatic system, namely the pressure dynamics and the mass flows through valve orifices, SMC was an appropriate choice for achieving sub-millimeter accuracy. Here, a brief derivation of the control law is presented. Referring to Fig. 2.4, the equation of motion for the sliding plate is given by

$$M\ddot{x} = P_2 A_2 - P_1 A_1 + P_{atm}\left(A_1 - A_2\right) \tag{1}$$

where $P_{1,2}$ and $A_{1,2}$ are the pressures and active cross-sectional areas of chambers 1 and 2, and atmospheric pressure is P_{atm}.
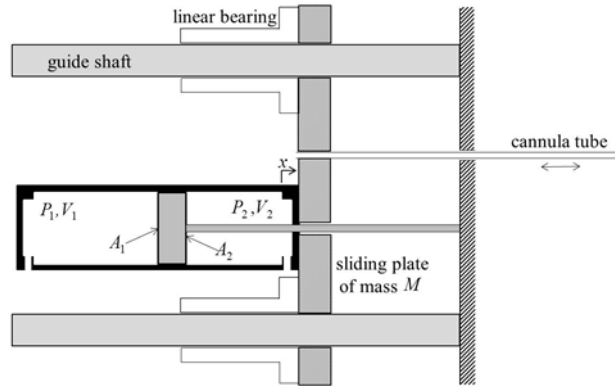
Figure 2.4 – Dynamics of the robot translational mechanism.

A 5-port/4-way spool valve was selected to control the actuator. For this type of actuator-valve system, a thorough derivation of the gas dynamics model can be found in [24]. These dynamics include the thermodynamics of the compressible gas in either cylinder chamber, as well as the mass flow through the valve orifice. Since a surgical intervention must be a safe, relatively slow procedure, a low bandwidth is sufficient and preferred for the controller. Therefore, the pressure dynamics are assumed to behave isothermally. From the mathematical model described in [24], the time derivative of each chamber pressure $\dot{P}_{1,2}$ is given for the isothermal case by

$$\dot{P}_i = \frac{RT}{V_i}\dot{m}_i - \frac{P_i\dot{V}_i}{V_i} \tag{2}$$

where R is the specific ideal gas constant, T the ambient temperature, and V_i the actuator chamber volume, including all dead volumes downstream of the valve.

To provide a single output from the control law to the spool valve, the mass flows $\dot{m}_i$ into the actuator chambers are expressed as the product of valve orifice area A_v and area-normalized mass flow Ψ_i, as follows:

$$\begin{aligned}
\dot{m}_1 &= -A_v\Psi_1(P_u,P_d) \\
\dot{m}_2 &= A_v\Psi_2(P_u,P_d)
\end{aligned} \tag{3}$$

The area-normalized mass flows are given by Eqns. (4)-(7), where P_u and P_d are the pressures upstream and downstream of the valve orifice and P_s is the supply pressure:

$$\Psi_1(P_u,P_d) = \begin{cases} \Psi(P_1,P_{atm}) & \text{for } A_v \geq 0 \\ \Psi(P_s,P_1) & \text{for } A_v < 0 \end{cases} \tag{4}$$

$$\Psi_2(P_u,P_d) = \begin{cases} \Psi(P_s,P_2) & \text{for } A_v \geq 0 \\ \Psi(P_2,P_{atm}) & \text{for } A_v < 0 \end{cases} \tag{5}$$

$$\Psi(P_u,P_d) = \begin{cases} \dfrac{C_1C_fP_u}{\sqrt{T}} & \text{(choked)} \\ \dfrac{C_2C_fP_u}{\sqrt{T}}\left(\dfrac{P_d}{P_u}\right)^{1/k}\sqrt{1-\left(\dfrac{P_d}{P_u}\right)^{(k-1)/k}} & \text{(unchoked)} \end{cases} \tag{6}$$

$$C_r = \left(\frac{2}{k+1}\right)^{\frac{k}{k-1}}, \; C_1 = \sqrt{\frac{k}{R}\left(\frac{2}{k+1}\right)^{(k+1)/(k-1)}}, \; C_2 = \sqrt{\frac{2k}{R(k-1)}} \tag{7}$$

The derivation of Eqns. (6) and (7) assumes isentropic flow through a thin-walled plate. Choked flow occurs when the pressure ratio of P_d over P_u is less than or equal to the critical ratio constant C_r. For the isothermal case, the temperature T of the flow is equal to ambient. The ratio of specific heats is $k = c_p/c_v$ and C_f is the dimensionless discharge coefficient dependent on valve orifice geometry.

A suitable SMC control law was formulated by choosing a third-order sliding surface acting on the integral of the position error $e = x - x_d$, where x_d is the desired position of the actuator. Equation (8) defines the sliding surface s, in which the desired closed-loop poles of the error dynamics are

introduced as $-\lambda$.

$$s=\left(\frac{d}{dt}+\lambda\right)^{3}\int e=\ddot{e}+3\lambda\dot{e}+3\lambda^{2}e+\lambda^{3}\int e \tag{8}$$

The system dynamics are third-order in position, and the affine control variable A_v appears by taking the time derivative of Eqn. (1) and substituting in Eqn. (2) to obtain:

$$M\,\dddot{x}=A_{2}\left(\frac{RT}{V_{2}}\dot{m}_{2}-\frac{P_{2}\dot{V}_{2}}{V_{2}}\right)-A_{1}\left(\frac{RT}{V_{1}}\dot{m}_{1}-\frac{P_{1}\dot{V}_{1}}{V_{1}}\right) \tag{9}$$

To achieve stable error dynamics, the Lyapunov candidate function $V=\frac{1}{2}s^{2}$ was chosen, and its time derivative, $\dot{V}=s\dot{s}$, was set equal to a negative definite function of choice. The function $\dot{V}_{\text{desired}}=-\eta\,s\cdot\operatorname{sat}(s/\phi)$ is a desirable choice because it forces the s dynamics and hence the error dynamics to exhibit a smoothly decaying behavior. This behavior is described by Eqn. (10), which was obtained by equating $\dot{V}$ to $\dot{V}_{\text{desired}}$. The saturation function $\operatorname{sat}(s/\phi)$ is bounded at ± 1; η is the positive-valued robustness constant of choice and ϕ the boundary layer.

$$\dot{s}=-\eta\operatorname{sat}(s/\phi) \tag{10}$$

Equations (11)-(13) present the SMC control law, obtained by taking the time derivative of Eqn. (8), setting the result equal to Eqn. (10), and substituting in Eqn. (9). In Eqn. (11), velocity was introduced by noting that $\dot{V}_{1}=-A_{1}\dot{x}$ and $\dot{V}_{2}=A_{2}\dot{x}$. This SMC control law ensures Lyapunov-stable closed-loop error dynamics for the robot controller.

$$A_{v}=\frac{\dddot{x}_{d}+f\left(P_{i},V_{i},\dot{x}\right)-3\lambda\ddot{e}-3\lambda^{2}\dot{e}-\lambda^{3}e-\eta\operatorname{sat}(s/\phi)}{g\left(V_{i},\Psi_{i}\right)} \tag{11}$$

$$f\left(P_{i},V_{i},\dot{x}\right)=\frac{1}{M}\left(A_{1}^{2}\frac{P_{1}}{V_{1}}+A_{2}^{2}\frac{P_{2}}{V_{2}}\right) \tag{12}$$

$$g\left(V_{i},\Psi_{i}\right)=\frac{RT}{M}\left(\frac{A_{1}}{V_{1}}\Psi_{1}+\frac{A_{2}}{V_{2}}\Psi_{2}\right) \tag{13}$$

Controller Electronics

Implementation of the model-based sliding mode controller requires position and pressure feedback from each actuator. One 19-inch long linear transmissive strip with 500 lines per inch (US Digital part no. LIN-500-19-6) is mounted along one side of the stationary robot frame, as shown in Fig. 2. Three optical linear encoder modules (US Digital part no. EM1-0-500-I) read the transmissive strip to provide the position of each translational stage of the robot. Similarly, for each of the two rotational stages of the robot, one optical rotary encoder module (U.S. Digital part no.

EM1-1-1250-I) reads a transmissive disc (U.S. Digital part no. HUBDISK-1-1250-236-IE) supported by one shaft of the pulley and timing belt assembly, as shown in Fig. 2.3. The optical encoder modules are known to be MR-compatible [12].

For position control of each actuator there is one 5-port/4-way proportional spool valve (Festo part no. MPYE-5-M5-010-B). Using manufacturer data, the mass flow discharge coefficient C_f for these valves was determined to be 0.2939 [28]. Charging and exhausting of the rod locks is accomplished by a valve manifold (Festo part no. 10P-10-4C-MP-V-Z) containing 5-port/2-way valves (Festo part no. CPV10-M1H-5LS-M7). In the de-energized state, the 2-way valve exhausts the rod lock for safety; thus, the rod lock is only pressurized when the 2-way valve is energized. Pressure feedback for the five actuators is provided by 10 pressure transducers (Festo part no. SDE-16-10V); there is one additional transducer to measure supply pressure (Festo part no. SPTW-P10R-G14-VD-M12). Transmission lines (polyurethane tubing, 4 mm I.D., 6 mm O.D.) connect the rod locks and piston-cylinders to remotely located valves and pressure sensors. These 3 meter long pneumatic lines can adequately separate the valves and pressure sensors from the scanner yet are not so long as to introduce non-negligible line dynamics.

The model-based sliding mode controller was created using MATLAB Simulink, which compiles and runs as C code on an xPC target machine. The target PC houses two data acquisition boards, and is designed to be located outside the scanner room. Double-shielded 5-meter long cables route the encoder signals from the robot to the target PC. Two 25-pin D-sub double-shielded cables connect the pressure sensors and valves to a break-out board that connects to the PC. These D-sub connectors will be used in future experiments to connect through the scanner room patch panel.

IV. Experimental Results

Following the manufacture of the robotic platform and the development of the model-based, SMC position control, actuation of the robot base joints was demonstrated. The MR-compatibility of the robot was also verified.

Robot Base Joint Control

The controller was tuned for each of the five DoF's, and the tuning parameters are listed in Table 1. Figure 5 demonstrates that the controller for the first translation is capable of tracking a square wave of 90 mm peak-to-peak amplitude, with a 2% settling time of 0.8 sec, mean steady-state error of 0.027 mm, and maximum overshoot of 0.006 mm (the encoder resolution). From a controls perspective, the square wave response is a good benchmark for controller performance, but a less aggressive trajectory would be desirable for surgical applications. Thus, for all five DoF's the controller was tested for endpoint positioning with a velocity of 16 mm/sec between endpoints.

Additionally, the desired trajectory was filtered by a second-order low pass filter at 1 Hz to achieve smooth transitioning between start and stop. During actuation of any given DoF, the remaining actuators were held stationary by their respective rod locks, thereby precluding the introduction of unwanted disturbances to the controller.

Table 2.1 – Controller tuning parameters by degree of freedom.

DoF	λ (Hz)	η (mm/s^3)	ϕ (mm/s^2)
T1	10	200	0.01
R1	15	200	0.01
T2	10	2000	0.002
R2	15	2000	0.01
T3	10	200	0.01
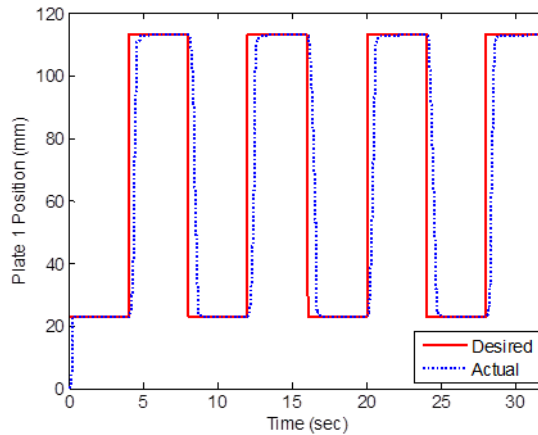
Figure 2.5 – First translation, position tracking of a square wave.

Endpoint to endpoint positioning for the first translation is shown in Fig. 2.6 along with two close-ups of the transition from transient to steady-state response. Inset A corresponds to needle insertion and inset B needle retraction. Note that the controller for the first translation sees the total mass of all three sliding plates (4 kg), as only the rod lock for the plate 1 actuator is disengaged during this operation. Figure 2.7 shows endpoint to endpoint positioning for the second translation. Here, plate 2 position is the change in position of plate 2 relative to plate 1, such that full retraction of the pre-curved cannula tube corresponds to 0 mm. Thus, inset A in Fig. 2.7 shows the precurved tube extending an arc length of 37 mm beyond the tip of the stiff outer tube, while inset B shows precurved tube retraction to a 7-mm arc length beyond the stiff tube tip. A substantial amount of friction is present due to the curved portion of the second tube rubbing against the inner wall of the stiff outer tube. Figure 2.7 demonstrates that the SMC controller can compensate for this unknown friction force. Endpoint to endpoint positioning for the third translation is shown in Fig. 2.8, with plate 3 position defined as the change in the position of plate 3 relative to plate 2. Thus, full

retraction of the simulated ablator probe (tube 3) corresponds to 0 mm in Fig. 2.8.
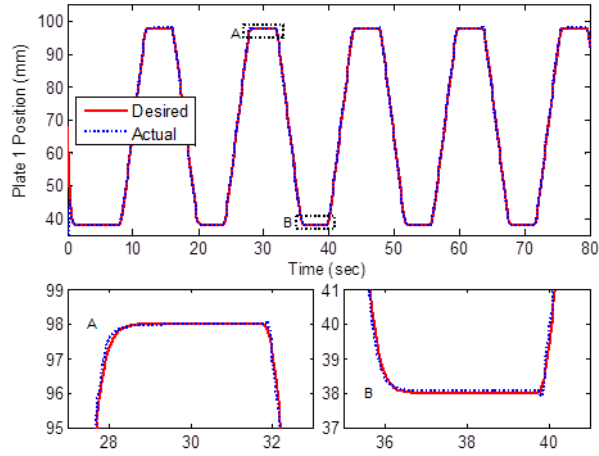
Figure 2.6 – First translation (T1), endpoint to endpoint positioning.
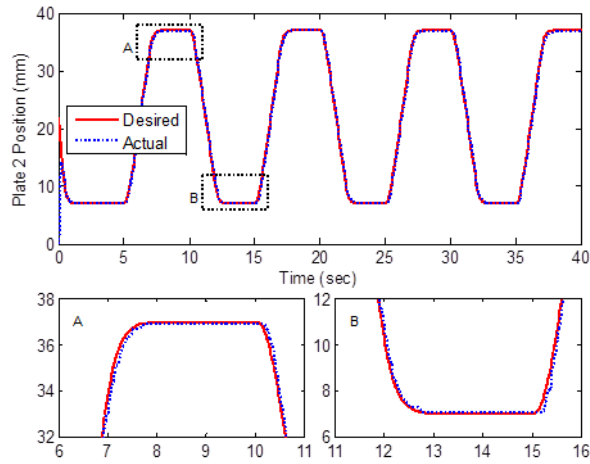
Figure 2.7 – Second translation (T2), endpoint to endpoint positioning.
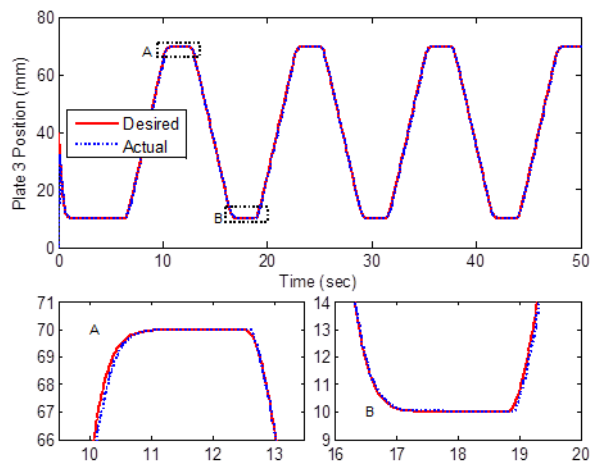
Figure 2.8 – Third translation (T3), endpoint to endpoint positioning.

Figures 2.9 and 2.10 demonstrate angular position control for the first and second rotational stages. During rotation of the precurved tube, the curved portion is entirely inside the stiff outer tube. This condition is the most demanding on the controller, as torsional interaction occurs between the precurved tube and outer tube. The controller can handle this behavior, as shown in Fig. 2.9. A summary of the mean and maximum steady-state errors for endpoint to endpoint positioning of each base joint is provided in Table 2.2. No overshoot occurred.
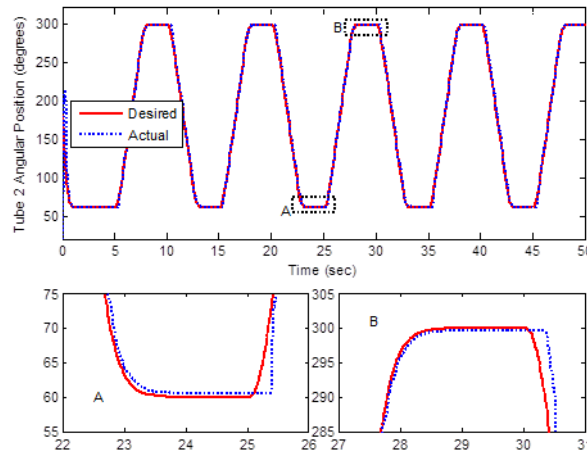
Figure 2.9 – First rotation (R1), point to point angular positioning.
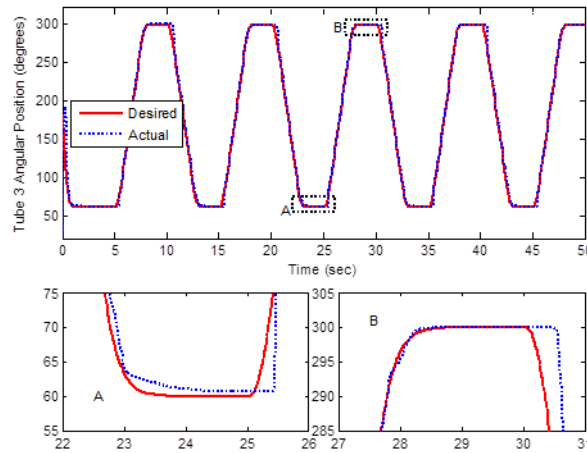
Figure 2.10 – Second rotation (R2), point to point angular positioning.

Table 2.2 – Summary of controller performance.

DoF	Mean steady-state error (mm)	Max steady-state error (mm)	Overshoot?
T1	0.028	0.062	No
R1	0.075 (0.451°)	0.128 (0.768°)	No
T2	0.058	0.081	No
R2	0.074 (0.442°)	0.128 (0.768°)	No
T3	0.010	0.020	No

MR-Compatibility Testing

Preliminary MR-compatibility testing of the robotic platform was done, primarily to verify that the small quantities of metals on the robot do not degrade the signal-to-noise ratio (SNR) by eddy currents. The robot was placed inside a Philips 3T Achieva scanner, with the front plate of the stationary robot frame directly behind the head coil. Four 3D images of an fBIRN phantom were acquired, both without and with the robot present. The imaging sequence was T1 weighted with FFE gradient echo and a voxel size of 2x2x2 mm. SNR was calculated for each data set as the ratio of the sum of the signal means over the sum of the signal standard deviations. SNR without the robot was 52.3 and SNR with the robot was 52.7.

The SNR results suggest that the calculated SNR is only meaningful to two significant figures, as it would not make sense that the SNR is 0.4 higher with the robot present. The SNR results do show that the metallic presences on the robot do not produce SNR-degrading eddy currents.

Additionally, MRI images of an ADNI phantom were taken with and without the robot adjacent. Analyzed by a third party service for MR distortion and image quality, the results indicated a maximum distortion of less than 1.3 mm along any dimension, which was within the recommended calibration limits for the particular MRI scanner used for this test.

V. Conclusions

The design and control of an MR-compatible precision pneumatic active cannula robot has been presented. A sliding mode controller for each of the robot's 5 DoF was formulated and implemented. The three translational DoF's exhibited positioning accuracies better than 100 µm, and the two rotational DoF's exhibited accuracies better than 1°. Based on the kinematic model of a similar active cannula presented in [30], these base-level positioning errors result in no greater than 0.78 mm cannula tip positioning error; this is smaller than the voxel size of most MR imagers. The MR compatibility of the robot was tested in a Philips 3T Achieva scanner and displayed no measurable effect on the SNR of an fBIRN phantom. Image distortion tests with an ADNI phantom indicate a maximum distortion of 1.3 mm. Future work includes cannula tip placement experiments and integration of the robotic platform with the MRI scanner. Scanner experiments will focus on providing both real-time feedback of the active cannula location as well as thermal dose monitoring of the ablator using MR thermometry.

Acknowledgment

References

[1] N. Tsekos, A. Khanicheh, E. Christoforou, and C. Mavroidis, "Magnetic Resonance-Compatible Robotic and Mechatronics Systems for Image-Guided Interventions and Rehabilitation: A Review Study," *Annu Rev Biomed Eng*, 9:351-387, 2007.

[2] H. Su, G.A. Cole, and G.S. Fischer, "High-field MRI-Compatible Needle Placement Robots for Prostate Interventions: Pneumatic and Piezoelectric Approaches," *Advances in Robotics and Virtual Reality*, eds. T. Gulrez and A. Hassanien, Springer-Verlag, Chap. 1, 2011.

[3] D.A. Woodrum, L.A. Mynderse, K.R. Gorny, K.K. Amrami, R.J. McNichols, and M.R. Callstrom, "3.0T MR-Guided Laser Ablation of a Prostate Cancer Recurrence in the Postsurgical Prostate Bed," *J Vasc Interv Radiol*, 22: 929-934, 2011.

[4] D.J. Curry, A. Gowdy, R.J. McNichols, and A.A. Wilfong, "MR-Guided Stereotactic Ablation of Epileptogenic Foci in Children," *Epilepsy and Behavior*, 24(4):408-414, 2012.

[5] A. Carpentier, R.J. McNichols, R.J. Stafford, J. Itcovitz, J.P. Guichard, D. Reizine, S. Delalog, E. Vicaut, D. Payen, A. Gowda, and B. George, "Real-Time Magnetic Resonance-Guided Laser Thermal Therapy for Focal Metastatic Brain Tumors," *Neurosurgery*, 63(1):21-29, 2008.

[6] K. Masamune, E. Kobayashi, Y. Masutani, M. Suzuki, T. Dohi, H. Iseki, and K. Takakura, "Development of an MRI-Compatible Needle Insertion Manipulator for Stereotactic Neurosurgery," *J Image Guid Surg*, 1:242-248, 1995.

[7] S.O.R. Pfleiderer, J.R. Reichenbach, T. Azhari, C. Marx, A. Malich, A. Schneider, J. Vagner, H. Fischer, and W.A. Kaiser, "A Manipulator System for 14-Gauge Large Core Breast Biopsies Inside a High-Field Whole Body MR Scanner," *J Magn Reson Imaging*, 17:493-498, 2003.

[8] B.T. Larson, A.G. Erdman, N.V. Tsekos, E. Yacoub, P.V. Tsekos, and I.G. Koutlas, "Design of an MRI-Compatible Robotic Stereotactic Device for Minimally Invasive Interventions in the Breast," *J Biomech Eng*, 126:458-465, 2004.

[9] G. Sutherland, I. Latour, A.D. Greer, T. Fielding, G. Feil, and P. Newhook, "An Image-Guided Magnetic Resonance-Compatible Surgical Robot," *Neurosurgery*, 62(2):286-293, 2008.

[10] S. Pandya, J.W. Motkoski, C. Serrano-Almeida, A.D. Greer, I. Latour, and G.R. Sutherland, "Advancing neurosurgery with image-guided robotics," *J Neurosurg*, 111(6):1141-1149, 2009.

[11] A. Melzer, B. Gutmann, T. Remmele, R. Wolf, A. Lukoscheck, M. Bock, H. Bardenheuer, and H. Fischer, "INNOMOTION for Percutaneous Image-Guided Interventions: Principles and Evaluation of this MR- and CT-Compatible Robotic System," *IEEE Eng Med Biol Mag*, pp. 66-73, 2008.

[12] G. Fischer, I. Iordachita, C. Csoma, J. Tokuda, S. DiMaio, C. Tempany, N. Hata, and G. Fichtinger, "MRI-Compatible Pneumatic Robot for Transperineal Prostate Needle Placement," *IEEE/ASME Trans Mechatronics*, 13(3):295-305, 2008.

[13] B. Yang, U.-X. Tan, A. McMillan, R. Gullapalli, and J.P Desai, "Design and Implementation of a Pneumatically-Actuated Robot for Breast Biopsy under Continuous MRI," *2011 IEEE Int Conf Robot Autom*, Shanghai, pp. 674-679, 2011.

[14] N. Zemiti, I. Bricault, C. Fouard, B. Sanchez, and P. Cinquin, "LPR: A CT and MR-Compatible Puncture Robot to Enhance Accuracy and Safety of Image-Guided Interventions," *IEEE/ASME Trans Mechatronics*, 13(3):306-315, 2008.

[15] M. Muntener, A. Patriciu, D. Petrisor, M. Schär, D. Ursu, D.Y. Song, and D. Stoianovici, "Transperineal Prostate Intervention: Robot for Fully Automated MR Imaging—System Description and Proof of Principle in a Canine Model," *Radiology*, 247(2):543-549, 2008.

[16] M.R. van den Bosch, M.R. Moman, M. van Vulpen, J.J. Battermann, E. Duiveman, L.J. van Schelven, H. de Leeuw, J.J.W. Lagendjik, and M.A. Moerland, "MRI-guided robotic system for transperineal prostate interventions: proof of principle," *Phys Med Biol*, 55:133-140, 2010.

[17] K.J. Macura and D. Stoianovici, "Advancements in Magnetic Resonance-Guided Robotic Interventions in the Prostate," *Top Magn Reson Imaging*, 19(6):297-304, 2008.

[18] G.M. Bone and S. Ning, "Experimental Comparison of Position Tracking Control Algorithms for Pneumatic Cylinder Actuators," *IEEE/ASME Trans Mechatronics*, 12(5):557-561, 2007.

[19] S. Chillari, S. Guccione, and G. Muscato, "An Experimental Comparison Between Several Pneumatic Position Control Methods," *Proc 40th IEEE Conf Decision and Control*, Orlando, FL, pp. 1168-1173, 2001.

[20] E. Richer and Y. Hurmuzlu, "A High Performance Pneumatic Force Actuator System: Part 1—Nonlinear Mathematical Model," *ASME J Dyn Syst, Meas Control*, 122(3):416-425, 2000.

[21] Y. Zhu and E.J. Barth, "Accurate Sub-Millimeter Servo-Pneumatic Tracking using Model Reference Adaptive Control (MRAC)," *Int J Fluid Power*, 11(2):49-57, 2010.

[22] D.B. Comber, D. Cardona, R.J. Webster III, and E.J. Barth, "Sliding Mode Control of an MRI-Compatible Pneumatically Actuated Robot," *2012 Bath/ASME Symp. Fluid Power & Motion Control*, D. N. Johnston and A. R. Plummer, eds., Centre for Power Transmission & Motion Control, University of Bath, UK, pp. 283-293.

[23] H. Su, D. Cardona, W. Shang, A. Camilo, G.A. Cole, D.C. Rucker, R.J. Webster III, and G.S. Fischer, "A MRI-Guided Concentric Tube Continuum Robot with Piezoelectric Actuation: A Feasibility Study," *2012 IEEE International Conference on Robotics and Automation*, pp. 1939-1945.

[24] D.C. Rucker, B.A. Jones, and R.J. Webster III, "A Geometrically Exact Model for Externally Loaded Concentric Tube Continuum Robots," *IEEE Trans Robotics*, 26(5):769-780, 2010.

[25] P.E. Dupont, J. Lock, B. Itkowitz, and E. Butler, "Design and control of concentric-tube robots," *IEEE Trans Robotics*, 26(2):209-225, 2010.

[26] S.D. Lhatoo, J.K. Solomon, A.W. McEvoy, N.D. Kitchen, S.D. Shorvon, and J.W. Sander, "A Prospective Study of the Requirement for and the Provision of Epilepsy Surgery in the United Kingdom," *Epilepsia*, 44(5):673-676, 2003.

[27] S.F. Berkovic, A.M. McIntosh, R.M. Kalnins, G.D. Jackson, G.C.A Fabinyi, G.A. Brazenor, P.F. Bladin, and J.L. Hopper, "Preoperative MRI Predicts Outcome of Temporal Lobectomy: An Actuarial Analysis," *J Neurol,* 45:1358-1363, 1995.

[28] D. Comber and E.J. Barth, "Precision Position Tracking of MR-Compatible Pneumatic Piston-Cylinder Using Sliding Mode Control," DSCC2011-5960, *Proc. 2011 Dynamic Systems & Control Conference and Bath/ASME Symp. Fluid Power & Motion Control*, Arlington, VA, pp. 45-51.

[29] D.B. Comber, D. Cardona, R.J. Webster III, and E.J. Barth, "Precision Pneumatic Robot for MRI-Guided Neurosurgery," *J Medical Devices*, **6**, March, pp. 017587-1, 2012.

[30] D.C. Rucker and R.J. Webster III, "Computing Jacobians and Compliance Matrices for Externally Loaded Continuum Robots," *2011 IEEE International Conference on Robotics and Automation*, Shanghai, China, pp. 945–950.

Addendum to Manuscript 1: Open-Loop Tip Accuracy of an MRI-Compatible Active Cannula
Robot

David B. Comber, Robert J. Webster III, Joseph S. Neimat and Eric J. Barth

From: *Hamlyn Symposium on Medical Robotics*, June 22-25, 2013

A-I. Introduction

Magnetic resonance imaging (MRI) is increasingly used intraoperatively, because it provides excellent soft tissue distinction and on-the-fly adjustment to imaging slice orientation without exposing clinician or patient to radiation. For neurosurgical procedures, intraoperative MRI holds significant advantages over traditional stereotactic methods (e.g. compensation for brain shift), and has thereby led to much research toward minimally-invasive treatments of brain tumors, epilepsy, and other neurological disorders. Because the tight confines of MRI scanners limit clinician access to the patient, an MRI-compatible robot is potentially useful for many procedures and additionally offers the clinician increased accuracy and degrees of freedom within the minimally-invasive context.

Affecting 0.5 to 1.0% of the global population, epilepsy is a neurological disorder for which surgery has been reported superior to prolonged pharmacotherapy, yet only a small fraction of potential surgical candidates receive treatment [1]. Minimally-invasive alternatives to conventional resection of seizure foci could side-step the potential morbidity and lengthy recovery associated with open brain surgery thereby making surgical treatment and cure available to a greater number of patients with less risk. Interstitial laser ablation of seizure foci has been clinically demonstrated using MRI to guide ablator placement and MR thermometry for thermal dosimetry [2]. This procedure currently requires multiple patient transfers between MRI scanner and operating room meaning that introducing an MRI-compatible robot could streamline surgical workflow. An alternative real-time MRI approach is high intensity focused ultrasound (HIFU), yet intracranial targets can be difficult to effectively treat due to high reflection and absorption of the ultrasound energy by the skull [3].

This paper reports a pneumatically-actuated active cannula robot designed for MRI-guided ablation of epileptogenic foci. An active cannula is a continuum robot consisting of concentric, superelastic nitinol tubes with pre-curved sections. Complex trajectories are realized by translation and rotation of the cannula tubes with respect to one another.

A-II. Materials and Methods

Since hippocampal sclerosis is present in a majority of epilepsy cases, the hippocampus was selected as the target region for thermal ablation, and an occipital trajectory was deemed optimal

for maximizing coverage through a single needle insertion. Following this trajectory and performing the ablation can be accomplished with five degrees of freedom: two translations and one rotation for the active cannula, and one additional translation and rotation for the ablator. Inclusion of rotation for the ablator provides the option of using an acoustic ablator with radially sectored transducers to direct the ablative energy [4].

To manipulate the active cannula and ablator, a robotic platform was designed and built, as shown in Fig. 2.11. For actuators, pneumatic piston-cylinders with fail-safe rod locks were selected instead of piezoelectric motors, as standard piezoelectric motor drives degrade image quality unless powered down during imaging [5]. Furthermore, pneumatic actuators are quieter than piezoelectrics, pose fewer contamination risks than hydraulics, and can run off a hospital's instrument air facilities. A detailed mechanical design of the robot is reported in [6].

A nonlinear, model-based controller was developed for precision position tracking of the actuators [6]. The electronics dedicated to controlling one actuator are: one 5-port/4-way proportional spool valve, two pressure transducers, one optical encoder for position feedback, and one 5-port/2-way valve for rod lock control. Long pneumatic tubing and shielded cables connect the actuators and optical encoders on the robot to the remotely located valves, pressure transducers and system electronics. The controller was implemented in MATLAB Simulink with xPC target. A supply pressure of approximately 585 kPa gage was used, providing actuator forces on the order of 40 N.
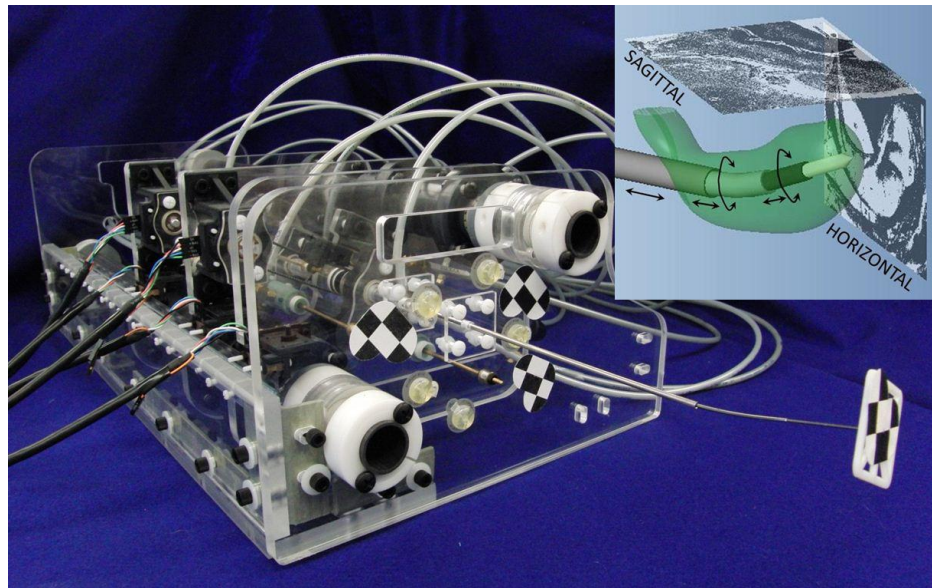
Figure 2.11 – Photograph of active cannula robot. Inset shows CAD model of cannula and ablator inside hippocampus.

Three tubes were selected for the active cannula and a simulated ablator. Their dimensions are presented in Table 2.3. The active cannula consists of a stiff, straight outer tube and inner, pre-curved nitinol tube. The outer tube only translates and inner tube both translates and rotates, as

shown in Fig. 2.11 inset. The inner tube was first curved by hand, and the resulting radius of curvature was estimated using a digital image of the tube.

Table 2.3 – Dimensions of active cannula and simulated ablator tubes.

Tube 1 outer diameter	3.18 mm
Tube 1 inner diameter	2.36 mm
Tube 2 outer diameter	1.65 mm
Tube 2 inner diameter	1.35 mm
Tube 2 radius of curvature	132.2 mm
Tube 2 arc length of curved portion	52.0 mm
Simulated ablator outer diameter	1.18 mm

The simulated ablator is a superelastic nitinol tube of outer diameter 1.18 mm. This is slightly smaller than existing MRI-compatible laser ablators [2], but the rotational mechanism of the robot readily accepts larger tube diameters using an interchangeable collet design.

Prior to in-scanner experiments, an initial benchtop assessment of cannula tip accuracy was needed. Thus, tip position measurements were acquired for 28 robot poses using an optical tracking system, the Micron-Tracker 3 by Claron Technologies (XB3-BW-H3-60). Three optical markers were affixed to the robot front plate. Manufactured from acrylic using a laser cutter, the plate includes pin-sized holes to assist in placing the markers at precisely known positions. Five multi-modality fiducial markers were similarly added for registration with MRI images. An optical marker was fixed to the cannula tip for bench testing with the optical tracker; it will be removed for in-scanner experiments.

Image registration from optical tracker to robot was achieved using point-based registration of the markers on the robot's front plate. Then, for each robot pose, the expected cannula tip position was determined from the robot's forward kinematics. The resulting model-based poses of the robot are illustrated in Fig. 2.12. Tip error was taken as the difference between measured tip position and tip position expected from the cannula model.

A-III. Results

The mean and maximum tip errors for the 28 cannula poses were 1.18 mm and 2.40 mm, respectively. The fiducial registration error was 0.278 mm, and steady-state errors of the base joints were on the order of 0.050 mm (translations) and 0.5 degrees (rotations).

A-IV. Discussion

Observing that the registration error and base joint tracking errors are 1 to 2 orders of magnitude below the cannula tip errors, it is reasonable to assume the majority of tip error is due to other sources. One likely cause is inaccuracy in the initial mounting of the cannula tubes; this
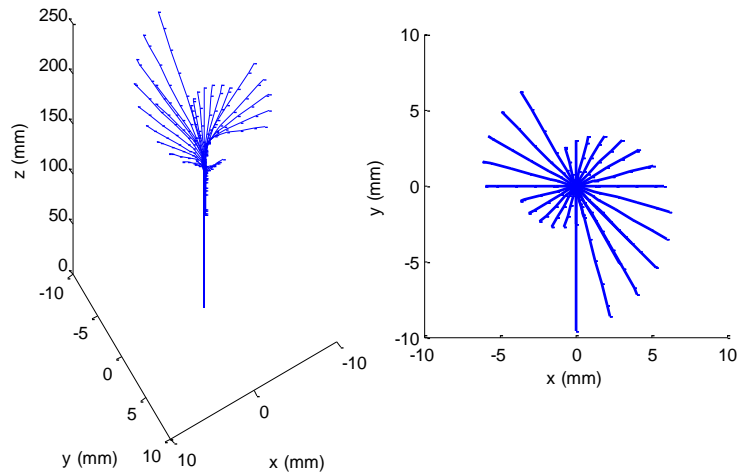
Figure 2.12 – Model-based poses of the active cannula robot: 3D view (left) and view along the needle guide axis (right).

was done by hand using a ruler and pen. Maximum tip error occurred when the precurved tube was at maximum extension. This error likely arose from the fact that the curvature preset into the curved tube may not have been perfectly circular. The shape setting could be improved by use of a high-precision jig and oven to more precisely set the circular curve.

Nonetheless, the presently observed tip errors are quite small and approach the minimum voxel size for MRI scanners ($1x1x1$ mm^3), and importantly we also note that real-time imaging will be available so that an image-based control loop can be closed on tip position during cannula insertion. Thus, the overall accuracy of tip placement is not limited to the robot's free-space open loop tip accuracy, which is what is reported in this paper. Furthermore, we tested for MRI-compatibility in a Philips 3T Achieva scanner, and the robot displayed no measurable effect on the signal-to-noise ratio of an fBIRN phantom. Image distortion tests with an ADNI phantom indicate a maximum distortion of 1.3 mm.

These results demonstrate that MRI-guided pneumatic actuation is a promising solution for the minimally-invasive treatment of epilepsy and of other intracranial diseases that either require or can benefit from MR imaging and thermometry. Future work includes integration of the robotic platform with the MRI scanner. Scanner experiments will focus on providing real-time feedback of tip location as well as using MR thermometry for real-time thermal dosimetry.

References

[1] J. Engel Jr. et al., "Practice Parameter: Temporal Lobe and Localized Neocortical Resections for Epilepsy," *Epilepsia*, 44(6):741-751, 2003.

[2] D.J. Curry et al., "MR-Guided Stereotactic Ablation of Epileptogenic Foci in Children," *Epilepsy and Behavior*, 24(4):408-414, 2012.

[3] A. Basak et al., "Implantable Ultrasonic Dual Functional Assembly for Detection and Treatment of Anomalous Growth," *2012 IEEE Int Conf EMBS*, San Diego, 170-173.

[4] A.M. Kinsey et al., "Transurethal ultrasound applicators with dynamic multi-sector control for prostate therapy: In vivo evaluation under MR guidance," *J Med Phys*, 35(5):2081-2093, 2008.

[5] H. Su et al., "High-field MRI-Compatible Needle Placement Robots for Prostate Interventions: Pneumatic and Piezoelectric Approaches," *Advances in Robotics and Virtual Reality*, T Gulrez & A Hassanien, eds, Springer-Verlag, Chap 1, 2011.

[6] D.B. Comber et al., "Sliding Mode Control of an MRI-Compatible Pneumatically Actuated Robot," *2012 Bath/ASME Symp Fluid Power & Motion Control*, D.N. Johnston and A.R. Plummer, eds, Centre for Power Transmission & Motion Control, University of Bath, UK, 283-293.

Chapter 3 – Design and Control of an MR-Compatible Additively Manufactured Needle Steering Robot

David B. Comber[1], Jonathon E. Slightam[3], Vito R. Gervasi[4], Joseph S. Neimat[2], and Eric J. Barth[1]

Vanderbilt University (1) Dept. Mechanical Engineering and (2) Medical Center, Nashville, TN, (3) Marquette University, Milwaukee, WI, and (4) Milwaukee School of Engineering

Shared first-authorship for D. B. Comber and J. E. Slightam

Prologue

This chapter describes the mechanical hardware and low-level controls resulting from a second iteration of designing an actuation unit for an MRI-guided concentric tube robot. New constraints included inherently safe mechanisms and an overall device footprint compatible with the transforamenal ablation concept. After manuscript submission, a controller configuration was conceived for higher precision and speed. The newer controller is presented in the chapter's addendum.

Abstract

Fluid power actuators (hydraulic and pneumatic) are well suited for electromagnetically sensitive environments like magnetic resonance imaging (MRI) machines. Such actuators would enable intraoperative MRI guidance of robotically steerable needles. Yet, a technical barrier to using fluid power in MRI-guided surgical systems is the absence of commercial, off-the-shelf fluid power actuators that are sterilizable and inherently safe. This paper reports the design, modeling, and control of an additively manufactured pneumatic stepper actuator. Designed using corrugated diaphragm theory, one helix-shaped bellows and one toroid-shaped bellows provide pure rotation and pure translation, respectively. The entire actuator module functions as a two degree-of-freedom needle driver; that is, the two bellows directly translate and rotate the base of one tube of a steerable needle. Several of these modules can be cascaded together as a complete actuation unit for steerable needles comprising multiple, concentric tubes. For needle tip translations and rotations, mechanical stops limit the bellows' movements to maximum unplanned step sizes of 0.5 mm and 0.5 degrees, which are acceptably safe in the event of a systems failure. Additively manufactured by selective laser sintering of nylon powder, the prototype device is compact and

hermetically sealed for sterilizability. The linear bellows produced peak forces of 33 N and -26.5 N for needle insertion and retraction, respectively. The rotary bellows produced peak torques of ±68 mN·m. Sub-step control allows translations and rotations less than full step increments; steady-state errors of 0.013 mm and 0.018 degrees were achieved.

I. Introduction

Medical robotic systems for image-guided interventions require safe, sterilizable (or disposable), precision actuators. Imaging modalities like computed tomography (CT) and magnetic resonance imaging (MRI) impose further limitations on the design of such actuators. It is desirable for the robot and its actuators to be transparent to the imager and to not produce artifacts, noise or distortion in the images. Thus, actuator design is restricted to materials and principles of operation that are compatible with the imaging environment. Together with the requirements for safety, sterilizability and precision control, these restrictions present a challenging design problem.

Review of MR-Compatible Robots

Over the past 20 years, numerous custom MR-compatible actuators have been reported in the literature. Due to the high strength magnetic field of the MR imager, these actuators cannot contain ferromagnetic materials. Pneumatic actuation has been commonly employed because the working principle does not rely on electromagnetism. Thus, these actuators can be constructed solely from diamagnetic materials. Stoianovici et al. reported a pneumatic stepper motor, PneuStep, which consists of three pulsing diaphragms that rotate a harmonic gear drive [1]. Using several of these motors to actuate an MRI-guided robot, Muntener et al. demonstrated transperineal prostate brachytherapy in a canine model [2]. Similarly, using reciprocating piston-cylinders to drive a ratcheting stepper mechanism, Zemiti et al. developed a CT- and MR-compatible needle puncture robot for abdominal procedures [3]. Using both hydraulic and pneumatic piston-cylinders, van den Bosch et al. reported a momentum-based needle tapping device for prostate interventions [4].

Departing from the stepping mechanism approach, INNOMOTION, one of the few commercially available MRI-guided robotic systems, addressed the need for safety by custom designing pneumatic piston-cylinders to exhibit high dynamic and low static friction [5]. Tokuda et al. demonstrated a needle positioning device employing four pneumatic piston-cylinders, opting for manual needle insertion by the radiologist for safety [6].

Other forms of actuation, in particular piezoelectrics, have been employed in a variety of anatomy-specific MR-compatible robots, including several for neurosurgical procedures [7-9]. While piezoelectrics offer precise, safe, and non-backdrivable actuation, many researchers have reported the high voltage ultrasonic drivers to substantially reduce the signal-to-noise (SNR) ratio of the MR imager, precluding the ability to servo the robot motors while simultaneously acquiring images [8]. However, by using low-noise, non-harmonic piezoelectric motors as well as replacing

the commercial motor driver boards with custom, low-noise drivers, Su et al. achieved a low 2% loss in SNR with motors servoing at full speed [10]. For a more comprehensive review of MR-compatible robots, see [8] and [11].

Although piezoelectric actuators can be a viable solution for MR-compatible robots, a low-cost yet customizable actuator that does not require extreme care in the design and shielding of drive electronics is desirable. Furthermore, both pneumatic and piezoelectric robots for MRI-guided interventions as reported in the literature have been limited to linear needle trajectories.

Concentric Tube Steerable Needles

The objective of this new work is to deploy steerable needles in curved trajectories under MRI guidance using a compact, safe, and sterilizable actuation unit. The MR-compatible actuation unit reported here is designed to robotically control a concentric tube needle, a tentacle-like needle made of multiple, elastic (shape memory) tubes with pre-curved lengths at their tips. Controllable needle motion is realized as the tube bases are rotated and telescoped relative to one another [12-13]. The feasibility of using concentric tube needle robots has already been investigated for minimally invasive surgeries in open body cavities like the sinuses and lung [14-15]. For soft tissue applications requiring MRI guidance, concentric tube needles would be deployed in a follow-the-leader fashion to prevent tissue damage, as described in [16-17]. This would be particularly useful for neurosurgical interventions, because nonlinear needle paths enable avoidance of eloquent, untreated brain tissues, while MRI guidance enables excellent soft tissue visualization and MR thermal imaging (MRTI) enables thermal dosimetry for ablation therapies.

Flexible Fluidic Actuator Design and Control

Made of elastomeric diaphragms, bellows, or artificial muscles, flexible fluidic actuators (FFA's) are an MR-compatible actuation technology. Providing compact actuation with hydraulics or pneumatics as the working fluid, FFA's are inexpensive and their material compliance often eliminates the need for added spring elements. Early work in the design, modeling, and control of FFA's was established by Paynter and Wilson and Orgill in [18-20] and [21-23], respectively. Paynter defined models for twisting and translational bellows with changes in enthalpy and experimentally determined torque relationships. Wilson and Orgill developed a mechanics of materials approach for modeling and designing twisting and translating bellows. They and Paynter both demonstrated simple serial and parallel chain robots using bellows actuators, later to be classified as FFA's by Gaiser et al. [24]. Grzesiak et al. and Zientarski independently reported the use of additive manufacturing of polyamide FFA's by selective laser sintering (SLS) [25-26]. Grzesiak reported FFA design for additive manufacturing of the Festo Bionic Handling Assistant [26]. Furthermore, novel uses of additive manufacturing processes have been reported to fabricate robotic systems in a cost- effective simultaneous manner, whereby joints, structures, power

transmission, and actuators are integrated during the process of fabrication or as a monolithic structure [27-30]. Slightam and Gervasi demonstrated the technology readiness of using selective laser sintering to fabricate monolithic FFA-driven robots in a two level Gough-Stewart platform [36].

A broad range of medical devices have used FFA's. Proulx and Plante reported an MR-compatible needle positioning device employing binary actuation of 12 pneumatic muscles [32]. Ikuta et al. created a multi-degrees-of-freedom active catheter actuated by miniature saline bellows [33], which were additively manufactured by stereolithography [34]. Similarly, Haga et al. developed a hydraulic suction active catheter and guide wire for intravascular diagnosis and therapy [35]. Further review of fluidic-based medical devices can be found in [36].

While pneumatic FFA's meet the gold standard of MR-compatibility, in order to achieve precision control it is necessary to accurately model the highly nonlinear pressure and mass flow dynamics. Richer and Hurmuzlu introduced a nonlinear mathematical model for the gas dynamics and demonstrated substantial improvements in bandwidth and force capabilities using sliding mode control [37-38]. Zhu and Barth achieved sub-millimeter positioning accuracy of 0.05 mm steady-state error using a composite adaptive and sliding mode force controller for an industrial robot [39]. Comber et al. reported sliding mode control of pneumatic piston-cylinders on an MR-compatible concentric tube needle robot, with base joint errors of 0.032 mm and 0.45 degrees resulting in a mean open-loop needle tip error of 1.2 mm [40-41].

In contrast to piston-cylinders, FFA's offer a hermetically-sealed and thus sterilizable means of actuation favorable for clinical use. Piston-cylinders are also unfavorable for clinical use due to the risk of full stroke motion in the event of a hardware or software failure. This provides motivation to design, manufacture, and precisely control a fail-safe, multi-DOF module that incorporates the benefits of flexible fluidic actuation.

II. Mechanical Design

The mechanical design of an MR-compatible, inherently safe actuating device for concentric tube needles is presented in several parts: 1) identification of design requirements, 2) design to actuate needle translation, 3) design to actuate needle rotation, and 4) design to grasp the needle. Designs of a device housing and position sensor assembly are presented as well. The overall approach is to implement FFA design to impart fail-safe, stepper motion to the needle. For reference, a photograph of the resulting prototype is shown in Fig. 3.1.
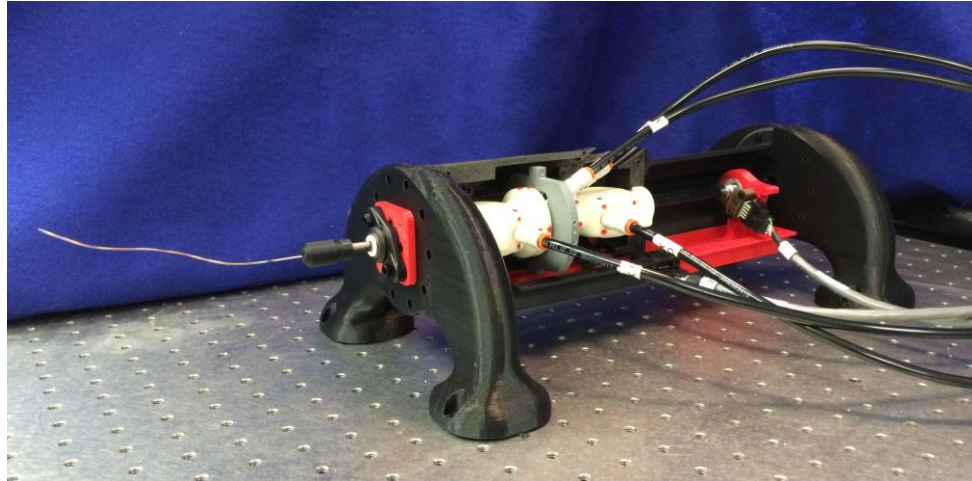
Figure 3.1 – Photograph of prototype with helix-shaped concentric tube needle. One half of the device housing is not shown, to expose inner working parts.

Design Requirements

Specifications were established such that the device would remain safe in the event of mechanical, pneumatic, electrical, or software control failure. Thorough discussions with our clinical collaborator concluded that unplanned needle tip displacements of 0.5 mm and 0.5 degrees were permissible in the event of a system failure. These values were thus selected as the maximum step sizes for linear and rotary actuation, in order to make the device inherently safe. Actuation forces and torques were determined using prior designs of concentric tube needles; the primary barrier to overcome is the friction that occurs as the inner and outer tubes rub against each other. The maximum operating pressure was limited to be no greater than that realistically supplied by existing instrument air facilities in hospitals. Optical position sensor resolution was chosen to be one order of magnitude greater than the required precision of the robot base joints. Table 3.1 summarizes these design parameters.

Table 3.1 – Device Specifications

Parameter	Specification
Translation step size	0.5 mm
Rotation step size	0.5 degrees
Translation force	22 N
Rotation torque	100 mN·m
Transmission tube diameter	6.35 mm
Operating pressure (gage)	700 kPa
Position sensor resolution	0.015 mm; 0.020 degrees

Ultimately the device needed to provide three principal functions to effectively advance the needle in a sequenced stepping motion: incremental linear displacement, incremental angular displacement, and gripper mechanisms to grasp and release the needle in a non-backdrivable manner. The stepping motion is then accomplished by sequencing control valves located outside the MRI scanner room and connected to the device by long transmission lines. Additionally, a versatile, modular design was desirable such that the device could be used for a variety of clinical target applications. Thus, device specifications included adjustability of step size increments as well as the flexibility to interchange tubes across a range of needle diameters.

Needle Translation

The conceptual design of the actuating mechanism for translation is illustrated in Fig. 3.2. The linear FFA is made of an inner bellows and outer bellows, connected at their two ends by a thick-wall rigid ring. The resulting hollow center allows for the needle to pass directly through the axial center of the device, achieving a compact design with uniform loading. This design is similar to that of our prior work, but one key difference is that inner bellows clearance was substantially increased [42]. This allows a thick-wall, large diameter tube to run the entire length of the device from back to front. Outside the front housing of the robot module (see Fig. 3.1), this transmission tube steps down to the millimeter-scale needle. Using a collet and clamping nut assembly, the needle can be interchanged for other sizes and shapes of sterilized needle tube. The transmission tube design increases torsional rigidity and reduces the length of expensive nitinol used for the actual needle.
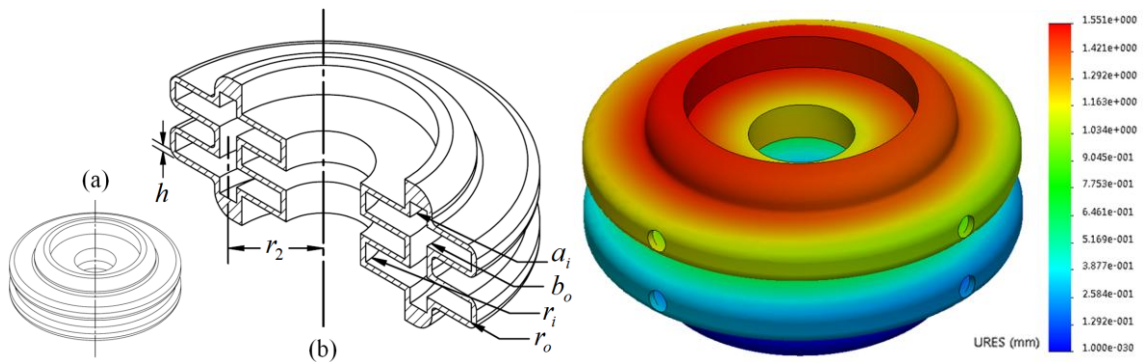
Figure 3.2 – Diagrams of (a) linear FFA, (b) annotated cutaway view, and (c) typical FEA case result.

Detailed design for the linear FFA began using the analytical model of a flat diaphragm with rigid center as described in [43]. This model is valid for small deflections of magnitudes less than five times the diaphragm thickness. It also assumes linearity between diaphragm displacement and internal pressure, because the rigid center substantially linearizes the diaphragm behavior.
The linear FFA shown in Figure 3.2 has some key geometrical differences from a simple flat diaphragm with rigid center. It has a hollow center of radius r_i, and inner and outer annular-area

diaphragms connected at a radius r_2. Thus, the analytical model in [43] was only used as a general guide. It was assumed that the inner and outer annular-area diaphragms each behave as some equivalent flat diaphragm with rigid center. This assumption was made because the rigid region of a rigid-center diaphragm deflects uniformly, and due to geometric constraint, the inner and outer diaphragms also deflect equally.

After a first pass at the detailed design was made using the model in [43], the part was drafted in CAD. Then, finite element analysis (FEA) was used to verify the expected displacement of the bellows due to internal pressure loading. The results for one typical FEA case are shown in Fig. 3.2(c). FEA also revealed a substantial stress concentration in the original design; imbalance between the surface areas of the inner and outer annular diaphragms was determined to be the cause. The location of the corrugation connection r_2 was adjusted to reduce this stress concentration.

Accounting for the number of corrugations n that make up the entire bellows, the total displacement y_b of the linear FFA is given as:

$$y_b = 2ny_0 \tag{1}$$

where y_0 is the deflection of just one of the diaphragms. The bellows stiffness k_b is then defined by (2), which is a simple force balance equation at equilibrium, where the product of internal pressure and effective acting area is equal to the product of bellows stiffness and displacement. This is Hooke's Law and assumes linear elasticity.

$$k_b = \frac{PA_e}{y_b} \tag{2}$$

The linear FFA was designed for gage pressures from zero to 550 kPa (80 psi) to correspond to deflections from zero to 6 mm, with a linear behavior. While this translation is much greater than the maximum allotted step size, the maximum step size can be adjusted via mechanical stops. Furthermore, this linear deflection range allows for substantial pre-tensioning of the bellows. Pre-tensioning makes the bellows stiffness useful as a restoring force, such that bi-directional actuation is achieved with only one bellows, much like a single-acting piston-cylinder with spring return. The design of a constraining system with adjustable mechanical stops and pre-tension is later described in detail. The final design parameters of the linear FFA are listed in Table 3.2 and meet the specification requirements.

Table 3.2 – Translational FFA Design Parameter Values.

Parameter	Value, mm (in)	Parameter	Value
r_i	6.35 (0.250)	n	2
r_o	22.225 (0.875)	Young's modulus, E	1586 kPa (230 ksi)
r_2	14.2875 (0.5625)	Poisson's ratio, v	0.408
a_i	13.0175 (0.5125)	k_b	120 N/mm (685 lbf/in)
b_o	15.5575 (0.6125)	A_e	1310.965 mm^2 (2.032 in^2)
h	0.762 (0.030)		

Needle Rotation

FFA's allow for manipulation of the corrugation geometry to achieve the desired motions in not only translation, but also rotation. The theory of thin orthotropic shells with helical corrugations was well defined by Wilson and Orgill [21-22]. They reported a mechanics of materials approach for the design of helical corrugations on a pressurized thin-walled tube to achieve rotational motion for flexible robotic applications.

The rotation of the free end of such a tube can be modeled by examining the cross section orthogonal to the central axis of the helices (Fig. 3.3(b)). This representation is illustrated in Figure 3 along with the final computer-aided design (CAD) of the rotary FFA. For a given cross section orthogonal to the 1-axis, the shear displacement δ_s due to pressurization will occur along the 2-axis direction and can be calculated from the rectangular model shown in Fig. 3.3(c), which resembles the representation reported in [44].
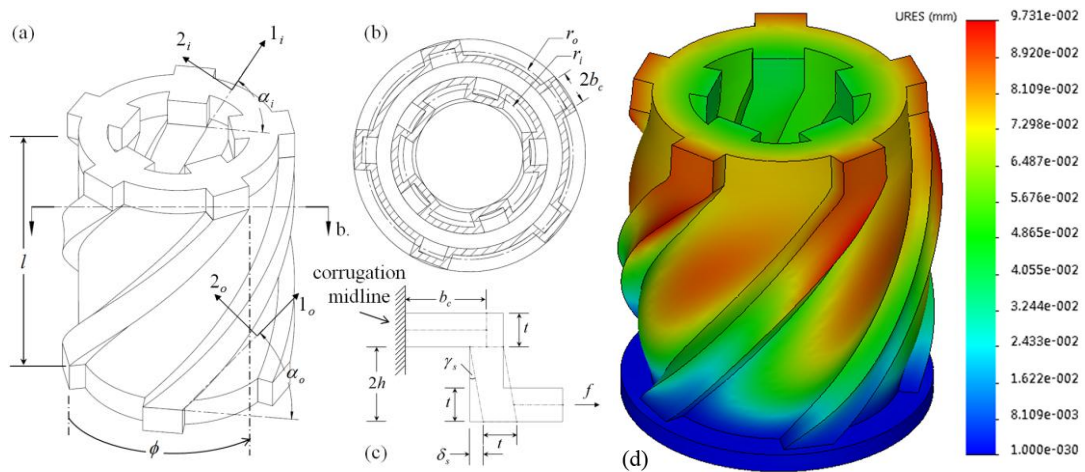
Figure 3.3 – Diagrams of (a) rotary FFA, (b) cross section orthogonal to central axis, (c) half corrugation shear deflection, and (d) typical FEA case result.

To design a rotary FFA with helical corrugations, an analytical expression is needed for the cumulative angular displacement θ of the free end of the FFA with respect to the central axis. The rotary FFA geometry as designed in Fig. 3.3 is unique in that it includes inner helical corrugations at a radius r_i. The response of these corrugations to applied pressure is different and is equivalent to pulling a vacuum on the conventional outer corrugations. That is, when pressurized the inner helix "winds up" instead of unwinding. Thus, the inner helix must be given the handedness opposing that of the outer corrugations, in order for angular displacement of the inner corrugations to be in the same direction of rotation as the outer corrugations. The derivation that follows applies to both the outer and inner corrugations, but a minus sign must be included for the inner corrugations. With the inclusion of inner helical corrugations, the overall rotary FFA geometry results in a hollow center that can then be concentric with the axis of the steerable needle and transmission tube.

Referring to Fig 3.3(c), the shear strain γ_s of the block of dimensions t by $2h$ is $\gamma_s = f/(tG)$, where f is applied force F per arc length S, t is wall thickness, and G is the shear modulus: $G = \frac{1}{2}E/(1+\nu)$. With internal pressurization, the applied force F_o or F_i acting on one outer or inner corrugation, respectively, is the product of pressure P and total surface area, as given in (3).

$$F_o = 2h_oS_oP \quad \text{and} \quad F_i = 2h_iS_iP \tag{3}$$

The arc lengths S_o and S_i of the helices are given in (4), where r_o is the outer corrugation radius and r_i the inner corrugation radius (see Fig 3.3(b)). The outer and inner helix pitches are the same and denoted as p, and the length l of the bellows is $l = p\phi$, where ϕ is the angular displacement for traveling some longitudinal length l along a helix of pitch p.

$$S_o = \phi\sqrt{r_o^2 + p^2} \quad \text{and} \quad S_i = \phi\sqrt{r_i^2 + p^2} \tag{4}$$

By the small angle approximation $\gamma_s \approx \tan\gamma_s = \delta_s/(2h)$, δ_s is then given in (5) as the product of corrugation height $2h$ and the shear strain of the block in Fig. 3.3(c). Shear displacement is denoted as $\delta_{s,o}$ for the outer tube and $\delta_{s,i}$ for the inner tube.

$$\delta_s = 2h\gamma_s = 2h\frac{f}{tG} \tag{5}$$

To calculate the cumulative angular displacements θ_o and θ_i about the central axis as resulting from $\delta_{s,o}$ and $\delta_{s,i}$, respectively, an expression is needed for the pure shear strains $\gamma_{\theta,o}$ and $\gamma_{\theta,i}$ relative

to the central axis. This expression is obtained by projecting δ_s from the plane orthogonal to the 1-axis onto the plane of Figure 3b orthogonal to the central axis. The pure shear strain in units of radians is then obtained by dividing by the radius r_s that is tangent to the vector f in Figure 3c, where $r_{s,o} = r_o - h_o$ and $r_{s,i} = r_i + h_i$. The resulting expressions for pure shear strain are given in (6).

$$\gamma_{\theta,o} = \delta_{s,o}(\sin\alpha_o)/r_{s,o} \quad \text{and} \quad \gamma_{\theta,i} = -\delta_{s,i}(\sin\alpha_i)/r_{s,i} \tag{6}$$

Note that a minus sign has been included for the shear strain on the inner corrugations because applied pressure causes the inner helix to wind up, in contrast to unwinding like the outer helix. Table 3.3 summarizes the four possible corrugation configurations and the corresponding directions of rotation.

Finally, the cumulative angular displacements due to pressure applied to the outer and inner helical corrugations are given in (7). A factor of $2n$ is included to account for the total number of half-helical corrugations that each undergo the angular strain γ_θ in a series configuration.

$$\theta_o = 2n\frac{l}{r_{s,o}}\gamma_{\theta,o} \quad \text{and} \quad \theta_i = 2n\frac{l}{r_{s,i}}\gamma_{\theta,i} \tag{7}$$

Table 3.3 – Helical Corrugation Configurations and Resulting Rotations.

Helix Direction	Outer or Inner Helix	Rotation Direction
Clockwise	Outer	Counterclockwise
Clockwise	Inner	Clockwise
Counterclockwise	Outer	Clockwise
Counterclockwise	Inner	Counterclockwise

Due to the "winding up" behavior of the inner helical corrugations, a unique characteristic of this rotary FFA design is that the cumulative linear displacement (i.e. along the central longitudinal axis) is quite small. Thus, an FFA exhibiting nearly pure rotation can be realized with this innovative design geometry. As a result of the opposing longitudinal loadings with applied pressure on the inner and outer thin shells, the net longitudinal deflection of the rotary FFA is approximately zero. The cancelation of deflections of the inner and outer helical corrugations is later verified experimentally. Any small amount of net longitudinal deflection that might occur can be eliminated with freely rotating, longitudinal constraints on the free-moving end of the rotary FFA. The final design dimensions for the rotary FFA are specified in Table 3.4.

Table 3.4 – Rotational FFA Design Parameter Values.

Parameter	Value, mm (in)	Parameter	Value
$2h_o$	1.59 (0.0625)	$A_{e,\theta}$	1099 mm^2
$2h_i$	1.97 (0.0775)	r_o	11.53 mm
t	0.76 (0.0300)	α_o	49.6 degrees
S_o	33.36 (1.313)	α_i	61.6 degrees
S_i	28.89 (1.137)	k_θ	150 kPa/degree
r_i	7.33 (0.2888)	n	5
$b_{c,o}$	1.39 (0.0548)	$b_{c,i}$	1.57 mm

Needle Grasping

Gripper mechanisms were designed to grasp and release the transmission tube that carries the needle in a non-backdrivable manner. Non-backdrivability is achieved by engaging at least one of the two grippers at all times. Each gripper consists of two diaphragms located on opposing sides of the transmission tube. When inflated, the diaphragms clamp the tube by deflecting toward and making contact with the tube. This design was tested and worked well for imparting actuation from the linear FFA. However, this design was ineffective at imparting actuation from the rotary FFA because the tube slipped in rotation at its line of contact with the gripper diaphragms. This problem was solved by inserting a clamshell-like plastic clamp between the diaphragms and the transmission tube (see Fig. 3.4). This insert effectively increased the gripping contact surface area and thereby eliminated the unwanted slipping.

Device Housing and Constraints

To achieve inherently-safe operation for the robot module, linear and rotary safety brackets with mechanical stops were designed. The safety brackets include set screws to adjust the pre-tension on the linear and rotary FFA's and to adjust the step increment sizes. The brackets were also needed to constrain the linear and rotary FFA motions to pure translation and rotation, respectively, such that the two degrees of freedom remained independent of each other. To accomplish this, rigid constraint tabs were added on both ends of the FFA device, and these tabs interface with linear and rotary safety brackets. As illustrated in Fig. 3.4, the 2-DOF FFA includes linear and rotary actuating bellows, two transmission tube grippers, and mechanical constraint tabs.
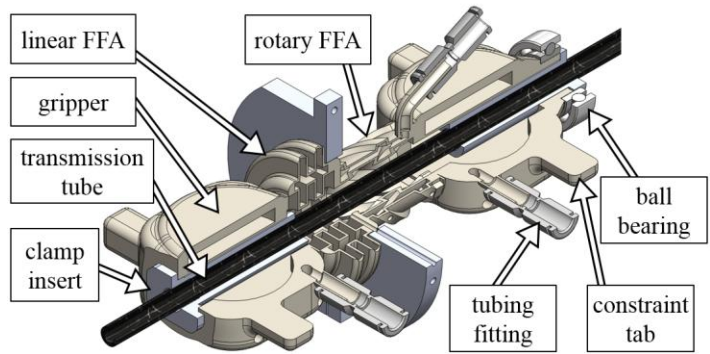
Figure 3.4 – 2-DOF FFA with mechanical constraint tabs.

The constraint tabs are fitted to slots in linear and rotary safety brackets, as depicted in Fig. 3.5. These brackets are a portion of a larger housing which supports the entire 2-DOF FFA and position sensing mechanism. The constraint brackets and mating tabs allow for simultaneous pressurization of the linear and rotary FFA's. Thus, the step size and pre-tension can be set according to the desired conditions of device operation. This ability to tune the set points for unique procedures, such that step size increments are inherently safe, makes the design robust in its potential for medical applications.
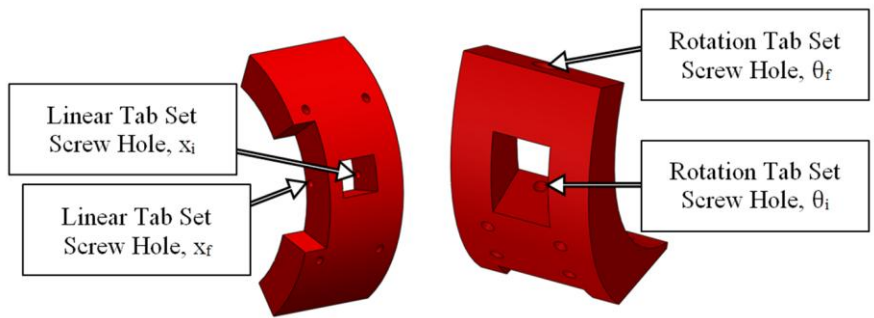
Figure 3.5 – Linear and rotary safety brackets constrain the rigid tabs and provide adjustments to preloads and step increment sizes.

For the linear bellows, the maximum pre-tension length is 1.5 mm and the maximum step increment is 3.5 mm. For the rotary bellows, the maximum pre-tension angle is 0.5 degrees and the maximum step increment is 1.5 degrees. The constraint tabs are sufficiently stiff to handle up to 267 N (60 lbf) of force and 45 N·m (400 lbf·in) of torque applied on the end of the tabs. The tabs could thus handle an unexpected load greater than magnitudes typical of concentric tube robots.

Mechanism for Absolute Position Sensing

An assembly was designed to provide the absolute linear and rotary displacement of the transmission tube, as shown in Fig. 3.6. High-resolution, indexed optical encoders were selected to ensure precision feedback and MRI-compatibility. The rotary encoder module (U.S. Digital part

no. EM2-1-5000-I) is affixed to the rotary encoder mount. This custom part translates with but does not rotate with the transmission tube, because it interfaces with the transmission tube via a ball bearing. A transparent code disc (5000 counts per revolution) mounts to and rotates with the transmission tube. The linear encoder module (U.S. Digital part no. EM1-0-500-I) is affixed to the device housing, while a transparent code strip (500 lines per inch) mounts to the rotary encoder mount and thereby translates with the transmission tube. Two linear guides support the rotary encoder mount and code strip and constrain against angular displacements. For good noise rejection during MRI scanner experiments, a cable driver chip is mounted to each encoder module to convert the signals from single-ended to differential (U.S. Digital part no. PC4-H10).
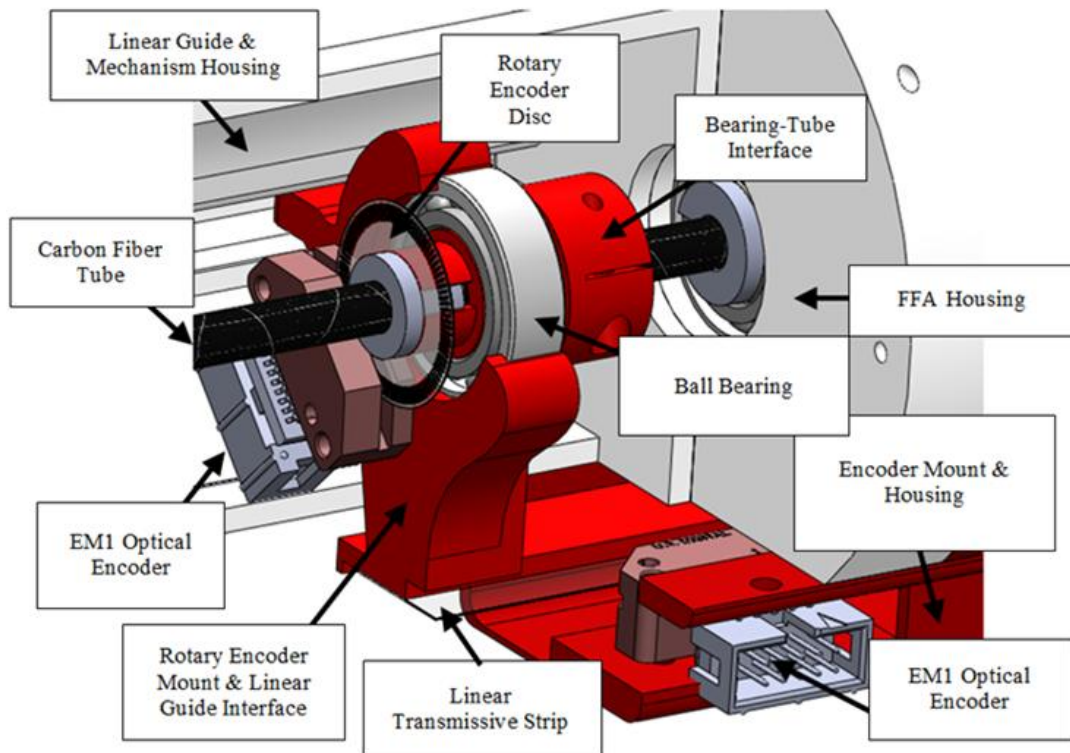
Figure 3.6 – Absolute position sensing mechanism.

III. Controller Design

A novel concept for hybrid control was conceived to meet both the performance criteria for precision positioning and decent speeds for translation and rotation. By sequencing a total of four control valves, the FFA bi-directionally translates and rotates the transmission tube. Two on/off solenoid valves engage and disengage each respectively one of the two grippers. Two proportional spool valves each respectively control the linear FFA and rotary FFA. Two separate hybrid controllers were designed for translation and rotation control respectively. Each controller has two modes: full step control and sub-step control.

Full Step Control Mode

In full step control mode of the linear FFA, the valves are sequenced to advance the transmission tube toward the final desired position. Using three control valves, the following sequence is repeated to advance the tube in the positive direction: (1) Inflate linear gripper, (2) Exhaust rotary gripper, (3) Inflate linear FFA, (4) Inflate rotary gripper, (5) Exhaust linear gripper, and (6) Exhaust linear FFA. To retract the tube in the negative linear direction, the material stiffness of the linear FFA is used to impart a restoring force. The following sequence is repeated to achieve negative linear displacement: (1) Inflate linear FFA, (2) Inflate linear gripper, (3) Exhaust rotary gripper, (4) Exhaust linear FFA, (5) Inflate rotary gripper, and (6) Exhaust linear gripper. The rotary FFA is not active during these two sequences.

In full step control mode of the rotary FFA, the following sequence is repeated to rotate the tube in the positive direction (right-handed) toward the final desired angular displacement: (1) Inflate rotary gripper, (2) Exhaust linear gripper, (3) Inflate rotary FFA, (4) Inflate linear gripper, (5) Exhaust rotary gripper, and (6) Exhaust rotary FFA. The tube is rotated in the negative direction (left-handed) using the internal stiffness of the rotary FFA to impart a restoring torque. The following sequence is repeated to achieve negative angular displacement: (1) Inflate rotary FFA, (2) Inflate rotary gripper, (3) Exhaust linear gripper, (4) Exhaust rotary FFA, (5) Inflate linear gripper, and (6) Exhaust rotary gripper. The linear FFA is not active during these two sequences.

These valve sequences ensure that at least one gripper is engaging the transmission tube (and needle) at all times, for safety.

Sub-Step Control Mode

<u>Linear FFA Sub-Step Control Law</u>

When the tube displacement is within one step increment of the desired final displacement y_{ref}, the controller switches modes from full step control to sub-step control. For linear displacement in sub-step control mode, the linear gripper engages the transmission tube and a model-based, sliding mode controller commands mass flow to the linear FFA using its respective control valve (proportional spool type). The control law formulation has been thoroughly described in our prior work [40, 42]. A brief summary is provided here. The equation of motion for the linear FFA and the final control law to command an orifice area A_v to the spool valve are described by (8) to (14).

$$M\ddot{y} = (P - P_{atm})A_e - k_b y - \xi\dot{y} - F_D \tag{8}$$

$$A_v = k_p \frac{\dddot{y}_{ref} - \hat{f}(\cdot) - 3\lambda\ddot{e} - 3\lambda^2\dot{e} - \lambda^3 e - \eta\,\mathrm{sat}(s/\phi)}{g(\cdot)} \tag{9}$$

$$\ddot{y} = \hat{f}(\cdot) + g(\cdot)A_v = -\frac{1}{M}\left(\frac{PA_e^2}{V} + k_b\right)\dot{y} + \frac{1}{M}\frac{RT}{V}\Psi(P_u, P_d)A_v \qquad (10)$$

$$\Psi(P_u, P_d) = \begin{cases} C_1 C_f P_u / \sqrt{T} & , \quad \dfrac{P_d}{P_u} \leq C_r \\[3mm] \dfrac{C_2 C_f P_u}{\sqrt{T}}\left(\dfrac{P_d}{P_u}\right)^{1/\gamma}\sqrt{1 - \left(\dfrac{P_d}{P_u}\right)^{(\gamma-1)/\gamma}} & , \quad \dfrac{P_d}{P_u} > C_r \end{cases} \qquad (11)$$

$$\Psi(P_u, P_d) = \begin{cases} \Psi(P_{\text{supply}}, P) & , \quad A_v \geq 0 \\ \Psi(P, P_{\text{atm}}) & , \quad A_v < 0 \end{cases} \qquad (12)$$

$$s = \left(\frac{d}{dt} + \lambda\right)^3 \int e \qquad (13)$$

$$\text{sat}(s/\phi) = \begin{cases} \text{sgn}(s/\phi) & , \quad |s/\phi| \geq 1 \\ s/\phi & , \quad -\phi < s < \phi \end{cases} \qquad (14)$$

In (8), ξ is the bellows' hysteretic damping and F_D represents all the unknown disturbance forces like friction. The control volume V is defined as $V = V_{dead} + A_e y$, where the dead volume is V_{dead}; isothermal behavior is assumed. Model-based sliding mode control is a good choice for precision pneumatic applications because it robustly handles the highly nonlinear dynamics and the unknown friction forces. For this reason, the friction forces and hysteretic damping have been omitted from the control law. The error e is taken as the difference of measured position and reference position, $e = y - y_{ref}$. The functions $\hat{f}$ and g are defined by the companion, or controllability canonical, form of the system dynamics, as given by (10). The mass flow through the proportional valves is given in (11) as normalized by orifice area A_v (that is, $\dot{m} = \Psi A_v$) and assumes isentropic flow through a hole in an infinitesimally-thin plate. The pressures upstream and downstream of the valve, P_u and P_d, are defined by (12). Isothermal behavior is assumed for the pressure dynamics of the control volume: $\dot{P} = (RT\dot{m} - P\dot{V})/V$. The sliding surface s and saturation function are defined by (13) and (14), respectively. A summary of the controller parameter definitions and values for the linear FFA is given in Table 3.5.

Table 3.5 – Linear FFA Sub-Step Control Law Parameters.

Parameter	Value	Parameter	Value
Gas constant, air, R	288.3 J/kg/K	Temperature, T	294 K
Robustness constant, η	200 mm/s^3	Closed-loop poles location, $-\lambda$	-120 Hz
Hysteretic damping, ξ	12.5 kPa/(mm/s)	Proportional gain, k_p	0.3
Critical pressure ratio, air, C_r	0.5286	Valve discharge coefficient, C_f	0.2939
Effective area, A_e	1419 mm^2	Moving mass, M	82 g
C_1 for air	0.04031 s$\cdot$K$^{0.5}$/m	C_2 for air	0.1560 s$\cdot$K$^{0.5}$/m
Boundary layer, ϕ	1 mm/s^2	Stiffness, k_b	143 kPa/mm

Rotary FFA Sub-Step Control Law

Similarly, a model-based sliding mode control law was derived for sub-step control with the rotary FFA. The hybrid controller for tube angular displacement switches to sub-step mode when tube angular displacement is within one step increment of the desired final angular position θ_{ref}. In the equation of motion (15), internal pressurization of the rotary FFA produces torques τ_o and τ_i on the outer and inner corrugations, as given in (16), and τ_D represents all the unknown disturbance torques like friction. The stiffness and hysteretic damping behaviors are modeled as a torsional spring and damper each acting on some effective area $A_{e,\theta}$ at some effective radius of distance r away from the central axis of the helix. Using the expressions for applied force given in (3), an expression for the quantity $rA_{e,\theta}$ is given in (17), where the relation $p = r_o \tan\alpha_o = r_i \tan\alpha_i$ is used to simplify.

$$J\ddot{\theta} = \tau_o + \tau_i - rA_{e,\theta}k_\theta\theta - rA_{e,\theta}\xi_\theta\dot{\theta} - \tau_D \tag{15}$$

$$\tau_o = 2nr_oF_o \sin\alpha_o \quad \text{and} \quad \tau_i = 2nr_iF_i \sin\alpha_i \tag{16}$$

$$\begin{aligned} rA_{e,\theta} &= 2n(2h_oS_or_o \sin\alpha_o + 2h_iS_ir_i \sin\alpha_i) \\ &= 4np(h_oS_o \cos\alpha_o + h_iS_i \cos\alpha_i) \end{aligned} \tag{17}$$

Using (16) and (17), the equation of motion (15) can be re-written as (18). The final control law is given by (11)-(14) and (19)-(21). For the sake of simple notation, note that the variables in (15)-(21) are distinct from those of the linear FFA controller in (8)-(10). Definitions and values for new

parameters that are different from those in the linear FFA control law are summarized in Table 3.6. The error is defined as $e = \theta - \theta_{ref}$, and friction and hysteretic damping have been neglected. The control volume is defined as $V = V_{dead} + \Delta V$, where the change in volume ΔV is given in (21); the displacement θ is obtained by rearranging (6)-(7).

$$J\ddot{\theta} = rA_{e,\theta}(P - P_{atm}) - rA_{e,\theta}k_\theta\theta - rA_{e,\theta}\xi_\theta\dot{\theta} - \tau_D \tag{18}$$

$$A_v = k_p \frac{\dddot{\theta}_{ref} - \hat{f}(\cdot) - 3\lambda\ddot{e} - 3\lambda^2\dot{e} - \lambda^3 e - \eta\text{sat}(s/\phi)}{g(\cdot)} \tag{19}$$

$$\dddot{\theta} = \hat{f}(\cdot) + g(\cdot)A_v = -\frac{rA_{e,\theta}}{J}\left(\frac{P\dot{V}}{V} + k_\theta\dot{\theta}\right) + \frac{rA_{e,\theta}RT}{JV}\Psi(P_u, P_d)A_v \tag{20}$$

$$\begin{aligned}
\Delta V &= \int_{V_{dead}}^{V} dV = \int_0^{S_o} \tfrac{1}{2}2h_o\delta_{s,o}dS + \int_0^{S_i} \tfrac{1}{2}2h_i\delta_{s,i}dS \\
&= h_o\frac{r_{s,o}^2}{l\sin\alpha_o}\theta\int_0^{S_o}dS + h_i\frac{r_{s,i}^2}{l\sin\alpha_i}\theta\int_0^{S_i}dS \\
&= \left\{h_o\frac{r_{s,o}^2}{l\sin\alpha_o}S_o + h_i\frac{r_{s,i}^2}{l\sin\alpha_i}S_i\right\}\theta
\end{aligned} \tag{21}$$

Table 3.6 – Rotary FFA Sub-Step Control Law Parameters.

Parameter	Value	Parameter	Value
Robustness constant, η	2 m/s³	Closed-loop poles location, -λ	-100 Hz
Boundary layer, ϕ	1000 m/s²	Proportional gain, k_p	0.2
Hysteretic damping, ξ_θ	93.3 kPa/(deg/s)	Second moment of inertia, J	16.1 kg-mm²
Stiffness, k_θ	450 kPa/deg	$rA_{e,\theta}$	8318 mm³

IV. Prototype and Experimental Setup

Using the mechanical design reported herein, a working prototype was manufactured and thoroughly tested. Details regarding its manufacture and the testing setup are here described.

Device Manufacturing

The majority of device components were 3-D printed by fused deposition modeling (FDM) on a Makerbot Replicator 2. The material used was polylactic acid (PLA). The clamshell insert required greater flexibility and was printed in acrylonitrile butadiene styrene (ABS). Because the 2-DOF FFA

was required to be airtight, it was manufactured by laser sintering nylon 12 powder. The machine used was a 3D Systems Sinterstation 2500 Plus, located at the Milwaukee School of Engineering Rapid Prototyping Center. After the FFA was printed, unsintered support material was removed through clean-out holes, which then were sealed shut with paraffin wax (red dots in Fig. 3.1). Finally, a few of the device components were off-the-shelf journal and ball bearings made of polymer and ceramic materials, and the transmission tube was thick wall carbon fiber tube.

Experimental Setup

The 2-DOF FFA was characterized and key performance metrics were quantified using an MRI-compatible testing setup. Pneumatic transmission lines (length 6 m) connect the prototype to non-MRI compatible controller electronics, which are located just outside of the electromagnetically-shielded MRI scanner room. The transmission lines pass through a wave guide port in the shielded wall between the two rooms. Similarly, a low-pass-filtered patch panel at the wall provides D-subminiature connectors for passing the position encoder signals from the scanner room to the controller electronics. Long lengths of double-shielded twisted-pair cables connect the optical encoder modules on the prototype to the patch panel. The controller and data acquisition were implemented using MATLAB Simulink and xPC Target with a sampling rate of 2 kHz.

The pneumatic controls for the prototype consists of two on/off solenoid valves (Festo part no. CPASC1-MH1-M-P-2,5) and two 5-port/3-way proportional spool valves (Festo part no. MPYE-5-M5-010-B). The discharge coefficient for the spool valve is 0.2939. One outlet of the spool valve is plugged and the other outlet connects to the FFA bellows. One pressure transducer provides feedback at the latter outlet (Festo part no. SDE-16-10V) and another transducer measures supply pressure at the valve inlet (Festo part no. SPTW-P10R-G14-VD-M12). For two degrees of freedom, a total of four pressure transducers were used; two separate sensors measured supply pressure at each valve because the linear bellows required 345 kPa gage (50 psi) while the rotary bellows required 620 kPa gage (90 psi) to achieve adequate displacement.

V. Results

Bellows Characterization

The stiffness and hysteretic damping of the linear and rotary FFA's were each experimentally characterized. To avoid the transient effect of creep, the bellows pressure was very slowly ramped linearly from zero to 400 kPa gage for the linear FFA (to 600 kPa for the rotary FFA). Plotting the bellows displacement vs. pressure, the stiffness coefficient is the slope of a least squares linear curve fitted to the data. Referring to Fig. 3.8 for the linear FFA, this curve is the lower of the two fitted lines. The y-intercept of this line is near zero as expected. The upper of the two lines has a noticeably non-zero y-intercept and this demonstrates the hysteretic damping. To measure the

hysteretic damping, the bellows pressure was quickly depressurized from 400 kPa gage to zero, at a rate of 500 kPa/sec. Bellows displacement vs. pressure and the least squares linear fit are as shown in Fig. 3.7. Then the damping coefficient is calculated using (22), where y_{int} is the y-intercept, y_{max} the initial displacement at maximum pressure, and ω is the rate of depressurization in (mm/sec)/kPa.

$$\xi = \frac{y_{\text{int}}}{\omega y_{\text{max}}} \tag{22}$$
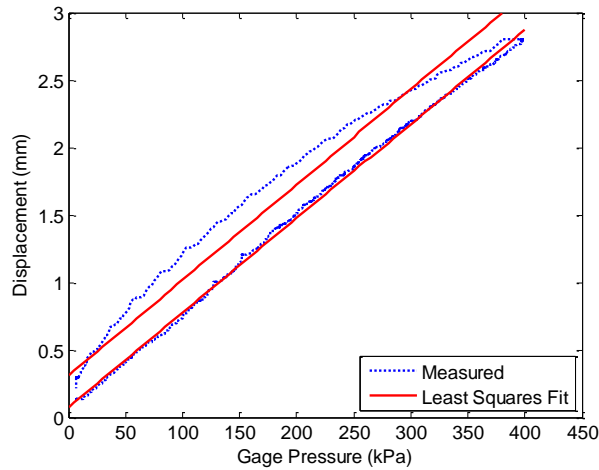
Figure 3.7 – Linear bellows characterization of stiffness and damping.

For the rotary FFA the stiffness and damping coefficients were similarly calculated using the data and least square linear fits shown in Fig. 3.8. The bellows was depressurized from 600 kPa gage to zero at a rate of 600 kPa/sec, and the units of ω are (deg/sec)/kPa. The resulting experimentally determined coefficients are reported in Tables 3.5 and 3.6. The rates of depressurization for these measurements were substantially faster than the dynamics expected in operation of the device, and thus the damping coefficients are adequately characterized for the low bandwidth of the controller.
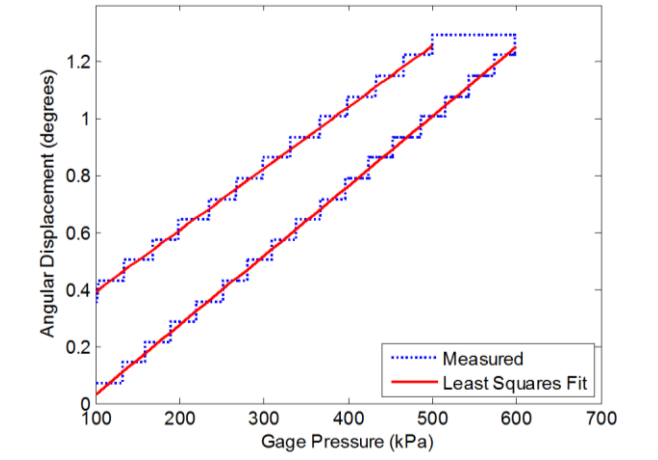
Figure 3.8 – Rotary bellows characterization of stiffness and damping.

Performance Testing

The experimentally determined stiffness coefficients were used with the hybrid controller in positioning experiments to evaluate the controls accuracy. For linear actuation of the transmission tube, the final error was 0.013 mm for the trial shown in Fig. 3.9. For rotary actuation of the transmission tube, the final error was 0.018 degrees for the trial run shown in Fig. 3.10.
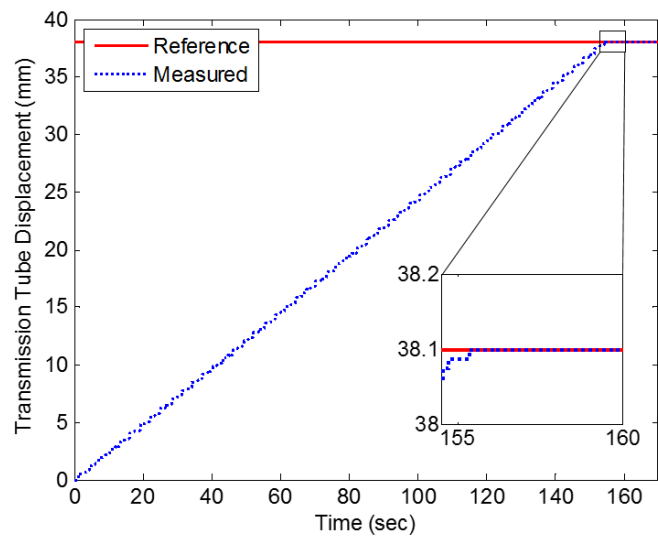
Figure 3.9 – Linear positioning of transmission tube with hybrid controller.
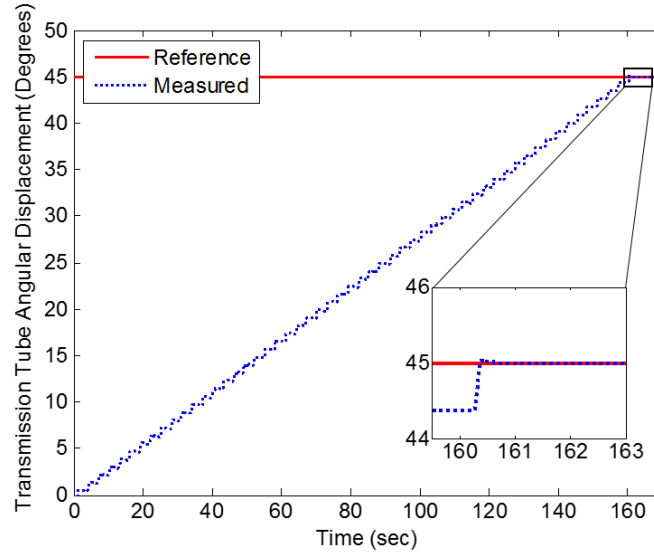
Figure 3.10 – Rotary positioning of transmission tube with hybrid controller.

A force gauge (Extech 475044) was used to measure the maximum force and torque outputs of the actuator. At a gage pressure of 414 kPa, the linear FFA produced forces of +33 N and -26.5 N. At a gage pressure of 755 kPa, the rotary FFA produced torques of 68 mN·m and -68 mN·m.

To verify that the rotary FFA results in purely rotational displacement (i.e. no longitudinal displacement), the linear constraints were removed from the actuator module and the linear position of the transmission tube was measured during actuation of the rotary FFA. The maximum longitudinal displacement observed across several trials was 0.038 mm, with actuation up to 1 degree of rotation at 480 kPa pressure.

The MR-compatibility of the hardware was tested in a 3-Tesla Philips Achieva scanner at Vanderbilt University Institute of Imaging Science (VUIIS). The sliding mode controller was unaffected by the scanner during imaging. With the hardware powered on but not in motion, no reduction in signal-to-noise ratio (SNR) of the images was observed. Even with the hardware in full motion, no observable reduction in SNR occurred.

VI. Conclusion

This paper has reported the design, manufacture, and control of an inherently-safe, MR-compatible robot to actuate concentric tube steerable needles. The bio-inspired, inchworm-like motion of the device allows for pneumatics to be used in a safer manner than traditional piston-cylinders. The design for additive manufacturing resulted in a compactly integrated prototype that fits inside the MRI scanner with the patient, and it has the potential to be a low-cost disposable in surgeries. The novel FFA design used helical bellows with both external and internal pressurization to achieve purely rotational displacements. The actuator produced bi-directional forces and torques of suitable magnitudes for loading with concentric tube needles. An innovative hybrid controller was

designed and has demonstrated precision positioning in both translations and rotations of the transmission tube. The hardware has been shown to be MR-compatible by in-scanner testing with a 3-Tesla machine.

Acknowledgment

References

[1] D. Stoianovici, A. Patriciu, D. Petrisor, D. Mazilu, and L. Kavoussi, "A New Type of Motor: Pneumatic Step Motor," *IEEE/ASME Trans Mechatronics*, 12(1):98-106, 2007.

[2] M. Muntener, A. Patriciu, D. Petrisor, M. Schär, D. Ursu, D.Y. Song, and D. Stoianovici, "Transperineal Prostate Intervention: Robot for Fully Automated MR Imaging—System Description and Proof of Principle in a Canine Model," *Radiology*, 247(2):543-549, 2008.

[3] N. Zemiti, I. Bricault, C. Fouard, B. Sanchez, and P. Cinquin, "LPR: A CT and MR-Compatible Puncture Robot to Enhance Accuracy and Safety of Image-Guided Interventions," *IEEE/ASME Trans Mechatronics*, 13(3):306-315, 2008.

[4] M.R. Van den Bosch, M.R. Moman, M. van Vulpen, J.J. Battermann, E. Duiveman, L.J. van Schelven, H. de Leeuw, J.J.W. Lagendjik, and M.A. Moerland, "MRI-guided robotic system for transperineal prostate interventions: proof of principle," *Phys Med Biol*, 55:133-140, 2010.

[5] A. Melzer, B. Gutmann, T. Remmele, R. Wolf, A. Lukoscheck, M. Bock, H. Bardenheuer, and H. Fischer, "Innomotion for Percutaneous Image-Guided Interventions: Principles and Evaluation of this MR- and CT-Compatible Robotic System," *IEEE Eng Med Biol Mag*, pp. 66-73, May/June 2008.

[6] J. Tokuda, S. Song, G.S. Fischer, I.I. Iordachita, R. Seifabadi, N. Cho, K. Tuncali, G. Fichtinger, C. Tempany, and N. Hata, "Preclinical evaluation of an MRI-compatible pneumatic robot for angulated needle placement in transperineal prostate interventions," *Int J CARS*, 7:949-957, 2012.

[7] K. Masamune, E. Kobayashi, Y. Masutani, M. Suzuki, T. Dohi, H. Iseki, and K. Takakura, "Development of an MRI-Compatible Needle Insertion Manipulator for Stereotactic Neurosurgery," *J Image Guid Surg*, 1:242-248, 1995.

[8] N. Tsekos, A. Khanicheh, E. Christoforou, and C. Mavroidis, "Magnetic Resonance-Compatible Robotic and Mechatronics Systems for Image-Guided Interventions and Rehabilitation: A Review Study," *Annu Rev Biomed Eng*, 9:351-387, 2007.

[9] G. Sutherland, I. Latour, A.D. Greer, T. Fielding, G. Feil, and P. Newhook, "An Image-Guided Magnetic Resonance-Compatible Surgical Robot," *Neurosurgery*, 62(2):286-293, 2008.

[10] H. Su, D. Cardona, W. Shang, A. Camilo, G.A. Cole, D.C. Rucker, R.J. Webster III, and G.S. Fischer, "A MRI-Guided Concentric Tube Continuum Robot with Piezoelectric Actuation: A Feasibility Study," *IEEE International Conference on Robotics and Automation*, pp. 1939-1945, 2012.

[11] T. Fisher, A. Hamed, P. Vartholomeos, K. Masamune, G. Tang, H. Ren, and Z. T. H. Tse, "Intraoperative magnetic resonance imaging-conditional robotics devices for therapy and diagnosis," *Proc IMechE Part H: J Engineering in Medicine*, 228(3):303-318, 2014.

[12] R.J. Webster III, J.M. Romano, and N.J. Cowan, "Mechanics of Precurved-Tube Continuum Robots," *IEEE Transactions on Robotics*, 25(1):67-78, 2009.

[13] D.C. Rucker, B.A. Jones, and R.J. Webster III, "A geometrically exact model for externally loaded concentric tube continuum robots," *IEEE Transactions on Robotics*, 26(5):769-780, 2010.

[14] J. Burgner, D.C. Rucker, H.B. Gilbert, P.J. Swaney, P.T. Russell III, K.D. Weaver, and R.J. Webster III, "A Telerobotic System for Transnasal Surgery," *IEEE/ASME Transactions on Mechatronics*, 19(3):996-1006, 2014.

[15] P.J. Swaney, H.B. Gilbert, R.J. Webster III, P.T. Russell III, and K.D. Weaver, "Endonasal Skull Base Tumor Removal Using Concentric Tube Continuum Robots: A Phantom Study," *Journal of Neurological Surgery Part B: Skull Base*, In Press.

[16] H.B. Gilbert and R.J. Webster III, "Can concentric tube robots follow the leader?" *IEEE Int Conf Robot Autom*, pp. 4881-4887, May 2013, Karslruhe.

[17] H.B. Gilbert, J. Neimat, and R.J. Webster III, "Concentric Tube Robots as Steerable Needles: Achieving Follow-the-Leader Deployment," *IEEE Trans Robotics*, .

[18] H.M. Paynter, "Low-Cost Pneumatic Arthrobots Powered by Tug-&-Twist Polymer Actuators," *Japan/USA Symposium on Flexible Automation*, 1:107-110, 1996.

[19] H.M. Paynter, "Thermodynamic Treatment of Tug-&-Twist Technology: Part 1 – Thermodynamic Tugger Design," *Japan/USA Symposium on Flexible Automation*, 1:111-117, 1996.

[20] H.M. Paynter and J.M. Juarez, "Thermodynamic Treatment of Tug-&-Twist Technology: Part 2 – Thermodynamic Twister Design," *IEEE/ASME Int Conf Advanced Intelligent Mechatronics*, 1999.

[21] J.F. Wilson and G. Orgill, "Linear Analysis of Uniformly Stressed, Orthotropic Cylindrical Shells," *ASME J Applied Mechanics*, 53(2):249-256 1986.

[22] G. Orgill and J.F. Wilson, "Finite Deformations of Nonlinear, Orthotropic Cylindrical Shells," *ASME J Applied Mechanics*, 53(2):257-265, 1986.

[23] J.F. Wilson, "Mechanics of fluid-activated, clustered satellite bellows," *Int J Solids Structures*, 45:4173-4183, 2008.

[24] I. Gaiser, S. Schulz, H. Breitwieser, and G. Bretthauer, "Enhanced Flexible Fluidic Actuators for Biologically Inspired Lightweight Robots with Inherent Compliance," *Proc IEEE Int Conf Robotics Biomimetics*, pp. 1423-1428, Tianjin, Dec 2010.

[25] S. Zientarski, "Additive Manufacturing of Fully Functional Fluid Power Components," *Proc. NCUR*, 2010.

[26] A. Grzesiak, R. Becker, and A. Verl, "The Bionic Handling Assistant: a success story of additive manufacturing," *Assembly Automation*, 31(4):329-333, 2011.

[27] S. Rajagopalan and M.R. Cutkosky, "Tolerance Representation for Mechanism Assemblies in Layered Manufacturing," *Proc ASME Design Engineering Technical Conference*, pp. 1-10, Sept 1998, Atlanta.

[28] J. Won, K.J. DeLaurentis, and C. Mavroidis, "Fabrication of a Robotic Hand using Rapid Prototyping," *Proc ASME Design Engineering Technical Conference*, pp. 1-7, Sept 2000, Baltimore.

[29] K.J. DeLaurentis and C. Mavroidis, "Rapid Fabrication of a Non-assembly Robotic Hand with Embedded Components," *Assembly Automation*, 24(4):394-405, 2004.

[30] T. Lalibert and C.M. Gosselin, "Practical Prototyping," *IEEE Robotics Automation Magazine*, Sept 2001.

[31] S. Proulx and J. Plante, "Design and Experimental Assessment of an Elastically Averaged Binary Manipulator Using Pneumatic Air Muscles for Magnetic Resonance Imaging Guided Prostate Interventions," *J Mech Des*, 133(11):1-9, 2011.

[32] K. Ikuta, I. Hironobu, S. Katsuya, and Y. Takahiro, "Micro Hydrodynamic Actuated Multiple Segments Catheter for Safety Minimally Invasive Therapy," *Proc IEEE Int Conf Robot Automat*, pp. 2640-2645, 2003.

[33] H. Haga, T. Matsunaga, W. Makishi, K. Totsu, T. Mineta, and M. Esashi, "Minimally Invasive Diagnostics and Treatment using Micro/Nano Machining," *Minimally Invasive Therapy*, 15(4):218-225, 2006.

[34] A. De Greef, P. Lambert, and A. Delchambre, "Towards Flexible Medical Instruments: Review of Flexible Fluidic Actuators," *Precision Engineering*, 33(4):311-321, 2009.

[35] H-W Kang, I.H. Lee, and D-W Cho, "Development of a micro-bellows actuator using micro-stereolithography technology," *Microelect Eng*, 83(7):1201-1204, 2006.

[36] J.E. Slightam and V.R. Gervasi, "Novel Integrated Fluid-Power Actuators for Functional End-Use Components and Systems via Selective Laser Sintering Nylon 12," *23rd Ann Int Solid Freeform Fabrication Symp*, 2012, Austin, TX, pp. 197-211.

[37] E. Richer and Y. Hurmuzlu, "A High Performance Pneumatic Force Actuator System: Part I—Nonlinear Mathematical Model," *ASME J Dyn Syst, Meas Control*, 122(3):416-425, 2000.

[38] E. Richer and Y. Hurmuzlu, "A High Performance Pneumatic Force Actuator System: Part II—Nonlinear Controller Design," *ASME J Dyn Syst, Meas Control*, 122(3):426-434, 2000.

[39] Y. Zhu and E.J. Barth, "Accurate Sub-Millimeter Servo-Pneumatic Tracking using Model Reference Adaptive Control (MRAC)," *Int J Fluid Power*, 11(2):49-57, 2010.

[40] D.B. Comber, E.J. Barth, and R.J. Webster III, "Design and Control of an MR-Compatible Precision Pneumatic Active Cannula Robot," *ASME J Medical Devices*, 8(1):011003-1-7, 2014.

[41] D.B. Comber, R.J. Webster III, J.S. Neimat, and E.J. Barth, "Open-Loop Tip Accuracy of an MRI-Compatible Active Cannula Robot," *Proc. Hamlyn Symp Medical Robotics*, pp. 112-113, Jun 2013, London.

[42] D.B. Comber, J.E. Slightam, V.R. Gervasi, R.J. Webster III, and E.J. Barth, "Design and Precision Control of an MR-Compatible Flexible Fluidic Actuator," *Proc. ASME/Bath Symposium on Fluid Power & Motion Control*, pp. 1-9, 2013, Sarasota, FL.

[43] M. Di Giovanni, 1982, *Flat and Corrugated Diaphragm Design Handbook*, Marcel Dekker, New York, pp. 130-192.

[44] J.F. Wilson and N. Inou, "Bellows-Type Springs for Robotics," *Proc. of Advanced Spring Technology JSSE 60th Anniversary Int. Symposium*, pp. 109-119, Nov 2007, Nagoya, Japan.

<u>Addendum to Manuscript 2: Improved Controller Design</u>

<u>A-I. Introduction</u>

The speed of device operation proved to be unsatisfactorily slow using the hybrid controller as previously described. An improved controller was needed that could simultaneously (i.e. not serially) translate and rotate a helically pre-curved tube for follow-the-leader deployment of the needle [1]. A helical pre-curvature was given to a superelastic nitinol tube by heating with electric current [2]. This tube was used as a loading on the actuation unit for testing of the improved controller. Controller design and performance are here reported.

<u>A-II. Controller Design</u>

To achieve follow-the-leader deployment for the helically pre-curved tube, the rotary and linear FFA's alternately increment the angular and linear displacement of the tube. The increment sizes are related to one another by the pitch p and radius r of the helix. An angular increment θ_{step} of 1 degree was chosen for the rotary FFA and the corresponding linear increment x_{step} is given by (23).

$$x_{step} = \theta_{step}\sqrt{r^2 + p^2} \tag{23}$$

Incremental displacement is implemented using four control valves, one for each of the functional components shown in Fig. 3.11: linear gripper, linear FFA, rotary FFA, and rotary gripper. The logic for the control valves was implemented in a Stateflow chart in MATLAB Simulink. The chart blocks for counterclockwise and clockwise motion of the helix are shown in Figs. 3.12 and 3.13, respectively. Chart inputs are incremental x_{step} and θ_{step} and the final desired linear and rotary displacements, x_{final} and θ_{final}. Chart outputs are the two binary, on/off valve commands (x_{grip} and θ_{grip}) and reference signals x_{des} and θ_{des}. The reference signals are inputs to the sliding mode control blocks, which output commands to the two mass flow valves. In one iteration of the control valve sequence, x_{des} and θ_{des} increment or decrement by the amounts x_{step} and θ_{step}, and the sliding mode controllers respond accordingly. Then, binary reset commands are sent to the mass flow valves to reset the linear and rotary FFA's before the next iteration of the sequence.
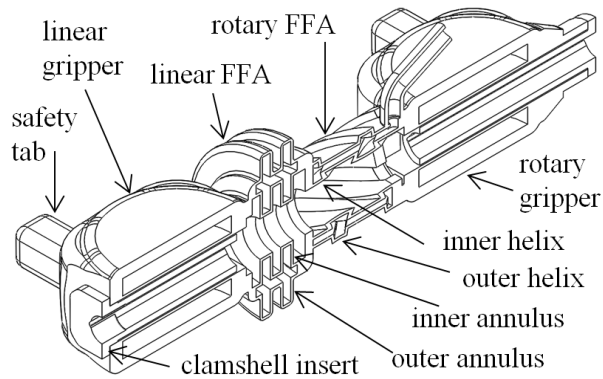
Figure 3.11 – Cross-section of linear and rotary actuating mechanism.
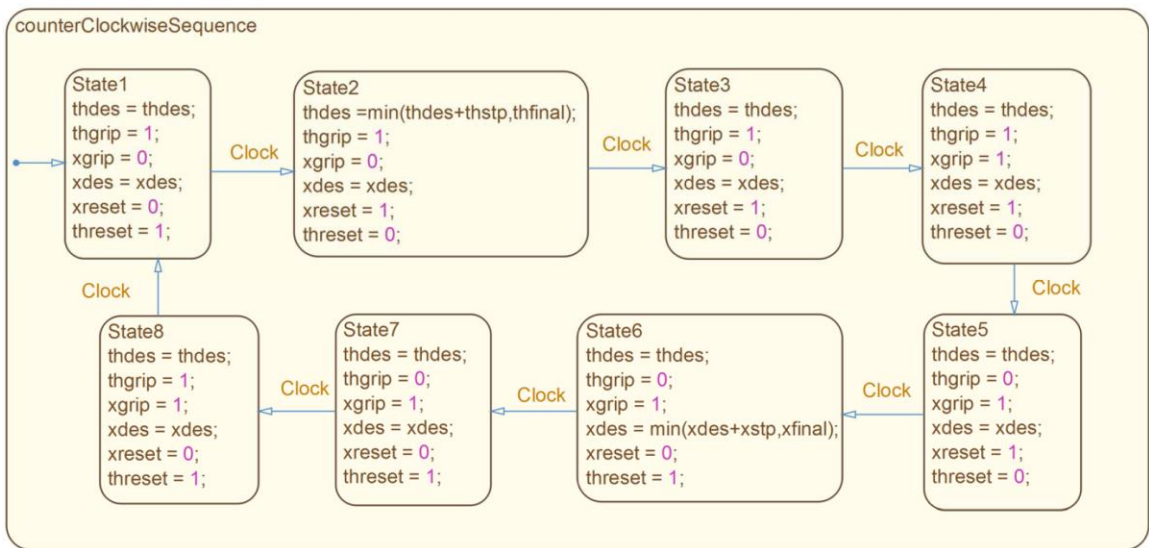
Figure 3.12 – Stateflow chart for counterclockwise (positive displacement) motion of helical tube.
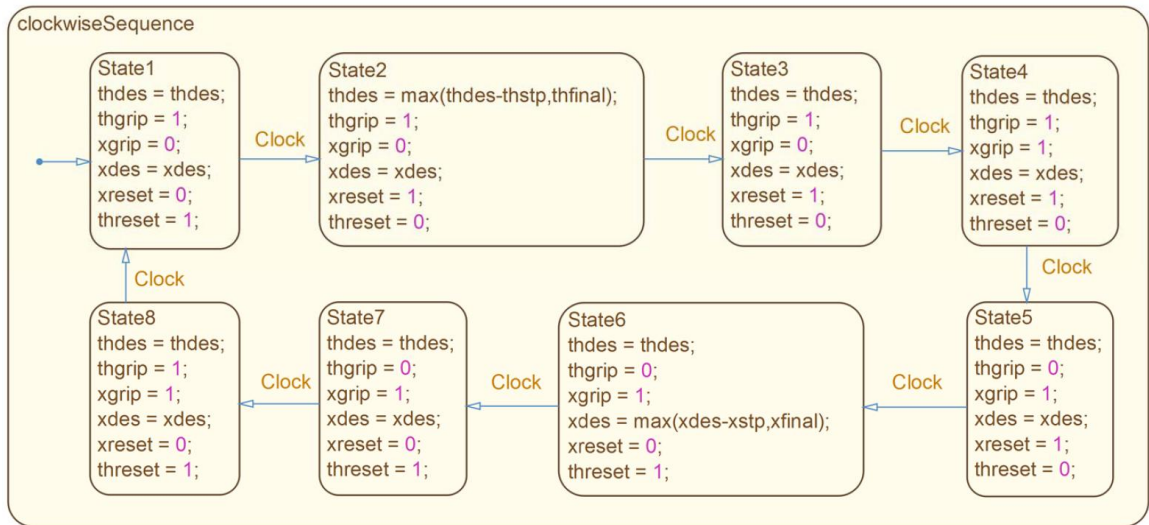
Figure 3.13 – Stateflow chart for clockwise (negative displacement) motion of helical tube.

A-III. Results

Successful trajectory tracking with simultaneous translation and rotation of the transmission tube is shown in Figs. 3.14 and 3.15. The transmission tube was loaded with the helix-shaped needle deploying out of a straight outer cannula into a gelatin-based phantom. Final errors at steady-state were 0.1 degrees and 0.12 mm.
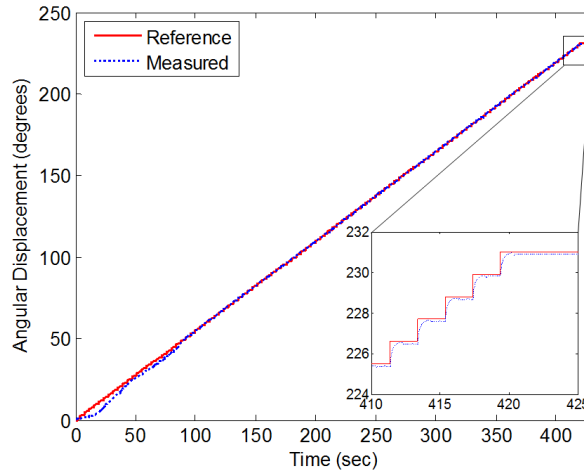
Figure 3.14 – Angular displacement tracking of a reference trajectory (needle insertion).
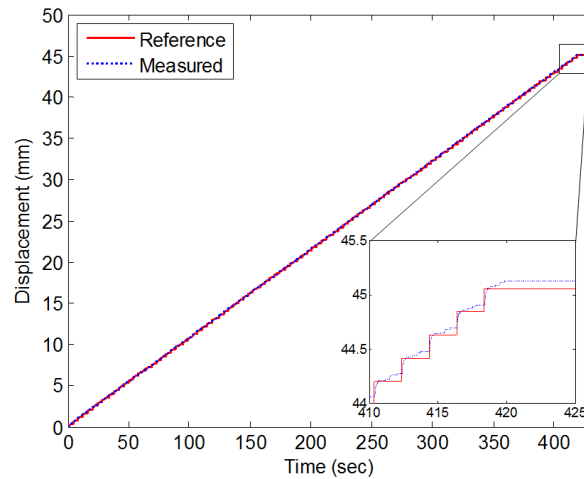
Figure 3.15 – Displacement tracking of a reference trajectory (needle insertion).

References

[1] H.B. Gilbert, J. Neimat, and R.J. Webster III, "Concentric Tube Robots as Steerable Needles: Achieving Follow-The-Leader Deployment," *IEEE Trans. Robotics*, 31(2):246-258, 2015.

[2] H.B. Gilbert and R.J. Webster III, "Rapid, Reliable Shape Setting of Nitinol for Concentric Tube Robots," *IEEE Trans. Biomedical Engineering*, [In Review].

Chapter 4 – Design and Validation of a Concentric Tube Robot for MRI-Guided Hippocampotomy

David B. Comber, E. Bryn Pitt, Yue Chen, Collin H. Grimes, Joseph S. Neimat, Eric J. Barth, and Robert J. Webster III

Vanderbilt University, Nashville, TN

Prologue

This chapter presents a robotic system concept for MRI-guided transforamenal ablation. The actuation unit from the previous chapter is used to robotically control under MRI guidance a concentric tube needle. A custom-designed concentric tube needle prototype for the transforamenal approach is described. The envisioned clinical workflow is presented. Forward and differential kinematics of the concentric tube needle are formulated and combined with the low-level robot controls from the previous chapter. The accuracy of the system is reported as tested with an optical tracker and a standard MRI scanner.

Abstract

This paper reports the design and validation of an MRI-guided concentric tube needle robot to treat epilepsy. The curved trajectory capabilities of this steerable needle enable access to the deep brain through the foramen ovale. This transforamenal approach would eliminate drilling of the skull and substantially minimize passage through untreated brain tissue. We hypothesized that a steerable needle comprising one superelastic tube of helical pre-curvature concentric with an inner, straight, ablation probe could traverse a follow-the-leader trajectory from the foramen ovale, to and through the hippocampus head-to-tail. To investigate the transforamenal approach, dual CT/MRI scans of a de-identified patient brain were registered and segmented. The resulting skull and hippocampus models were used to design a concentric tube needle. In simulation with this design, mean distance of the needle trajectory from the medial axis of the hippocampus was 0.88 mm. A superelastic nitinol tube was shape set to the helix corresponding to this planned trajectory. A radiofrequency ablation electrode was manufactured and tested. The accuracy of robotic control of the prototype needle was measured with an optical tracker. Needle tip position errors were 0.89, 1.14, and 1.02 mm for three placements. Robotic control was tested under MRI guidance using an MR-compatible actuation unit. For three placements in a phantom, needle tip errors were 3.07,

1.11, and 3.19 mm. Regarding MR-compatibility, no reduction in signal-to-noise ratio was observed with the robot in full motion. These results indicate that the robotic system reported here could feasibly enable a foramen ovale approach to epilepsy treatment.

I. Introduction

Research towards an MRI-guided robotic treatment for epilepsy is motivated by the high prevalence of and severe disability caused by this neurological disease. Prevalence is estimated at 0.5-1.0%, and epilepsy is said to account for 1 percent of the global burden of disease [1, 2]. Forty-seven percent of epilepsy patients obtain seizure control with a first anti-epileptic drug (AED), and an additional 13 percent with a second AED, while 40 percent of epilepsy patients are refractory to medication [3]. These medically-refractory patients are estimated to have a 30-fold increase in lifetime disease cost and moreover are at substantial risk for sudden unexplained death in epilepsy (SUDEP) [4].

Surgical resection of the hippocampus, where seizures commonly begin, is a potentially permanent cure for patients with medically-refractory epilepsy. Studies have shown a seizure-free rate following hippocampectomy of 70 to 80 percent [5, 6]. Despite these compelling findings, several studies in nations with centralized healthcare have demonstrated 50-90% underutilization of epilepsy surgery [5-7].

Recent technological advances including laser tissue ablation and MR thermography have reinvigorated interest in minimally invasive therapies for epilepsy. These techniques allow for real time visualization of ablation volumes as they are performed. Clinical trials have been reported for three different MRI-guided laser ablation systems: Visualase (Medtronic, Dublin), ClearPoint (MRI Interventions, Inc., Irvine, CA), and NeuroBlate (Monteris Medical, Inc., Plymouth, MN). Curry et al. reported seizure freedom at 3-month follow up for 5 pediatric patients treated using the Visualase Thermal Therapy System [8]. For a small series of procedures using the Visualase laser applicator and ClearPoint stereotactic frame [9], Willie et al. reported a 6-month seizure freedom rate in 7 of 13 patients and substantial improvement for an additional 3 patients [10]. Hawasli et al. effectively treated one case of medically-refractory epilepsy using the Monteris Neuroblate System [11].

The procedure using these systems still requires a full operating room preparation due to drilling of the skull, and the seizure outcomes to date have been worse than selective amygdalohippocampectomy. Additionally, their needles are limited to linear trajectories and therefore cannot lesion the entire hippocampus even with directionally aiming probes. The total volume of hippocampus ablated could potentially be improved by deploying a concentric tube needle in a nonlinear trajectory. Moreover, employing such a curved trajectory it is possible to approach the hippocampus from the foramen ovale and thereby eliminate the need to drill an opening in the skull.

This paper reports a robotic system to enable transforamenal ablation under MRI guidance.

The system comprises a concentric tube robot, an MR-compatible actuation unit, an ablation probe, and MRI guidance. MR imaging is used to visualize and guide the concentric tube needle along a planned trajectory, and MR thermometry is used to monitor delivery of thermal ablative therapy. Curvilinear trajectories are realized using a concentric tube needle. This continuum robot typically comprises multiple, nested tubes of superelastic nitinol. Controllable, curvilinear motion is realized when axial translations and rotations are applied to the tube bases. For an overview of this technology, see [12-14].

Application of the concentric tube robot as a steerable needle in soft tissue requires the robot to deploy in a follow-the-leader trajectory. That is, as the needle deploys, its backbone must follow the path created by the needle tip, to avoid shearing the surrounding tissue. The feasibility of follow-the-leader trajectories was recently demonstrated for a concentric tube robot comprising two tubes both of helical pre-curvature; trajectory error in free-space as measured by a pair of stereo cameras was 2 mm [15]. To effectively constrain the needle trajectory to follow-the-leader deployment, a robotic actuation unit is required. For MRI-guided interventions, this actuation unit must be MR-compatible.

Reporting RMS errors at needle tip of 0.61 to 2.24 mm, Su et al. preliminarily showed the feasibility of an MRI-guided concentric tube robot [16]. However, the trial insertions did not close the loop with robot inverse kinematics to target specific points in MRI scanner space. In addition, the footprint of their piezomotor-driven actuation unit could not be configured to fit adjacent to the upper torso of the patient inside the scanner. Thus, our transforamenal approach to deep brain access required an anatomy-specific design for the robot actuation unit.

The remainder of this paper is organized as follows: Section II presents the transforamenal ablation system concept. Section III describes the robotic system comprising the concentric tube robot and actuation unit. Section IV presents the envisioned clinical workflow. Section V describes the design, fabrication, and characterization of the concentric tube needle. Section VI outlines the robotic controls. Section VII presents experimental setup and results for testing with an optical tracker and a 3T MRI scanner. Section VIII discusses the experimental results and presents conclusion of the work.

II. System Overview

The system concept for robotic transforamenal ablation is illustrated in Fig. 4.1. A robot actuation unit is positioned with the patient under general anesthesia within a standard MRI scanner. The robot is suspended above the patient's torso using an arc-shaped frame affixed to the patient couch. A flexible receiver coil is shown because it is less likely to cause obstructions than a bird cage coil.
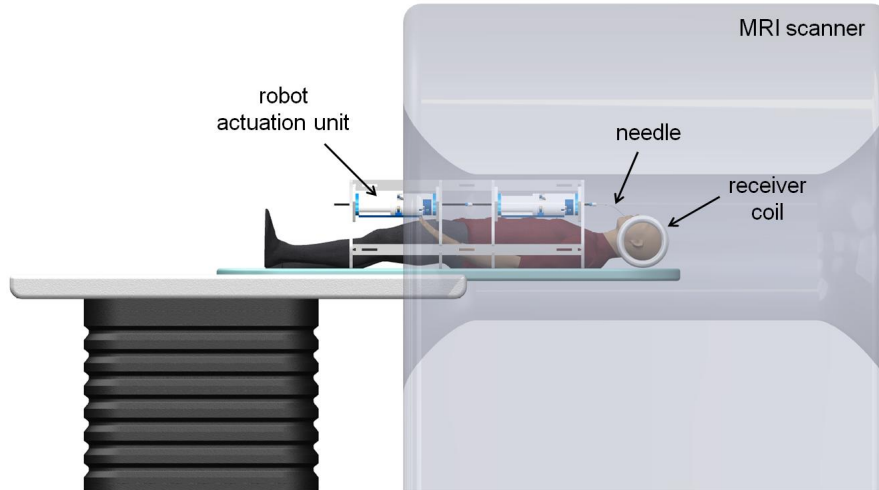
Figure 4.1 – Illustration of robotic transforamenal ablation system concept.

Photographs of functional prototypes for the system hardware are shown in Fig. 4.2. This layout fits inside a Philips Achieva 3T scanner (bore size: 60 cm). The hardware includes an aiming device to adjust the entry angle of the docking tube. The aiming device affixes to the patient via a bite block; a lockable ball-and-socket joint is used to orient the docking tube, which functions as a guiding port for delivery of the concentric tube robot. The bite block firmly secures to the upper maxilla using dental alginate to create a pseudo-vacuum. The non-invasive nature of this form of head fixation is ideal for our procedure, which we envision will take place from start to finish in a radiology clinic and not require use of a surgical suite. Cranial immobilization by vacuum-assisted maxillary fixation has been reported for cannulation of the foramen ovale, using the Vogele-Bale-Hohner (VBH) Head Holder device [17].
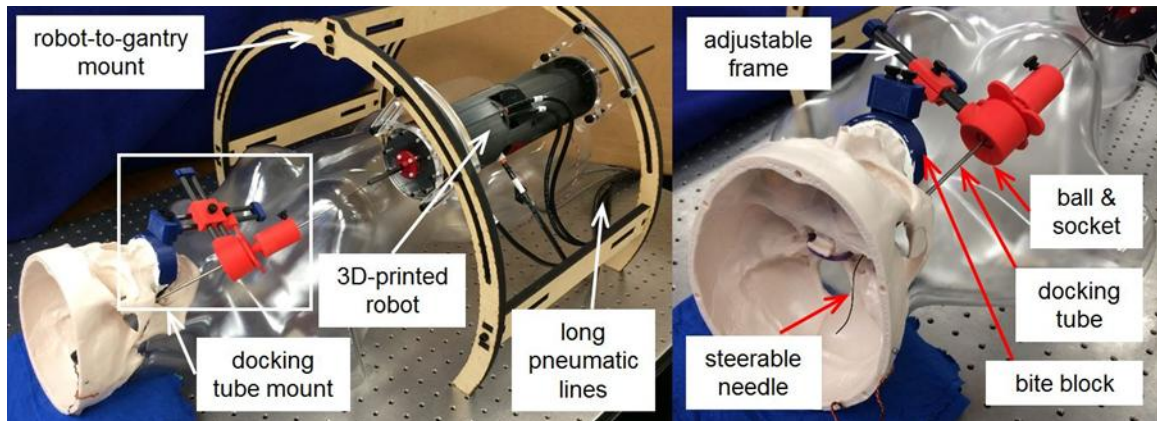
Figure 4.2 – *Left:* Robot actuation unit and aiming device are compactly positioned with a manikin. *Right:* Close-up view of aiming device and needle.

The needle in the system is made up of two parts: a manually-placed docking tube and a robotically-actuated concentric tube needle. The needle design is illustrated in Fig. 4.3 along with segmented models of the hippocampus and skull. The concentric tube needle comprises an outer,

helically pre-curved, superelastic tube and an inner ablation probe. The idea is for the concentric tube needle to deploy through a straight outer cannula, which is manually inserted beneath the cheek skin and docked to the foramen ovale.

Motion controlled at its proximal end by the robot actuation unit, the helical tube maneuvers the ablation probe toward and into the hippocampus. Deployment is guided using real-time MRI for visualization of the target and needle. The concentric tube robot continues along the medial axis of the hippocampus to its tail, and then the ablation probe extends beyond the helical tube to the configuration shown in Fig. 4.3. The ablation is monitored using MR thermal imaging and then the robot partially retracts the helical tube and probe such that the middle and head portions of the hippocampus can be likewise ablated.
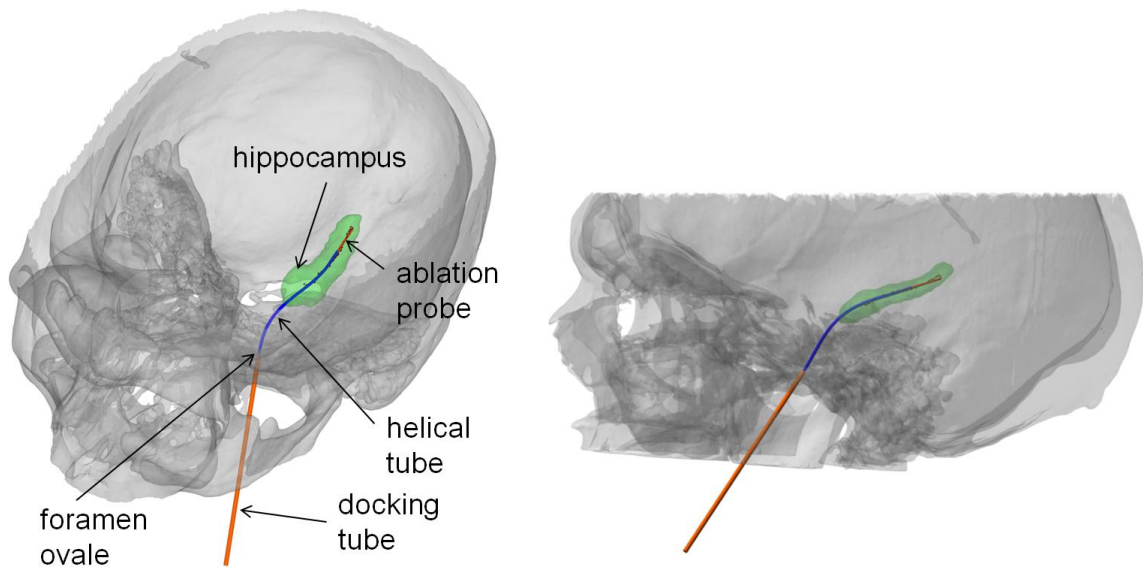
Figure 4.3 – Transforamenal deployment of concentric tube robot along medial axis of hippocampus.

III. Robotic System

Concentric Tube Robot as Steerable Needle

Application of the concentric tube robot as a steerable needle (i.e. not a manipulator inside an empty or fluid-filled cavity or lumen) requires a follow-the-leader design. That is, the backbone of the needle must follow the path created by the leading tip so as to avoid shearing adjacent tissue. Gilbert et al. proved that concentric tube robots can indeed achieve follow-the-leader deployment, provided the tube designs and actuator joint displacements satisfy certain constraints [15]. They showed that for a follow-the-leader design using two tubes, the two tubes must both have circular precurvatures lying in the same plane or both helical precurvatures with equal Frenet-Serret torsion. A trivial design in which one of the two tubes has zero precurvature can also perfectly deploy as

follow-the-leader.

For the transforamenal ablation application, the latter design was preferred. The ablation probe has zero precurvature and the superelastic nitinol tube was given a helical precurvature. A photograph of the needle prototype is shown in Fig. 4.4. Beginning with the ablation probe retracted within the helical tube, a follow-the-leader trajectory is realized by actuating the helical tube at the appropriate rates of arc length and angular velocity, such that the needle "corkscrews" through the tissue. Simultaneously, the ablation probe is actuated at the same rate of arc length velocity to ensure it remains fully overlapped with the helical tube, thereby maintaining a constant helical shape resulting from the overlapping portions.
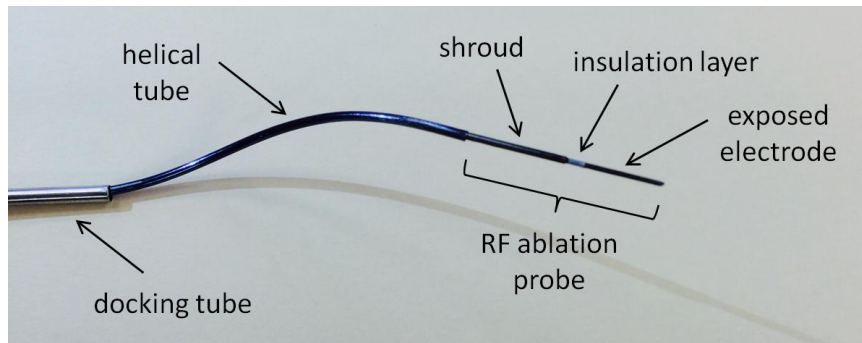
Figure 4.4 – Concentric tube needle prototype for transforamenal, follow-the-leader applications.

Robot Actuation Unit

To ensure the concentric tube needle is actuated with joint velocities that adhere to follow-the-leader conditions, a robot is essentially required. A thorough description of mechanical design and controls formulation for the robot actuation unit is found in [18]. A brief review is in order here. To satisfy requirements for compactness and sterilizability, the robot hardware was designed for additive manufacturing. By selective laser sintering (SLS) nylon powder, the actuators and mechanisms were printed simultaneously as a monolithic structure of compactly integrated components. The resulting prototype is easy to sterilize because, unlike a traditional assembly, the monolithic structure does not have separate components between which contaminants could lodge themselves. A cross-sectional view of this monolithic structure is shown in Fig. 4.5, along with a photograph of the complete actuation unit. A thick-wall, large diameter tube runs the entire length of the device from back to front. Outside the front housing of the robot module, this transmission tube steps down to the helical tube. Using a collet and clamping nut assembly, the needle can be interchanged for other sizes and shapes of sterilized tube.
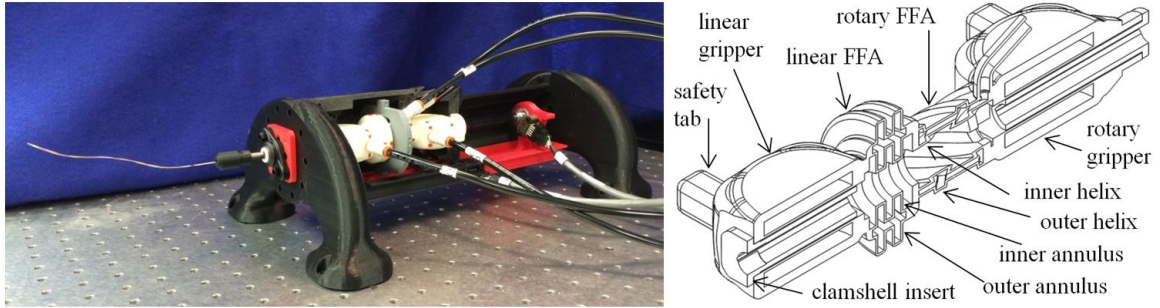
Figure 4.5 – *Left*: Photograph of prototype with helix-shaped concentric tube needle, with one half of the device housing removed to show inner parts. *Right*: Cross-section view of actuators.

One linear flexible fluidic actuator (FFA) and one rotary FFA bi-directionally translate and rotate the transmission tube that carries the needle. Displacement in one direction occurs with expansion of the FFA when it is pressurized, and displacement in the opposing direction occurs using the material compliance of the FFA when it is de-pressurized. Two grippers firmly grasp and release the transmission tube. Each gripper consists of two diaphragms located above and below the transmission tube. When inflated, the diaphragms deflect a clamshell insert, which firmly clamps against and around the transmission tube.

The actuating mechanism is secured to the robot housing such that the portion between the linear and rotary FFA's is stationary. Thus, the linear and rotary grippers are attached to the free-moving end of the linear FFA or rotary FFA, respectively. Their displacements are limited to small increments by safety tabs that interface with mechanical stops on the robot housing. A fail-safe hardware configuration is thereby achieved. To deploy the helical tube in a follow-the-leader manner, the rotary and linear FFA's alternately increment the angular and linear displacement of the tube in small increments related by the pitch and radius of the helix.

Incremental displacement is implemented using four control valves. Two on/off solenoid valves each respectively engage and disengage one of the two grippers. Two mass-flow proportional spool valves each respectively control the linear FFA and rotary FFA. Similar to prior work, a sliding mode control law was formulated to command the spool valves for sub-millimeter positioning of the FFA's [19]. Linear and rotary displacement of the transmission tube is measured by MR-compatible optical encoders. The valves and pressure transducers are not MR-compatible and connect to the robot via transmission lines of length 7 m.

Robot Ablation Tip

While our design is agnostic to the type of ablation technology, a radiofrequency (RF) ablation probe was custom designed and manufactured from nitinol for maximum compatibility with the helically precured nitinol tube. The efficacy and safety of RF ablation under MRI guidance has been previously demonstrated [20-22]. In addition, currently available laser or acoustic ablation

probes are too large to pass through the helical tube, the maximum size of which is constrained by the anatomy of the foramen ovale.

The ablation probe as depicted in Fig. 4.4 consists of three main parts. The electrode is a superelastic nitinol wire. It is insulated by a thin layer of polyester heat-shrinkable tubing. A sheath of thin-wall nitinol tubing acts as a protective shroud around the insulation to prevent the sharp edge of the helical tube from scraping it. The probe was tested in uncooked chicken breast with an RF generator (Vulcan, Smith & Nephew, Inc., Memphis, TN). Using a pulsed sequence of 60 seconds on and 15 seconds off for a total of 15 minutes, lesions greater than 1 cm diameter were observed.

IV. Clinical Workflow

The envisioned surgical workflow for the procedure is summarized in Fig. 4.6. Pre-operative CT and MRI scans are used to segment the skull and amygdalohippocampal complex, respectively. The segmented models are used with path planning software to find an optimal trajectory and the corresponding pre-curvature parameters of the helical tube and orientation angles (pitch and yaw) of the docking tube. The helical tube is pre-curved to match the plan and then sterilized.

The entire procedure occurs in a standard radiology clinic with the patient under general anesthesia in the supine position on a transfer board. The cranium is immobilized using a maxillary fixation system, which is then secured to the transfer board. The surgeon makes a small incision on the patient's cheek and cannulates the foramen using a C-arm machine. Based on the fluoroscopic image, the surgeon uses the aiming device to orient the docking tube to correct pitch and yaw angles. The patient is then transferred to the diagnostic MRI machine.

A frame of fiducial markers specific to the maxillary fixation system is used to do a point-based registration. The pre-op plan is also registered by a non-rigid registration to the intra-operative scan. After registration, the fiducial frame is removed, and positioning of the docking tube is confirmed or adjusted if necessary. Then, the MR-compatible actuation unit is positioned using the arc-shaped frame as in Fig. 4.2. At the distal end of the actuation unit, the concentric tube needle is aligned with and partially inserted into the docking tube. The actuation unit is secured to the transfer board and the patient is returned to isocenter. The needle is registered to MRI, and the planned trajectory is reviewed by the surgeon and modified if desired. The actuation unit then assists the surgeon in placing the needle along the planned trajectory. Real-time MRI is used to confirm or adjust placement. Finally, the hippocampotomy is performed using thermal ablation, monitored and confirmed by MR thermal imaging for thermal dosimetry.

V. Helical Needle Design

A medical image analysis was conducted to characterize the workspace and constraints for design and selection of tubes for the concentric tube robot. Dual CT/MRI volumes were segmented

using free and open source software, 3D Slicer (www.slicer.org). The CT and MRI volumes were registered by a rigid transformation plus scaling using the software's BRAINSFit module [23]. The skull was segmented from CT using an automated threshold. The hippocampus and amygdala were segmented manually from MRI and reviewed and confirmed by our neurosurgeon. The segmented anatomical models were imported to MATLAB to overlay with the kinematic model of the concentric tube needle. The hippocampus model was converted from triangular-polygon mesh to voxel format and then the medial axis was computed using the skeletonizing method found in [24]. A simplified geometric representation of a 3-D digital object, the medial axis is the locus of the centers of all maximal spheres inscribed within the object, where maximal spheres touch more than one point on the object boundary.

Our objective in this design was to cause the ablator to pass as close to the medial axis as possible. The rationale for this was that if the ablator radiates heat evenly in all directions, it would be most likely to achieve uniform coverage of the hippocampus if it traveled along the medial axis. However, we note that it need not travel perfectly along the axis, as there are examples of successful ablations of the hippocampus being performed substantially away from the medial axis [8, 10-11].
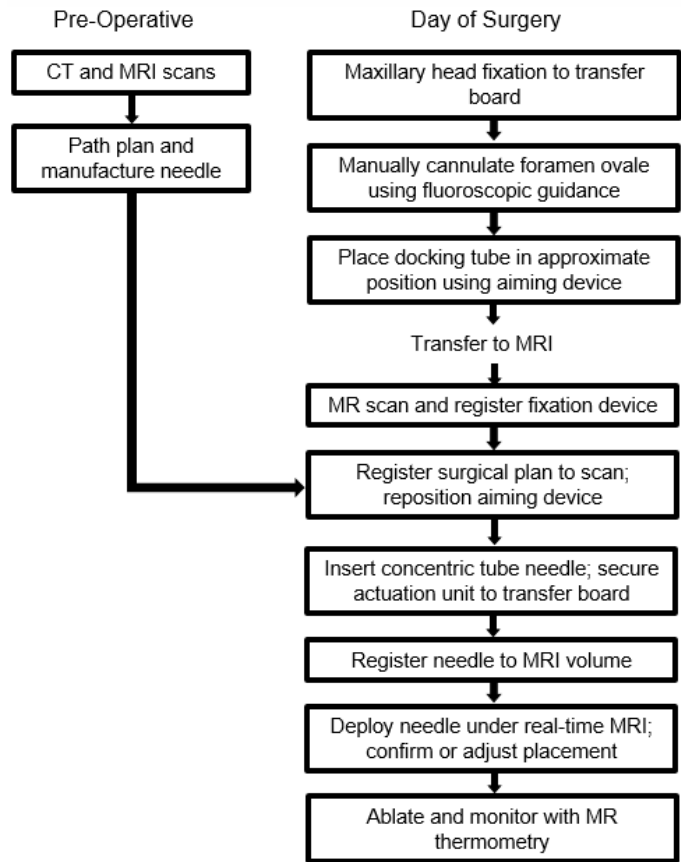
Figure 4.6 – Surgical workflow for robotic MRI-guided transforamenal hippocampotomy.

It was assumed that the foramen ovale could be cannulated with a 14 gauge needle, a size

typically available in trigeminal rhizotomy kits. Based on this constraint, the concentric tube robot could realistically be made of at most two tubes inside the 14g cannula, with the inner "tube" a superelastic nitinol wire. This wire can be thought of as a simulated ablator. Furthermore, by selecting the inner "tube" to be straight rather than pre-curved, our design remains compatible with commercially available laser, acoustic, or RF ablation probes [25-26].

We found that a helically curved trajectory exists such that the outer tube can insert from within the docking tube at the foramen ovale and accurately traverse along the medial axis of the hippocampus. An optimization was done in MATLAB to find a helical precurvature minimizing the mean distance of the needle trajectory from the medial axis. This design is illustrated for one patient case in Fig. 4.3. A prototype needle was then fabricated out of superelastic nitinol tube (1.143 mm O.D. x 0.965 mm I.D.). The tubing was constrained to the desired helical geometry using a jig made of thin laser-cut laminations (birch plywood, 0.79 mm) stacked and clamped together on a square shaft. Shape setting was done by electrical heat treatment. The jig and resulting pre-curved tube are shown in Fig. 4.7.

(a)

(b)

(c)
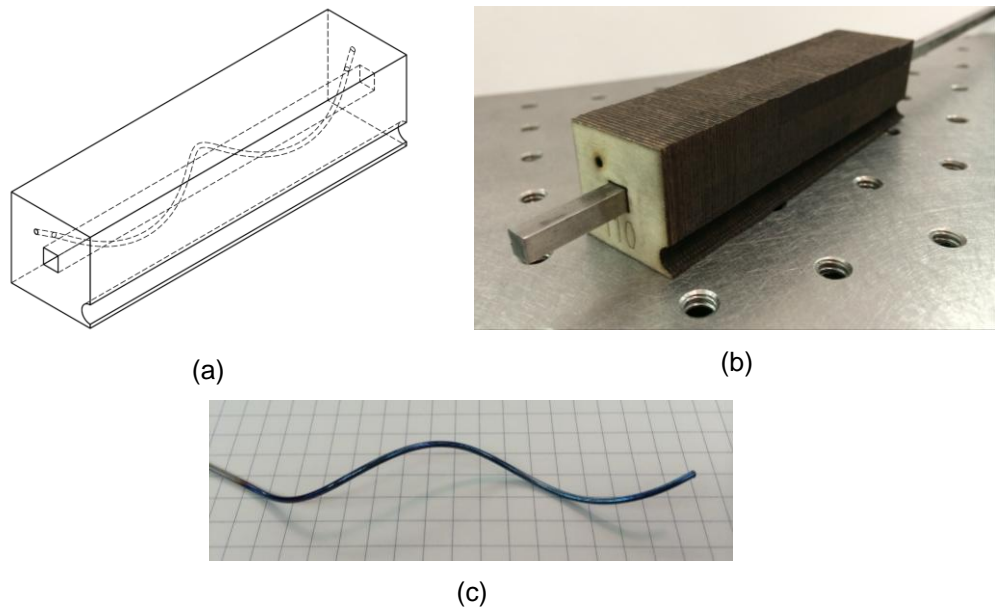
Figure 4.7 – Shape setting jig diagram (a) and photograph (b), photograph of resulting pre-curved needle (c).

After shape setting, to characterize the true shape of the prototype needle, the 3D Cartesian location of approximately 500 points along the length of the needle were measured using an electromagnetic tracker (Aurora Tabletop, Northern Digital, Inc., Waterloo, ON). The axis, radius, and pitch of each of the helical needles were determined by numerical fitting of these data. The helix axis is defined by a unit vector, which can be defined in 3D Cartesian space in terms of two parameters (the azimuth and elevation angles):

$$\hat{n} = \begin{bmatrix} \cos\theta\cos\phi & \sin\theta\cos\phi & \sin\phi \end{bmatrix}^T$$

Since the orientation of the helix data with respect to the coordinate system of the magnetic tracker was not known *a priori*, the best-fit axis was determined independently of the other helix parameters through an iterative, random-search algorithm in the θ-ϕ parameter space. For a perfectly circular helix, all points along the helix will lie on a circle when projected into the plane defined by the axis of the helix; therefore, in each iteration of the algorithm, the goodness of fit of a candidate axis to the helical data set was inferred from the square error between the projection of the experimental data points into the plane defined by the candidate axis. The fit of the projected data to a circle was calculated according the algorithm proposed by Taubin [27]. The candidate axis resulting in the smallest error of the circle fit was taken as the best-fit axis of the helix. After determining the best-fit axis, a Cartesian coordinate system was define with its z-axis along the best-fit axis of the helix. The radius r and pitch p of the helix were then determined by a non-linear least squares fit of the helix data to the standard equation for a circular helix:

$$\left[r\cos\left(\frac{z_i}{p}+\beta\right) \quad r\sin\left(\frac{z_i}{p}+\beta\right) \quad z_i \right] = \begin{bmatrix} x_i & y_i & z_i \end{bmatrix}$$

The phase angle β simply accounts for possible rotation of the experimental data points about the z-axis of the coordinate frame; it does not characterize the shape of the helix. Helical pitch is defined such that $2\pi p$ is the longitudinal distance traveled with one full revolution of the helix. Pitch is positive for right-handed helix and negative for a left-handed helix. A right-handed helix is needed for the left-side hippocampus, while a left-handed helix is needed for the right-side hippocampus. The EM tracker data and best-fit helix as calculate by our method are illustrated in Fig. 4.8 for measuring the true shape of the helical needle shown in Fig. 4.7.
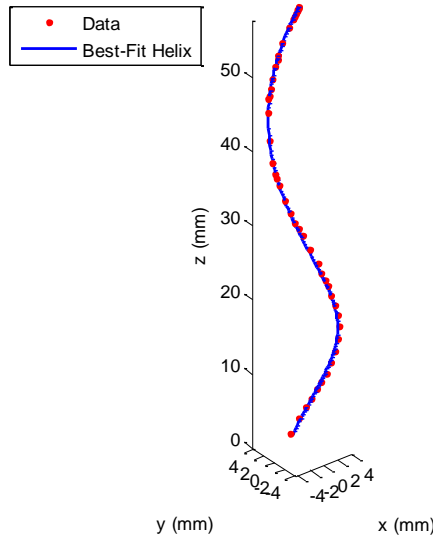
Figure 4.8 – Rotated EM tracker data and best-fit helix for Fig. 4.7(c) needle.

For needle trajectory planning, it was more convenient to define the helix using the Frenet-

Serret frame parameters of curvature κ and torsion τ. These parameters relate to radius and pitch by two equations, respectively:

$$r = \frac{\kappa}{\kappa^2 + \tau^2} \text{ and } p = \frac{\tau}{\kappa^2 + \tau^2}$$

For the optical tracker and MRI scanner experiments, the desired tube pre-curvature was a helix defined by $\kappa = 40.7$ m^{-1} and $\tau = 95.2$ m^{-1}rad^{-1}. This shape corresponded to a planned trajectory that followed the medial axis at a mean distance error of 0.84 mm. Based on prior outcomes using our electrical heating method for shape setting, it was assumed that curvature would relax 42.5% after the tube was removed from the jig, while torsion would remain relatively unchanged. Thus, the designed curvature of the jig was increased by a factor of 1/0.575. The prototype helical tube as shaped with this jig had a measured pre-curvature of $\kappa = 41.2$ m^{-1} and $\tau = 84.8$ m^{-1}rad^{-1}. While this does not exactly match the desired trajectory as initially planned, a slightly modified trajectory was then found using the prototype pre-curvature that will follow the hippocampus medial axis at a mean error distance of 1.80 mm; thus, the expected trajectory error due to uncertainties in shape setting is less than 1 mm.

VI. Robotic Controls

Forward Kinematics

For targeting experiments, the forward and differential kinematics of the concentric tube needle were needed. The forward kinematics are described simply by the equation of a helix, plus a line extending tangent to the helix corresponding to the portion of the ablation probe extending past the helical tube. These two parts are illustrated by the black and red curves in Fig. 4.9. The helical curve travels along the cylindrical surface as shown. A Cartesian coordinate frame {H} for the helix is defined with z-axis $\hat{z}_H$ co-linear with the central axis of the cylindrical surface and x-axis $\hat{x}_H$ always pointing towards the origin $\bar{o}_A$ of a Cartesian coordinate frame {A} of the robot. Frame {A} is defined with z-axis $\hat{z}_A$ co-linear with the transmission tube of the actuation unit.
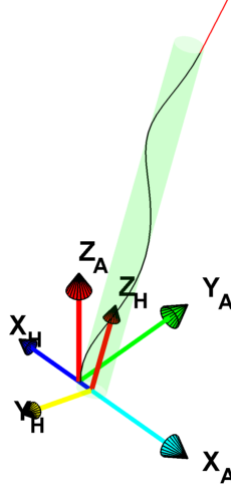
Figure 4.9 – Coordinate frames for robot {A} and helix {H}.

By this definition, the origin of {A} with respect to {H} is $^{H}\vec{o}_A = \left[r_{12} + \frac{1}{2}(d_o - d_2) \quad 0 \quad 0 \right]^T$. The

term $\frac{1}{2}(d_o - d_2)$, where d_o is outer cannula I.D. and d_2 is helical tube O.D., accounts for the

loose tolerance between these two tubes. Subscripts 1 and 2 respectively refer to parameters of

Tubes 1 and 2. The ablation probe (Tube 1) partially straightens out the helical tube (Tube 2) into

a less curved helix. Thus, the radius of the helix r_{12} includes the interaction of Tubes 1 and 2 across

their overlapped portion. The resultant curvature and torsion κ_{12} and τ_{12} are given as:

$$\kappa_{12} = \frac{E_1 I_1 \kappa_1 + E_2 I_2 \kappa_2}{E_1 I_1 + E_2 I_2} = \frac{E_2 I_2}{E_1 I_1 + E_2 I_2} \kappa_2 \text{ and } \tau_{12} = \tau_2$$

Tube stiffness EI is the product of the modulus of elasticity E of superelastic Nitinol (50 GPa)

and second moment of inertia about x- or y-axis, $I = (\pi/64)(OD^4 - ID^4)$.

Frame {H} rotation and origin position are dictated by the initial rotation ψ of Tube 2 inside the

outer cannula before it begins to extend in a follow-the-leader manner. For a right-handed helix,

$\psi = 0$ corresponds to the helix deploying dominantly along the $\hat{x}_A$ axis and for a left-handed helix

along the $-\hat{x}_A$ direction. By defining the transformation from {H} to {A} as dependent on ψ, the

helical curve in Fig. 4.9 can then always be written in parameterized form:

$$\begin{bmatrix} x_{12} & y_{12} & z_{12} \end{bmatrix} = \begin{bmatrix} r_{12} \cos\phi & r_{12} \sin\phi & p_{12}\phi \end{bmatrix}$$

The parameter ϕ is the angle of rotation about the helix central axis and relates to the extended

arc length L_2 of Tube 2 as $L_2 = \phi\sqrt{r_{12}^2 + p_{12}^2}$. For a position vector $^{H}\vec{p}$ in frame {H}, the

transformation to coordinate frame {A} is $^{A}\vec{p} = {}_{H}^{A}R({}^{H}\vec{p} - {}^{H}\vec{o}_A)$. The rotation matrix $_{H}^{A}R$ is defined

$$_H^A R = R_Z(\psi + \pi/2) R_X(\pi/2 - \alpha)$$

The pitch angle $\alpha = \tan^{-1}(p_{12}/r_{12})$ and the rotation matrices $R_Z(t)$ and $R_X(t)$ are defined

$$R_Z(t) = \begin{bmatrix} \cos t & -\sin t & 0 \\ \sin t & \cos t & 0 \\ 0 & 0 & 1 \end{bmatrix} \text{ and } R_X(t) = \begin{bmatrix} 1 & 0 & 0 \\ 0 & \cos t & -\sin t \\ 0 & \sin t & \cos t \end{bmatrix}$$

Next, considering the additional extension of Tube 1, define a unit tangent vector $\hat{t}$ at the point of departure from the helix. Then, the tip position of the concentric tube needle will be

$$^H\vec{p} = \begin{bmatrix} x_{12} & y_{12} & z_{12} \end{bmatrix}^T + (L_1 - L_2)\hat{t}$$

L_1 and L_2 are the arc lengths of Tubes 1 and 2, respectively, extended distal from the outer cannula. The unit tangent vector is simply the derivative with respect to ϕ of the parameterized helical curve equation, evaluated at the final value ϕ_f at the distal end of the overlapped tubes.

$$\hat{t} = \frac{\vec{t}}{\|\vec{t}\|} = \frac{1}{\sqrt{r_{12}^2 + p_{12}^2}}\vec{t} \quad \text{and} \quad \vec{t} = \frac{d}{d\phi}\begin{bmatrix} x_{12} \\ y_{12} \\ z_{12} \end{bmatrix}_{\phi=\phi_f} = \begin{bmatrix} -r_{12}\sin\phi \\ r_{12}\cos\phi \\ p_{12} \end{bmatrix}_{\phi=\phi_f}$$

Inverse Kinematics

The resolved rates method first proposed by Whitney was used to solve the inverse kinematics problem [28]. For a Cartesian point $^A\vec{p}$ in the workspace of the robot, the configuration of the joints $\vec{q} = \begin{bmatrix} q_1 & q_2 & q_3 \end{bmatrix}^T = \begin{bmatrix} \psi & L_2 & L_1 \end{bmatrix}^T$ was found by iteratively updating $\vec{q}_i$ on the i-th iteration using the joint velocity $\dot{\vec{q}}$ and time step Δt

$$\vec{q}_i = \vec{q}_{i-1} + \dot{\vec{q}}_{i-1}\Delta t$$

Joint velocity is the product of position error and the inverse of the Jacobian

$$\dot{\vec{q}}_i = (J^{-1}(\vec{q}_i))(^A\vec{p} - \vec{p}(\vec{q}_i))$$

VII. Experimental Setup and Results

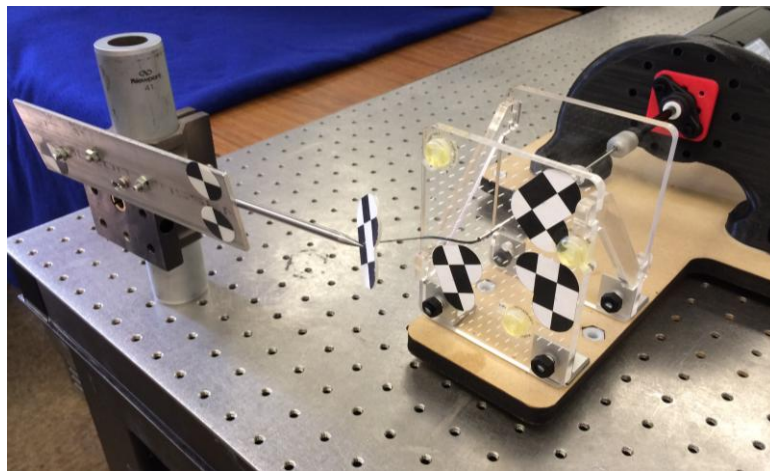*Optical Tracker Experiment*

Prior to in-scanner experiments, an initial benchtop assessment of needle tip accuracy was needed. Measurements were acquired using an optical tracking system (MicronTracker H3-60, Claron Technology). Three optical markers were adhered to the robot front plate at precisely known positions and used to register the robot and optical tracker spaces by a point-based registration.

An optical marker was also attached to the needle tip. Tip positions were measured for several poses of the concentric tube needle and then used to calibrate the initial rotation ψ in the kinematics. For Tube 1, a superelastic Nitinol wire (0.762 mm OD) was used as a simulated ablation probe. The prototype helical tube as previously described was Tube 2. The resultant radius and pitch parameters were $r_{12} = 3.65$ mm and $p_{12} = 10.53$ mm/rad.

For three placements of the concentric tube needle, the mean and maximum tip positioning errors were 0.97 and 1.06 mm, respectively. Each placement was planned by measuring a desired tip position using a pointer tool tracked by the camera. After transforming the desired position into robot coordinate frame, the joint configuration was computed by the inverse kinematics solution. The actuation unit was used to extend the concentric tube needle to that joint configuration, and the final position of the needle tip was then measured. The experimental setup is shown in Fig. 4.10 and the results are illustrated in Fig. 4.11.

MRI Scanner Experiment

Needle tip accuracy was next evaluated in a targeting experiment with MRI. The experiment was conducted with a Philips Achieva 3T scanner at Vanderbilt University Institute of Imaging Science. A phantom made of water and animal-protein based ballistic test media (Corbin SIM-TEST) was secured in an 8-channel head coil. The marker plate with MR-bright fiducials (see Fig. 4.10) was also positioned in the head coil just inferior to the phantom. A point-based registration was performed between scanner and robot space. The phantom was adjusted after each of the first two needle placements, so as to use an un-punctured portion of the phantom for the next placement. Thus, a registration was done for each of the three placements; fiducial registration errors were 0.16, 0.19, and 0.27 mm. For needle visualization, a T2-weighted fast spin echo imaging sequence (TR: 3000 ms, TE: 80 ms, 0.5mm x 0.5mm x 2mm, 1.5 SENSE) was used.

Figure 4.10 – Photograph of setup for optical tracker experiment.
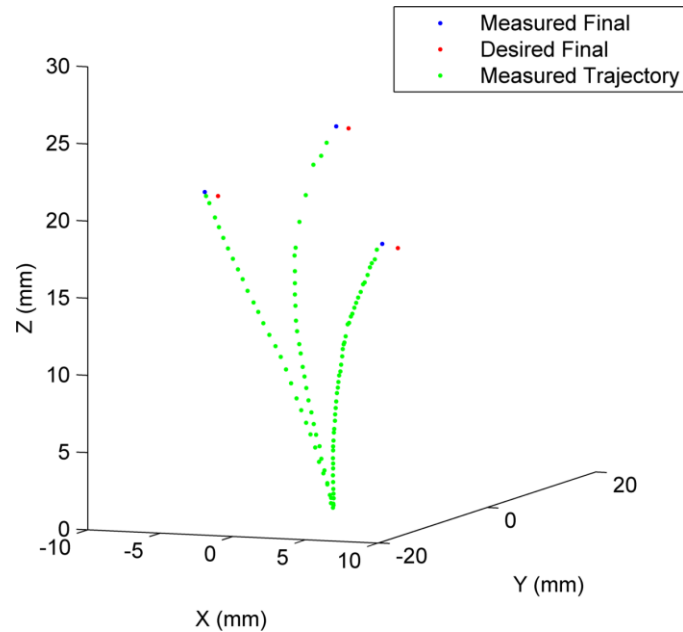
Figure 4.11 – Needle tip trajectory and final position as measured with optical tracker.

Controller hardware for the actuation unit resided outside the scanner room. Long pneumatic lines were run from the robot, through the wave guide, and connected to the valve bank. A differential signal cable driver was connected to each optical encoder module, shielded with copper tape, and grounded to the conductive sheathing of 10-conductor twisted pair cable. The proximal ends of the cables were connected to the patch panel; an additional cable outside the scanner room then connected from the patch panel to data acquisition electronics. This setup provided excellent noise rejection; there was no observable reduction in signal-to-noise ratio (SNR) even with the robot in full motion. For SNR measurements, an fBIRN phantom was imaged using the same imaging sequence as for needle localization.

For three placements of the concentric tube needle, the tip positioning errors were 3.07, 1.11, and 3.19 mm. An MR image of needle tip placement in the phantom is shown in Fig. 4.12. The cross-hatch indicates the desired target and the needle tip location is evident by the small (3 to 4 mm diameter) area of signal void.
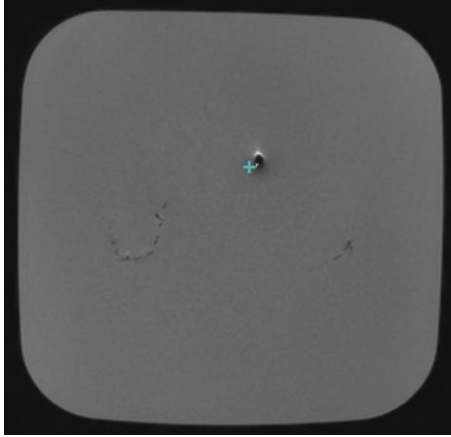
Figure 4.12 – MR image of the concentric tube needle tip in final position.

VIII. Discussion

A comparison of results from the optical tracker and MRI scanner experiments suggests likely sources of inaccuracy. To provide a scientific control, the same points were targeted in the MRI scanner as with the optical tracker. Thus, the decrease in accuracy going from optical tracker to MRI scanner is likely due to the change from free-space to in-phantom. Examining the MRI results, error was least for the shortest arc length extension and worst for the longest arc length extension. A reasonable cause for this observation is that the phantom slightly deflects the needle and this deflection is amplified as the needle continues to extend to longer arc lengths. This problem is potentially correctable using real-time MRI to adjust the needle trajectory mid-course. Full integration of MR imaging with the robotic controls is planned future work.

The concept of transforamenal hippocampotomy requires a curvilinear trajectory to feasibly target and ablate a hippocampal volume. This paper has reported design, fabrication, and characterization of a concentric tube needle that can deploy through the skull base and traverse along the medial axis of the hippocampus. Because image guidance using MRI is a key enabler for this procedure, the accuracy and MR-compatibility for robotic placement of this needle in the MRI scanner was tested. Experimental results suggest that an MRI-guided concentric tube robot could feasibly enable an incisionless procedure to treat epilepsy.

References

[1] S. Wiebe, W.T. Blume, J.P. Girvin, and M. Eliasziw. "A randomized, controlled trial of surgery for temporal-lobe epilepsy," *N Engl J Med*, 345(5):311-318, 2001.
[2] H. Choi, R.L. Sell, L. Lenert, P. Muennig, R.R. Goodman, F.G. Gilliam, and J.B. Wong. "Epilepsy surgery for pharmacoresistant temporal lobe epilepsy: a decision analysis," *JAMA*, 300(21):2497-2505, 2008.

[3] P. Kwan and M.J. Brodie. "Early identification of refractory epilepsy," *N Engl J Med*, 342(5):314-319, 2000.

[4] C.E. Begley, J.F. Annegers, D.R. Lairson, T.F. Reynolds, and W.A. Hauser. "Cost of epilepsy in the United States: a model based on incidence and prognosis," *Epilepsia*, 35(6):1230-1243, 1994.

[5] S.D. Lhatoo, J.K. Solomon, A.W. McEvoy, N.D. Kitchen, S.D. Shorvon, and J.W. Sander. "A prospective study of the requirement for and the provision of epilepsy surgery in the United Kingdom," *Epilepsia*, 44(5):673-676, 2003.

[6] S.G. Uijl, F.S.S. Leijten, K.G.M. Moons, E.P.H.M. Veltman, C.H. Ferrier, and C.A. van Donselaar. "Epilepsy surgery can help more adult patients with intractable seizures," *J Epilepsy Research*, 101(3):210-216, 2012.

[7] P. de Flon, E. Kumlien, C. Reuterwall, and P. Mattsson. "Empirical evidence of underutilization of referrals for epilepsy surgery evaluation," *Eur J Neurol*, 17(4):619-625, 2010.

[8] D.J. Curry, A. Gowdy, R.J. McNichols, and A.A. Wilfong. "MR-Guided Stereotactic Ablation of Epileptogenic Foci in Children". *Epilepsy and Behavior*, 24(4), August, pp. 408-414, 2012.

[9] P.S. Larson, P.A. Starr, G. Bates, L. Tansey, R.M. Richardson, and A.J. Martin. "An Optimized System for Interventional MRI Guided Stereotactic Surgery: Preliminary Evaluation of Targeting Accuracy," Neurosurgery, 70(Operative):95-103, 2012.

[10] J.T. Willie, N.G. Laxpati, D.L. Drane, A. Gowda, C. Appin, C. Hao, D.J. Brat, S.L. Helmers, A. Saindane, S.G. Nour, and R.E. Gross. "Real-Time Magnetic Resonance-Guided Stereotactic Laser Amygdalohippocampotomy for Mesial Temporal Lobe Epilepsy," *Neurosurgery,* 14(6):569-585, 2014.

[11] A.H. Hawasli, S. Bagade, J.S. Shimony, M. Miller-Thomas, and E.C. Leuthardt. "Magnetic Resonance Imaging-Guided Focused Laser Interstitial Thermal Therapy for Intracranial Lesions: Single-Institution Series," Neurosurgery, 73(6):1000-1017, 2013.

[12] R.J. Webster III, J.M. Romano, and N.J. Cowan, "Mechanics of Precurved-Tube Continuum Robots," *IEEE Transactions on Robotics*, 25(1):67-78, 2009.

[13] D.C. Rucker, B.A. Jones, and R.J. Webster III, "A geometrically exact model for externally loaded concentric tube continuum robots," *IEEE Transactions on Robotics*, 26(5):769-780, 2010.

[14] P.E. Dupont, J. Lock, B. Itkowitz, and E. Butler, "Design and control of concentric-tube robots," *IEEE Trans Robotics*, 26(2):209–225, 2010.

[15] H.B. Gilbert, J. Neimat, and R.J. Webster III, "Concentric Tube Robots as Steerable Needles: Achieving Follow-The-Leader Deployment," *IEEE Trans. Robotics*, 31(2):246-258, 2015.

[16] H. Su, D.C. Cardona, W. Shang, A. Camilo, G.A. Cole, D.C. Rucker, R.J. Webster III, and G.S. Fischer, "A MRI-guided concentric tube continuum robot with piezoelectric actuation: a

feasibility study," *2012 IEEE International Conference on Robotics and Automation (ICRA),* pp. 1939-1945.

[17] R.A. Sweeney, R. Bale, T. Auberger, M. Vogele, S. Foerster, M. Nevinny-Stickel, P. Lukas, "A Simple and Non-Invasive Vacuum Mouthpiece-Base Head Fixation System for High Precision Radiotherapy," *Radiotherapy and Oncology*, 43-37, 2001.

[18] D.B. Comber, J.S. Slightam, V.R. Gervasi, J.S. Neimat, and E.J. Barth, "Design and Control of an MR-Compatible Additively Manufactured Needle Steering Robot," *IEEE Trans. Robotics*, [In Press].

[19] D.B. Comber, J.E. Slightam, V.R. Gervasi, R.J. Webster III, and E.J. Barth, "Design and Precision Control of an MR-Compatible Flexible Fluidic Actuator," *Proc ASME/Bath Symposium on Fluid Power & Motion Control*, Sarasota, FL, 2013.

[20] A.G. Parrent and W.T. Blume. "Stereotactic amygdalohippocampotomy for the treatment of medial temporal lobe epilepsy," *Epilepsia*, 40(10):1408-1416, 1999.

[21] W.D. Yang, Q. Yu, J.N. Zhang, C.H. Shen, F.L. Wang, L.Y. Cui, H. Li, and S.Y. Yang. "Stereotactic combined amygdala and hippocampus lesions for treatment of medial temporal lobe epilepsy," *Chinese J Surgery*, 43(9):616-619, 2005.

[22] S. Clasen and P.L. Pereira, "Magnetic resonance guidance for radiofrequency ablation of liver tumors," *Journal of Magnetic Resonance Imaging*, 27(2):421-433, 2008.

[23] J.H. Johnson, G. Harris, and K. Williams, "BRAINSFit: Mutual Information Registrations of Whole-Brain 3D Images, Using the Insight Toolkit," *The Insight Journal*, http://hdl.handle.net/1926/1291, 2007.

[24] T.-C. Lee, R.L. Kashyap, and C.-N. Chu, "Building Skeleton Models via 3-D Medial Surface/Axis Thinning Algorithms," *CVGIP: Graphical Models and Image Processing*, 56(6):462-478, 1994.

[25] E.R. Cosman Sr. and E.R. Cosman Jr., "Radiofrequency Lesions," *Textbook of Stereotactic and Functional Neurosurgery*, eds. A.M. Lozano, P.L. Gildenberg and R.R. Tasker, Springer-Verlag, Chap. 82, pp. 1359-1382, 2009.

[26] E.C. Burdette, D.C. Rucker, P. Prakash, C.J. Diederich, J.M. Croom, C. Clarke, and R.J. Webster III, "The ACUSITT ultrasonic ablator: the first steerable needle with an integrated interventional tool," *SPIE Medical Imaging*, pp. 76290V-76290V, 2010.

[27] G. Taubin, "Estimation of planar curves, surfaces, and nonplanar space curves defined by implicit equations with applications to edge and range image segmentation," *IEEE Transactions on Pattern Analysis & Machine Intelligence*, 11:1115-1138, 1991.

[28] D.E. Whitney, "Resolved motion rate control of manipulators and human prostheses," *IEEE Transactions on man-machine systems*, 1969.

Chapter 5 – Optimization of Curvilinear Needle Trajectories for Transforamenal Hippocampotomy

David B. Comber[1], E. Bryn Pitt[1], Hunter B. Gilbert[1], Matthew W. Powelson[3], Emily Matijevich[4], Joseph S. Neimat[2], Robert J. Webster III[1], and Eric J. Barth[1]

Vanderbilt University (1) Dept. Mechanical Engineering and (2) Medical Center, (3) Tennessee Technological University, and (4) University of Illinois at Urbana-Champaign

Prologue

This paper summarizes optimization work in the design of a concentric tube robot for the transforamenal hippocampotomy procedure. Medical image volumes were obtained and de-identified as prescribed by the IRB exemption for this work. These volumes were manually segmented to extract anatomical features and geometries to inform mechanical design of the concentric tube robot and the positioning of the outer cannula for transforamenal access. The purpose of this work was to preliminarily determine whether a concentric tube robot could feasibly enable a transforamenal approach to thermal treatment of typical hippocampus volumes and thereby eliminate drilling the skull. For each hippocampus volume, a helically pre-curved tube was manually designed such that it could deliver the ablation probe in a follow-the-leader fashion along the medial axis of the hippocampus. For improved accuracy of traversing this trajectory, an optimization script was written to tune the design parameters.

Abstract

BACKGROUND: The recent development of MRI-guided laser-induced thermal therapy (LITT) offers a minimally-invasive alternative to craniotomies performed for tumor resection or for amydalohippocampectomy to control seizure disorders. Current LITT therapies rely on linear stereotactic trajectories that mandate twist-drill entry into the skull and potentially long approaches traversing healthy brain. The use of robotically-driven, telescoping, curved needles has the potential to reduce procedure invasiveness by tailoring trajectories to the curved shape of the ablated structure and by enabling access through natural orifices.

OBJECTIVE: This work investigated the feasibility of using a concentric tube robot to access the hippocampus through the foramen ovale to deliver thermal therapy and thereby provide a percutaneous treatment for epilepsy without drilling the skull.

METHODS: The skull and both hippocampi were segmented from dual CT/MR image volumes for 10 patients. For each of the 20 hippocampi, a concentric tube robot was designed and optimized to traverse a trajectory from the foramen ovale to and through the hippocampus from head to tail. **RESULTS:** Across all 20 cases, the mean distances (error) between hippocampus medial axis and backbone of the needle were 0.55, 1.11, and 1.66 mm for best, mean, and worst case, respectively. **CONCLUSION:** These curvilinear trajectories would provide accurate transforamenal delivery of an ablation probe to typical hippocampus volumes. This strategy has the potential to both decrease the invasiveness of the procedure while increasing the completeness of hippocampal ablation.

I. Introduction

Epilepsy has a point prevalence of about 0.6% globally and accounts for 1% of the global burden of disease in terms of disability-adjusted life years [1-2]. Forty-seven percent of patients are seizure-free with their first anti-epileptic drug (AED), and an additional 13% are seizure-free with their second AED [3]. Thus, about 40% of patients are refractory to medical therapy, and many of these are potential surgical candidates. Although epilepsy surgery outcomes reflect seizure-free rates of 70 to 80% [4-6], only a small fraction of potential surgical candidates are referred for treatment, due in part to physician bias against the highly invasive surgery [7-8]. Furthermore, the invasiveness of current surgical procedures likely causes many otherwise eligible patients for forgo surgery, despite the high likelihood of a seizure-free outcome.

In recent years, needle-based thermal ablation has been investigated as a minimally-invasive alternative to selective amygdalohippocampectomy (SAH). An SAH resection is less aggressive than standard anterior temporal lobectomy (ATL) but has demonstrated equivalent or near-equivalent outcomes [5]. Parent and Blume reported amygdalohippocampotomy by MRI-guided radiofrequency ablation (RFA); seizure outcomes were worse than ATL [9]. However, more recent clinical trials using MRI-guided laser ablation systems have more positively indicated the efficacy of percutaneous thermal ablation for epilepsy. Curry et al. reported seizure freedom at 3-month follow up for 5 pediatric patients treated using the Visualase Thermal Therapy System [10]. For a small series of procedures using the Visualase laser, Willie et al. reported a 6-month seizure freedom rate in 7 of 13 patients and substantial improvement for an additional 3 patients [11]. Hawasli et al. effectively treated one case of medically-refractory epilepsy using the Monteris Neuroblate System [12]. Despite some promising results, these ablation procedures to date have not matched the success of SAH. One of the primary limitations of current laser-induced thermal therapy (LITT) procedures is that the laser probes used with currently available devices are restricted to linear trajectories, which cannot lesion the entire hippocampus, even with directionally-aiming probes. Additionally, these procedures still require full operating room preparation for twist-drilling the skull.

The Transforamenal Ablation Concept

Our transforamenal approach is enabled by nonlinear probe trajectories that can also traverse the natural curvature of the hippocampus. These trajectories may offer more complete lesioning than linear trajectories, potentially improving seizure outcomes to equivalency with SAH. The proposed procedure accesses the mesial temporal lobe by cannulation of the foramen ovale. This would eliminate the need for twist-drilling the skull and allow for real-time course correction as the needle insertion is performed in the MRI.

The curvilinear trajectories required are realized using a concentric tube needle. This device consists of multiple, nested tubes of superelastic nitinol. Controllable, curvilinear motion is realized when axial translations and rotations are applied to the tube bases. For an overview of this technology, see [13-16]. A photograph of the concentric tube needle as designed for transforamenal ablation is shown for Fig. 1. Deploying this needle through a soft tissue media in a helical trajectory requires precise coordination of both insertion and axial rotation of the component tubes, as was recently described in [17], and is hence typically achieved by attaching motors to tube bases to enable computer control of tube motions. Several particular MRI-compatible robot designs have recently been proposed to accomplish this motion control [18-20]. In this paper we use the robot presented in [19]. Gilbert et al. also explored in simulation the potential benefits of using helical trajectories with a concentric tube needle to access the hippocampus from a burr hole in the back of the skull [17], but did not consider transforamenal deployment, which is the focus of our current paper.
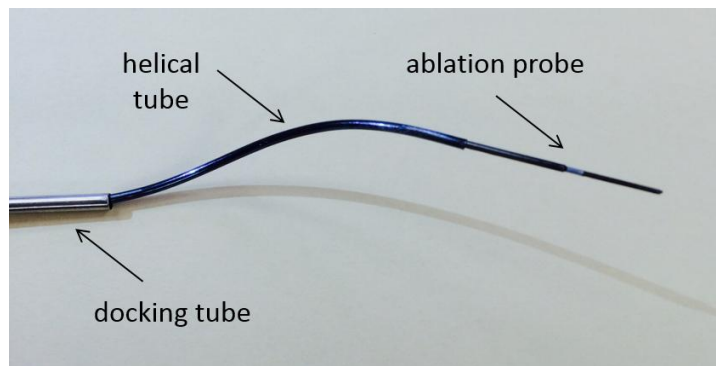
Figure 5.1 – Photograph of concentric tube needle concept for transforamenal ablation.

Several research groups have performed frameless stereotactic cannulation of the foramen ovale for trigeminal rhizotomy [21-22]. Similarly, for diagnosis and surgical treatment of drug-refractory epilepsy, Ortler et al. reported an optically-tracked aiming device and non-invasive maxillary fixation system called the Vogele-Bale-Hohner (VBH) head holder [23-24]. This setup facilitates placement of foramen ovale depth electrodes and also mitigates the risk of entering no-

go zones like the carotid artery during cannulation.

To enable the transforamenal ablation concept, we have developed a robotic MRI-guided system (see Fig. 2). The system comprises a concentric tube robot, an MR-compatible actuation unit, an ablation probe, and MRI guidance. We envision the procedure will take place from start to finish in a radiology suite and not require use of a surgical suite.
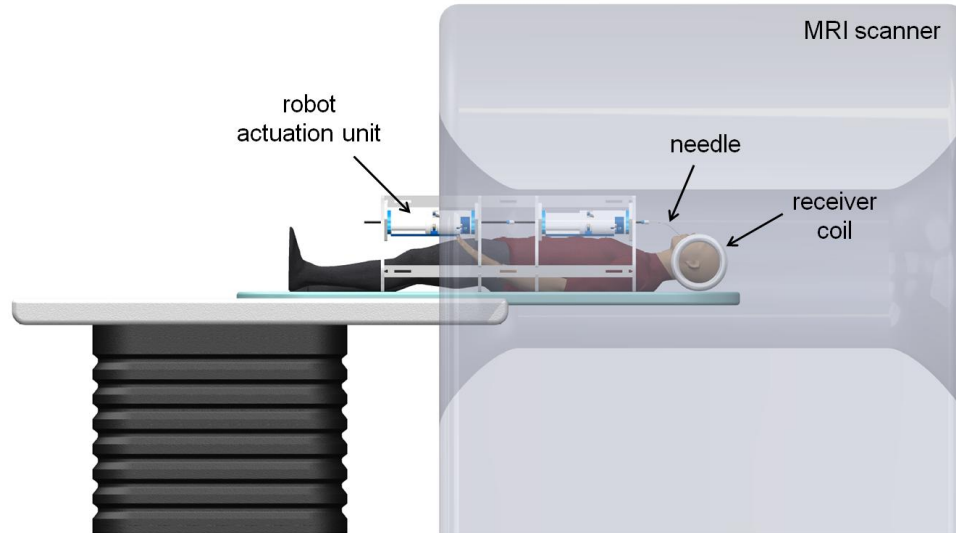
Figure 5.2 – Illustration of robotic transforamenal ablation system concept.

A robot actuation unit is positioned with the patient under general anesthesia within a standard MRI scanner. The robot is suspended above the patient's torso using an arch-shaped frame affixed to the patient gantry. The needle in the system is made up of two parts: a docking tube and a robotically-actuated concentric tube needle as shown in Fig. 5.1. The docking tube is an outer cannula manually placed by the neurosurgeon under fluoroscopic guidance to cannulate the foramen ovale. The concentric tube needle is then deployed through the docking tube and consists of a helically curved superelastic tube with the ablation probe contained within it.

The pneumatic robot actuators described in [19] grasp both the helical tube and the ablation probe at their proximal ends, and apply necessary insertion and axial rotation motions to deliver the helical tube and ablation probe into the hippocampus. Deployment is guided using real-time MRI for visualization. The helical tube and ablator pass as close as possible along the medial axis of the hippocampus towards its tail, and the ablation probe is then extended a short distance beyond the tip of the helical tube. Spatial thermal energy deposition is monitored using MR thermal imaging. When sufficient thermal dose is reached at this first position, the ablator is retracted within the helical tube, the helical tube is retracted a short distance along its entry trajectory, and the ablator is re-deployed. This process can be repeated as many times as desired by the physician to achieve desired thermal dose to the hippocampus. The amygdala can also be lesioned if desired by fully retracting the concentric tube robot into the docking tube and then re-inserting along a second trajectory targeting the amygdala.

We note that all aspects of this system concept are not yet fully integrated. In particular, we have developed the MRI compatible robotic hardware and the concentric tube device, and conducted initial experiments to verify MRI compatibility, but we have not yet integrated MRI thermometry or demonstrated use of MRI images to guide the needle to desired points. These are elements of future work. Our current paper addresses the question of whether the concentric tube needle (i.e. one with a single helically curved elastic tube, as described above) can, in principle, guide an ablator close to the medial axis of the hippocampus when delivered through the foramen ovale.

Here, we consider that a custom helical tube would be made for each patient, between the time that the patient obtains their preoperative diagnostic scan and the time of the intervention itself. This is feasible, since nitinol can be rapidly shape set to a helical curve using a heat treatment process (see [16-17] for examples of many tubes shape set in standard air furnaces).

Medical Image Analysis

To characterize the required workspace and constraints for the concentric tube robot, a medical image analysis was conducted. As a retrospective study with exemption approval from the Vanderbilt University Institutional Review Board, dual CT/MR image volumes were obtained and de-identified. Image sets for 10 patients were selected simply based on whether a sufficient amount of mandible and maxillary bone were included in the CT scan. This was to ensure adequate information to inform the design of cannula orientation angles for cannulation of the foramen ovale. No prior indication as to whether the hippocampus would be convenient to reach through the foramen ovale influenced patient selection.

Visualization and analysis of the image volumes were performed using the open source 3D Slicer software (www.slicer.org). The CT and MR image volumes were registered by a rigid transformation plus scaling using Slicer's BRAINSFit module [25]. The skull was segmented from the CT volume using an automated threshold. The hippocampi and amygdala were segmented manually from the MRI volume and reviewed and confirmed by an experienced neurosurgeon (Dr. Neimat, who is a co-author on this manuscript).

Concentric Tube Needle Design

The skull, hippocampus, and foramen ovale models were used to design a concentric tube needle trajectory for each patient. It was assumed that the foramen ovale could be cannulated with a 14-gauge needle, a size typically available in trigeminal rhizotomy kits. Our design objective was to cause the ablator to pass as close to the medial axis as possible. The medial axis is the locus of the centers of all maximal spheres inscribed within the object, where maximal spheres touch more than one point on the object boundary [26]. The rationale for this approach is that if the ablator radiates heat evenly in all directions, it will be most likely to achieve uniform coverage of the

hippocampus if it travels along the medial axis. However, we note that the ablator need not travel perfectly along the axis, as there are examples of successful ablations being performed substantially away from the medial axis [10-12].

The segmented anatomical models were imported to MATLAB so that they could be overlaid with possible trajectories of the concentric tube needle. The medial axis was computed using the skeletonizing method of [26]. The forward kinematic equations of the robot were used to manually design a helical tube capable of following a trajectory close to the medial axis. An example of this design is shown for Patient 4 in Fig. 5.3. This manual design served as an initialization for the numerical optimization algorithm. Additional inputs to the algorithm are initial orientation angles for the docking tube and constraints on those angles. Specifically, using the skull model, we defined a coordinate frame for the docking tube such that its central axis lies in a plane of maximum adjustability in the space between maxilla and mandible. This plane is approximately sagittal and the corresponding range of motion is illustrated by the larger circular sector in Fig. 5.3(c). This range of allowable motion was constrained in the optimization to ±10°, and for the orthogonal plane shown in Fig. 5.3(b), a constraint of ±5° was imposed.

A total of seven parameters were optimized: helix curvature, helix torsion, helix maximum insertion length, helix initial rotation, ablation probe maximum insertion length, and the two orientation angles of the docking tube. A maximum of 8% recoverable strain was allowed for helical
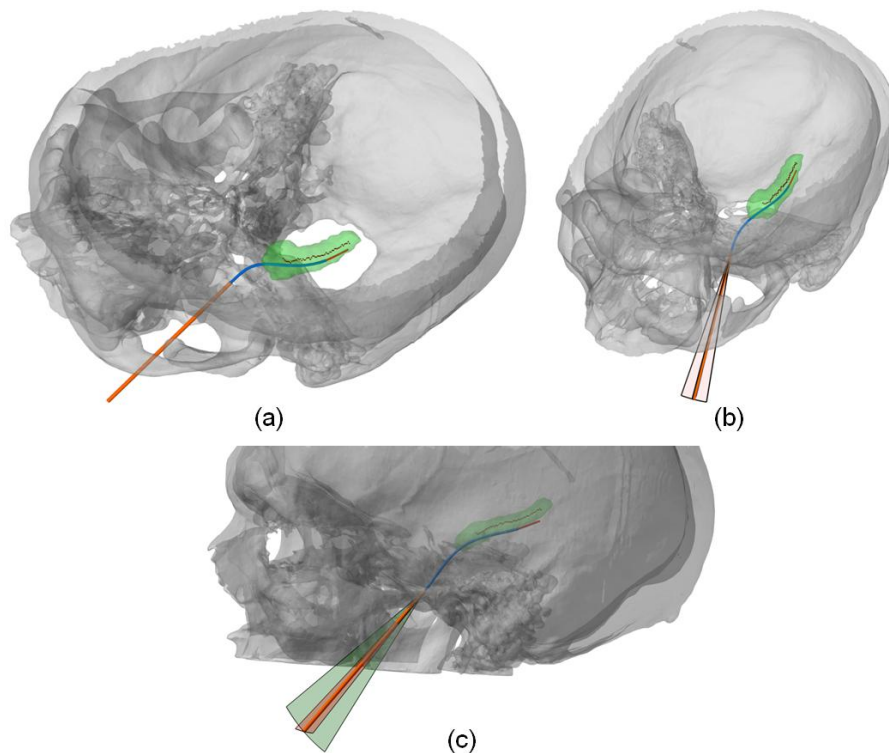
Figure 5.3 – (a) Initial transforamenal trajectory for Patient 4. (b,c) Docking tube range of allowable motion.

tube curvature; this is the often-quoted recoverable strain limit for nitinol in the literature. The optimization algorithm used the Nelder-Mead simplex method and was implemented with the MATLAB *fminsearch* function [27]. Parameter limits were enforced via cost conditions. The optimization minimized the mean distance from each point on the medial axis of the hippocampus to the closest point on the concentric tube needle's backbone.

III. Results

The optimized concentric tube robot design for Patient 4 is shown in Fig. 5.4. A comparison of initial (Fig. 5.3) to optimized designs shows a substantial improvement in the accuracy of the trajectory to traverse the medial axis of the hippocampus. A summary of all 20 optimized designs is provided in Fig. 5.5 and Table 5.1. Figure 5.5 shows the medial axis of each hippocampus and each trajectory at its maximum path distance from the foramen ovale. Across all 20 cases, the mean distances (error) between hippocampus medial axis and backbone of the needle were 0.55, 1.11, and 1.66 mm for best, mean, and worst case, respectively. For each case, a helical curvature was found that will result in strains less than the 8% limit for superelastic nitinol. This ensures that after the helical tube is straightened inside the docking tube, the helical tube will return to its pre-curved shape as it deploys.

Considering the summary of the design parameters given in Table 5.1, there are several reasons why patient-specific designs were required to achieve sufficient accuracy. First, the helical tube torsion is positive for the left hippocampus and negative for the right hippocampus, so at least two different needles are required. Second, optimized torsion varied by ±25% from the mean (89.1 $m^{-1}rad^{-1}$) for the set of right-handed helices and by ±19% from the mean (107.3 $m^{-1}rad^{-1}$) for the left-handed helices. If a generic shaped needle were used instead, this amount of variation from optimal torsion would result in additional trajectory error of 3 to 5 mm.
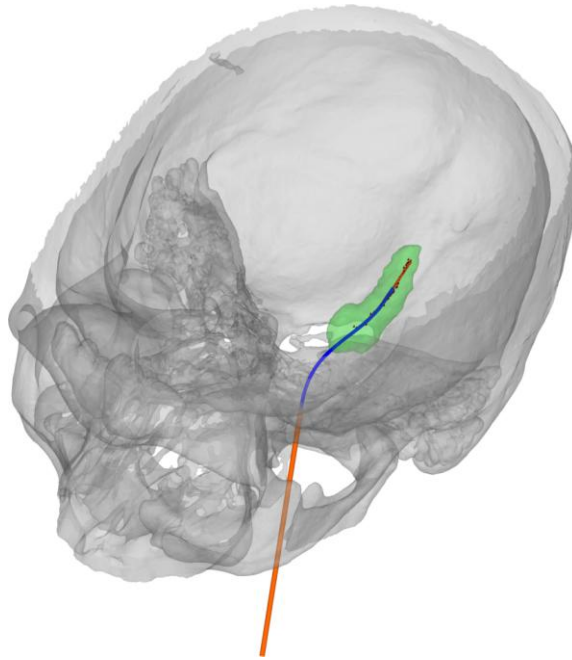
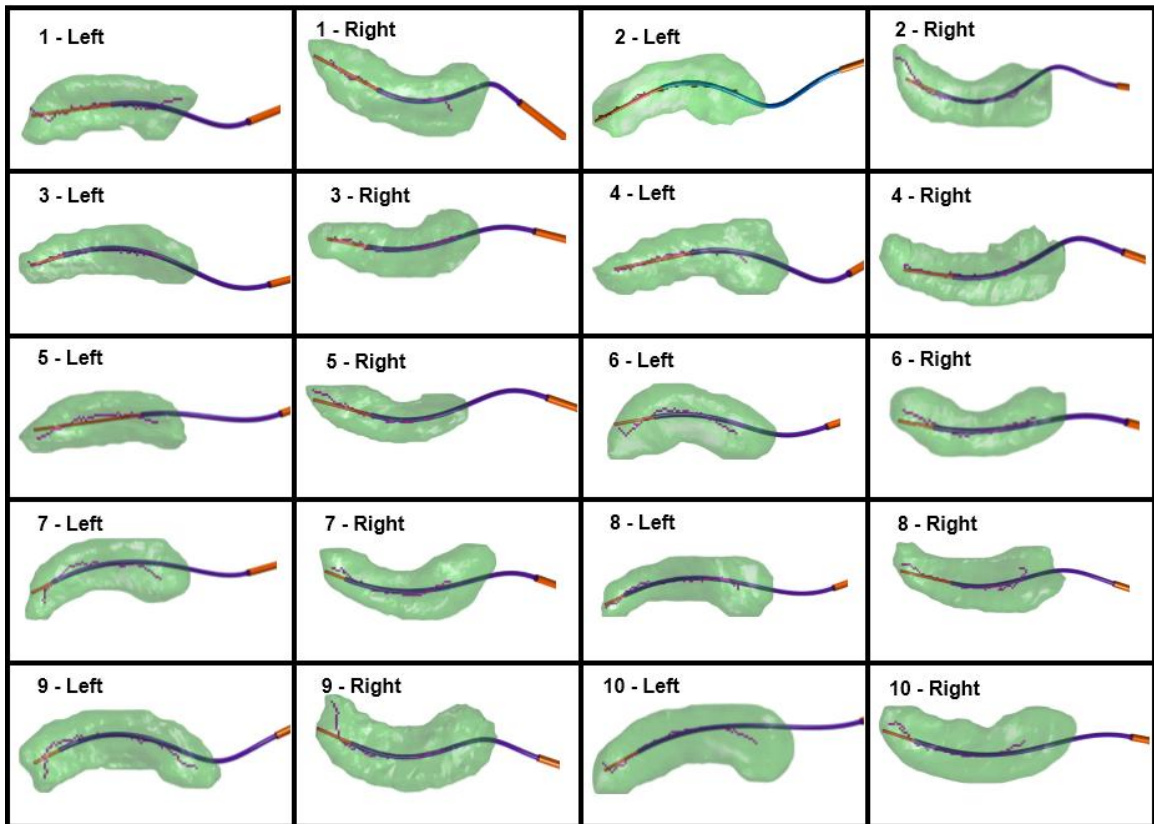**Figure 5.4** – Optimized concentric tube robot design for Patient 4.

Figure 5.5 – Optimized concentric tube robot designs for 20 hippocampi, axial view.

Table 5.1 – Concentric tube robot design parameters and corresponding error predictions.

Patient No.	Helically Pre-curved Tube			Ablation Probe	
	Length (mm)	Curvature (m^{-1})	Torsion (m^{-1}·rad^{-1})	Length (mm)	Mean Error (mm)
1 Left	42.0	40.7	95.2	60.8	0.84
1 Right	47.6	60.8	-110.4	65.6	0.67
2 Left	56.2	78.3	107.0	71.2	0.81
2 Right	56.0	83.9	-118.0	65.0	1.26
3 Left	52.8	49.7	94.9	60.6	0.74
3 Right	42.6	44.9	-112.9	51.9	1.14
4 Left	46.3	50.6	84.1	63.1	0.59
4 Right	50.0	55.1	-102.8	61.1	0.55
5 Left	45.5	43.6	92.5	58.9	0.86
5 Right	33.8	57.0	-111.3	57.4	1.26
6 Left	48.3	39.9	102.7	58.1	1.49
6 Right	47.2	29.9	-101.5	54.9	1.62
7 Left	58.7	32.4	72.2	64.8	1.43
7 Right	56.5	34.1	-84.7	62.0	0.90
8 Left	58.2	39.5	77.8	63.6	1.17
8 Right	48.5	48.9	-114.0	62.3	1.64
9 Left	58.4	62.3	102.1	64.9	1.59
9 Right	52.6	59.0	-125.8	62.4	1.66
10 Left	55.0	32.9	62.9	63.5	0.90
10 Right	55.2	36.8	-91.2	63.3	1.03

It is feasible to rapidly and accurately fabricate patient-specific needles using a new shape setting method by electric heating developed by our lab (HB Gilbert, unpublished data, March 2015). A prototype concentric tube needle was fabricated for Patient 1, using a superelastic nitinol tube of outer and inner diameters 1.14 and 0.97 mm, respectively. The fabricated prototype had a curvature of 41.2 m^{-1} and torsion of 84.8 m^{-1}rad^{-1}. Since the prototype's curvature and torsion are slightly different from the optimized values given in Table 1, due to uncertainties inherent in the heat shape setting process, we re-ran the optimization with the fabricated tube's measured curvature and torsion to find the best insertion path for the fabricated tube. This new trajectory follows the medial axis of the hippocampus at a mean error distance of 1.80 mm and is illustrated in Fig. 5.6.
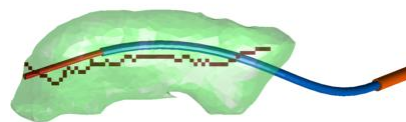
Figure 5.6 – Optimized trajectory using measured curvature and torsion of prototype.

IV. Discussion

The study described in this paper indicates that it is feasible to reach the hippocampus through the foramen ovale with a concentric tube needle for the purpose of hippocampotomy by ablation. In parallel work, we have designed and fabricated an actuation unit powered by pneumatic stepper

motors [19]. Preliminary testing of this robot's MRI-compatibility indicates no observable degradation in signal-to-noise ratio, as measured by the method of [28], even with the robot in full motion. Imaging protocols for MR thermometry are being evaluated with our needle prototype and will be integrated with MRI guidance for the robot. A variety of ablation technologies are possible, and future work will be needed to choose the best technology for this application.

In conclusion, this paper has described a novel approach to access the hippocampus through a natural orifice using a concentric tube robot. For each hippocampus in the study, simulation of the optimized needle trajectory shows accurate traversal of the curvilinear medial axis of the target volume. A prototype needle with sufficiently accurate pre-curvature has been manufactured and successfully tested for MR-compatibility with an MRI-compatible robot (DB Comber, unpublished data, Aug 2015). These results preliminarily suggest that MRI-guided transforamenal ablation could be a less-invasive alternative to current ablation treatments for epilepsy and may ultimately provide a more complete ablation. Additional work on the robotic needle hardware may also provide a generic curvature design suitable for all potential curved trajectories without need for patient-specific customization.

References

[1] S. Wiebe, D.R. Bellhouse, C. Fallahay, and M. Eliasziw, "Burden of Epilepsy: The Ontario Health Survey," *Canadian J Neurol Sci*, 26:263-270, 1999.

[2] J. Engel, Jr., S. Wiebe, J. French, M. Sperling, P. Williamson, D. Spencer, R. Gumnit, C. Zahn, E. Westbrook, and B. Enos, "Practice Parameter: Temporal Lobe and Localized Neocortical Resections for Epilepsy," *Epilepsia*, 44(6):741-751, 2003.

[3] P. Kwan and M.J. Brodie, "Early identification of refractory epilepsy," *N Engl J Med*, 342(5):314-319, 2000.

[4] T. Hori, F. Yamane, T. Ochiai, M. Hayashi, and T. Taira, "Subtemporal Amygdalohippocam-pectomy Prevents Verbal Memory Impairment in the Language-Dominant Hemisphere," *Stereotact Funct Neurosurg*, 80(1-4):18-21, 2003.

[5] M.T. Lutz, H. Clusmann, C.E. Elger, J. Schramm, and C. Helmstaedter, "Neuropsychological Outcome after Selective Amygdalohippocampectomy with Transsylvian versus Transcortical Approach: A Randomized Prospective Clinical Trial of Surgery for Temporal Lobe Epilepsy," *Epilepsia*, 45(7):809–816, 2004.

[6] H.G. Wieser, M. Ortega, A.Friedman, and Y. Yonekawa, "Long-term seizure outcomes following amygdalohippocampectomy," *J Neurosurg*, 98:751–763, 2003.

[7] S.G. Uijl, F.S.S. Leijten, K.G.M. Moons, E.P.H.M. Veltman, C.H. Ferrier, and C.A. van Donselaar, "Epilepsy surgery can help more adult patients with intractable seizures," *J Epilepsy Research*, 101:210-216, 2012.

[8] P. de Flon, E. Kumlien, C. Reuterwall, and P. Mattsson, "Empirical evidence of underutilization of referrals for epilepsy surgery evaluation," *Eur J Neurol*, 17(4):619-625, 2010.

[9] A.G. Parrent and W.T. Blume, "Stereotactic amygdalohippocampotomy for the treatment of medial temporal lobe epilepsy," *Epilepsia*, 40(10):1408-1416, 1999.

[10] D.J. Curry, A. Gowdy, R.J. McNichols, and A.A. Wilfong, "MR-Guided Stereotactic Ablation of Epileptogenic Foci in Children". *Epilepsy and Behavior*, 24(4):408-414, 2012.

[11] J.T. Willie, N.G. Laxpati, D.L. Drane, A. Gowda, C. Appin, C. Hao, D.J. Brat, S.L. Helmers, A. Saindane, S.G. Nour, and R.E. Gross, "Real-time magnetic resonance-guided stereotactic laser amygdalohippocampotomy for mesial temporal lobe epilepsy," *Neurosurgery*, 74(6):569-85, 2014.

[12] A.H. Hawasli, S.K. Bandt, R.E. Hogan, N. Werner, and E.C. Leuthardt, "Laser Ablation as Treatment Strategy for Medically Refractory Dominant Insular Epilepsy: Therapeutic and Functional Considerations," *Stereotact Funct Neurosurg*, 92:397–404, 2014.

[13] R.J. Webster III, J.M. Romano, and N.J. Cowan, "Mechanics of Precurved-Tube Continuum Robots," *IEEE Transactions on Robotics*, 25(1):67-78, 2009.

[14] D.C. Rucker, B.A. Jones, and R.J. Webster III, "A geometrically exact model for externally loaded concentric tube continuum robots," *IEEE Transactions on Robotics*, 26(5):769-780, 2010.

[15] P.E. Dupont, J. Lock, B. Itkowitz, and E. Butler, "Design and control of concentric-tube robots," *IEEE Trans Robotics*, 26(2):209–225, 2010.

[16] H.B. Gilbert, D.C. Rucker, and R.J. Webster III, "Concentric Tube Robots: State of the Art and Future Directions", in *16th International Symposium on Robotics Research (2013)*, *Springer Tracts in Advanced Robotics*, In Press, 2013.

[17] H.B. Gilbert, J. Neimat, and R.J. Webster III, "Concentric Tube Robots as Steerable Needles: Achieving Follow-The-Leader Deployment," *IEEE Trans. Robotics*, 31(2):246-258, 2015.

[18] D.B. Comber, E.J. Barth, and R.J. Webster III, "Design and control of a magnetic resonance compatible precision pneumatic active cannula robot," *ASME J Med Dev*, 8(1):011003, 2014.

[19] D.B. Comber, J.E. Slightam, J.S. Neimat, V.R. Gervasi, and E.J. Barth, "Design and Control of an MR-Compatible, Additively Manufactured Needle Steering Robot," *IEEE Trans Robotics*, In Press.

[20] H. Su, D.C. Cardona, W. Shang, A. Camilo, G.A. Cole, D.C. Rucker, R.J. Webster III, and G.S. Fischer, "A MRI-guided concentric tube continuum robot with piezoelectric actuation: a feasibility study," *2012 IEEE International Conference on Robotics and Automation (ICRA),* pp. 1939-1945.

[21] R. Bale, I. Laimer, A. Martin, A. Schlager, C. Mayr, M. Reiger, B. Czermak, P. Kovacs, and G. Widmann, "Frameless Stereotactic Cannulation of the Foramen Ovale for Ablative Treatment of Trigeminal Neuralgia," *Neurosurgery*, 59(ONS Suppl 4):ONS-394–ONS-402, 2006.

[22] M. Lin, M.-H. Lee, T.-C. Wang, Y.-K. Cheng, C.-H. Su, C.-M. Chang, and J.-T. Yang, "Foramen ovale cannulation guided by intra-operative computed tomography with integrated neuronavigation for the treatment of trigeminal neuralgia," *Acta Neurochir*, 153:1593-1599, 2011.

[23] M. Ortler, G. Widmann, E. Trinka, T. Fiegele, W. Eisner, K. Twerdy, G. Walser, J. Dobesberger, I. Unterberger, and R. Bale, "Frameless Stereotactic Placement of Foramen Ovale Electrodes in Patients with Drug-Refractory Temporal Lobe Epilepsy," *Neurosurgery*, 62(2):ONS481-ONS489, 2008.

[24] M. Ortler, E. Trinka, J. Dobesberger, R. Bauer, C. Unterhofer, K. Twerdy, G. Walser, I. Untergerger, E. Donnemiller, T. Gotwald, G. Widmann, and R. Bale, "Integration of multimodality imaging and surgical navigation in the management of patients with refractory epilepsy. A pilot study using a new minimally invasive reference and head-fixation system," *Acta Neurochir*, 152:365-378, 2010.

[25] J.H. Johnson, G. Harris, and K. Williams, "BRAINSFit: Mutual Information Registrations of Whole-Brain 3D Images, Using the Insight Toolkit," *The Insight Journal*, http://hdl.handle.net/1926/1291, 2007.

[26] T.-C. Lee, R.L. Kashyap, and C.-N. Chu, "Building Skeleton Models via 3-D Medial Surface/Axis Thinning Algorithms," *CVGIP: Graphical Models and Image Processing*, 56(6):462-478, 1994.

[27] J.C Lagarias, J.A. Reeds, M.H. Wright, and P.E. Wright, "Convergence Properties of the Nelder-Mead Simplex Method in Low Dimensions," *SIAM Journal of Optimization*, 9(1):112-147, 1998.

[28] K. Chinzei, R. Kikinis, and F.A. Jolesz, "MR compatibility of mechatronic devices: design criteria," *Medical Image Computing and Computer-Assisted Intervention–MICCAI'99*, pp. 1020-1030, January 1999.

Chapter 6 – Conclusion

Summary

This dissertation has presented the design and control of a concentric tube robot as applied to an MRI-guided system concept for an incisionless treatment for epilepsy. The technological capability to go through the skull base to target and treat the hippocampus and other deep brain structures creates exciting potential for significant medical advancements. This work has aimed to solve some of the technical barriers preventing this innovative concept from coming to fruition. The mechanical design and controls presented herein contribute a novel device for robotic actuation inside the MRI magnet. Testing results from in-scanner experiments suggest the device could safely and precisely control the concentric tube needle and thereby enable full integration of the needle with intraoperative MRI for the envisioned transforamenal therapy.

The robotic platform with pneumatic steppers contributes broadly to the fields of robotics and fluid power by its demonstration of additively-manufactured fluidic actuators and mechanisms. The compact device footprint, the simple monolithic structure of the FFA's, and the relatively low fabrication costs are attributes of the robot that were carefully designed to ensure it is a suitable medical device. Additive manufacturing served an essential role in the engineering of these features. Furthermore, the successful and continuing operation of the robot for more than one year without any mechanical failures speaks to the viability of using additive manufacturing to produce functional, end-use devices.

This 3D-printed hardware is uniquely different from prior art in MR-compatible robots. It still provides precision performance, but it has the potential to be made easily available as open-source hardware for interventional MRI research. A major reason that MRI-guided robots are not yet routinely used is that each research group has to first develop MR-compatible custom hardware. This technological barrier could be removed by creating a small business to provide downloadable plans and CAD parts that can be locally 3-D printed and assembled to create functional copies of the robot.

Future Work

While the MR-compatible robotic hardware as presented in this dissertation is at a sufficiently mature stage of development, there are several components of the MRI-guided robotic system for epilepsy treatment that require future work before moving to animal model studies. Functionalities that are still needed include: image-guidance software and user interface for surgical navigation; evaluation and selection of the most appropriate ablation technology; development of MR thermal imaging protocols; and refinements to the manually-adjustable aiming device and bite block

hardware. In the design of these components, particular attention should be given to how they will be integrated together to form a complete, working system and how the efficacy of that system will be evaluated in testing.

To inform this future design work, the needle tube simulation and optimization described herein should be leveraged. The data and analysis produced from the study of twenty different epilepsy patient cases is useful for identifying the engineering requirements (e.g. repeatability, accuracy, range of motion) for hardware design to do animal model and cadaver studies. Additionally, an interesting continuation of the tube optimization studies is to determine a minimum number of unique pre-curvatures for a set of needles to effectively treat the broader epilepsy patient population. As this analysis will be interdependent with the performance of the robotic hardware as a whole, particular attention should be given to ensure the uncertainties and errors of the components will cumulatively be acceptable.

The transforamenal therapy concept and robotic system hardware can be applied broadly in future work to create less invasive and more viable treatments for other neurological diseases (e.g. Parkinson's, Huntington's, Alzheimer's) and cancers of the deep brain (e.g. brain stem). A similar roadmap for design can be followed, segmenting target volumes from de-identified image sets and running tube optimization algorithms to design a concentric tube robot with an acceptable workspace. The MR-compatible, 3D-printed hardware can be slightly modified to match the ranges of motion required for the new design.

Contribution

As summarized above, this dissertation has described the design, fabrication, and validation of an MRI-compatible concentric tube robot and an investigation of its feasible use for MRI-guided transforamenal hippocampotomy. Key contributions for the four manuscripts resulting directly from this work include the following:

- A pneumatic, MR-compatible robot for neurosurgical and other soft tissue interventions
- Novel designs of bellows-type fluidic actuators, additively manufactured for compactness and hermetic sealing
- A hybrid controller for precision operation of fail-safe pneumatic steppers
- An innovative system concept for a skull base approach to treating epilepsy
- Hardware prototypes for the transforamenal ablation concept: non-invasive head holder, helical needle, RF ablation probe, and modular actuation units
- Needle design optimization and analysis of the transforamenal hippocampotomy concept for multiple patient cases

These contributions collectively help to pioneer the transformation of deep brain treatment from open surgery to a minimally invasive, out-patient procedure.